Uncertainty quantification for solar sails in the near-Earth environment

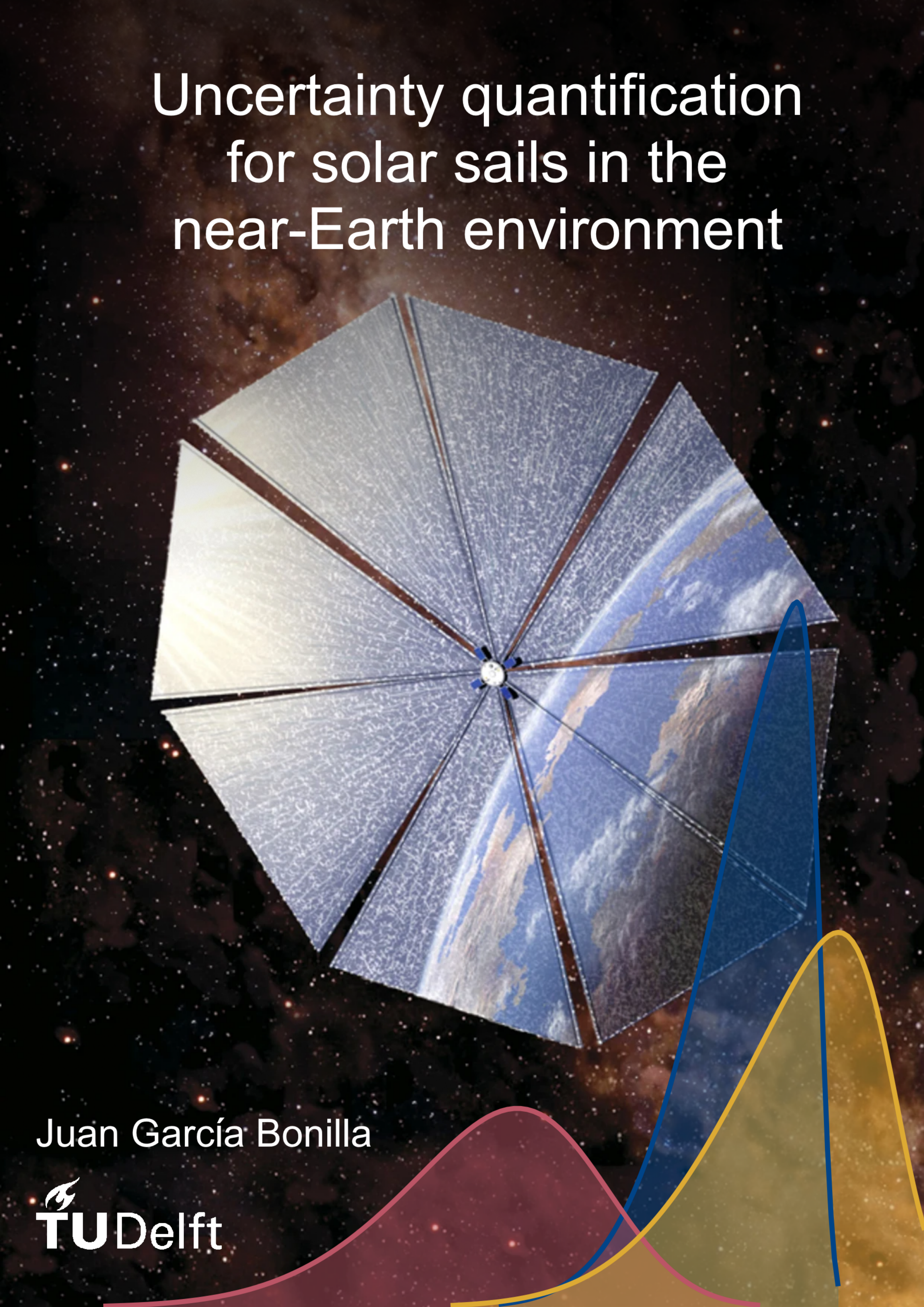

Juan García Bonilla

TU Delft

Uncertainty quantification for solar sails in the near-Earth environment

by

Juan Garcia Bonilla

to obtain the degree of Master of Science
at the Delft University of Technology,
to be defended publicly on Wednesday August 30, 2023 at 9:00 AM.

Student number:	5460646	
Project duration:	February 1, 2023 – August 30, 2023	
Supervisors:	Dr. ir. J. Heiligers	
	Prof. dr. ir. P.N.A.M. Visser	
Co-supervisor:	Ir. L. Carzana	
Thesis committee:	Prof. dr. ir. P.N.A.M. Visser	Committee chair, Supervisor
	Ir. L. Carzana	Co-supervisor
	Ir. R. Noomen	Examiner
	Dr. ir. S. Speretta	Examiner

to the family I was born with
and the one I have found along the way

"We demand rigidly defined areas of doubt and uncertainty!"
- Douglas Adams

Preface

There is an ancient African proverb, though no one can trace exactly when or where it originated, that translates to: *It takes a village to raise a child.* Now, I am still young and I know very little about raising childs. In fact, I know very little of most things. However, today I can say that I know something about writing a thesis, and thus I can confidently add my contribution to the list of contemporary Spanish-Dutch proverbs: *It takes a village to write a thesis.* I don't know if this proverb will catch on as much as the one about raising a child, but one has to try. And thus, with this brief preface, I would like to thank *my village* for writing with thesis with me.

I must begin by thanking Livio Carzana. Livio has always been there, every Wednesday at 5 PM and through countless e-mail, to give me his honest feedback and to provide indispensable moral support. His help cannot be overstated and I am extremely happy to have shared this experience with him, even if he left me to sleep in a corridor once in New York. Jennette Heiligers also offered her support and extremely valuable opinion, especially during the beginning of the thesis and before the ISSS conference. While she had to step down from being my supervisor due to much more important concerns, I feel that her impact has steered my thesis until the very last day. From Livio and Jeannette I have learned to be thorough, to hold my work to the highest standards, and to be ambitious yet reasonable about my goals. After Jeannette stepped down, Pieter Visser was kind enough to replace her as my supervisor, and I am grateful to him for making me feel confident through this transition.

Over the pond, I want to thank Hanspeter Shaub, who kindly welcomed me to his research lab at the University of Colorado Boulder for a six month research stay. He was very kind to me, he advised me about my research, and he was extremely encouraging as I collaborated with the Basilisk development team. However, the thing I'm most grateful to him for is for making me part of the AVS Lab community. During my stay, I was lucky to meet all the brilliant researchers at the lab and share lunch breaks, coffe breaks, happy hours, parties, and even a rafting trip with them. Having a research team to call my own, even if only temporarily, made the prospect of doing my own research a bit less daunting.

Finally, I must thank my family, the one I was born with and the one I found in Delft. This thesis not only represents the culmination of my technical work at TUDelft, but also of my wonderful life in the Netherlands. To begin with, if I was able to venture out into the world fearless and motivated as I did, it was only because I know my mom and dad will always have my back. No matter the problem or the mistake I have made, no matter whether they understand my eclectic life or not, I have never doubted that I could count on them. Thus, I thank them for this precious gift they have given me. In Delft, on the other hand, I found a family with whom to *share* my eclectic life. People with whom I could explore who I was, who I wanted to become, and how I wanted my life to be. It is unfair for me to name some names while skipping others, so I won't. But know that, if you have known me and are reading this, you have contributed to shaping the best two years of my life. It does not matter if we were housemates, or classmates, or if we shared a beer once, or if I poured one all over you, or if we had lunch or went to the North Pole together, or if we danced or kissed at a party. You are important to me, even if sometimes I fail to let you know. I wouldn't change any of the things I have done or the people I have met in Delft. So thank you all, truly, for making Delft so hard to leave behind.

Executive Summary

Solar sailing is a propellantless propulsion method based on the use of large reflective surfaces to maximize the effect of solar radiation pressure on spacecraft. Despite the wealth of research on solar-sail mission design in the literature, there is a clear lack of studies on the effects of uncertainties for these missions, especially for those in the near-Earth environment. This gap in the literature might appear surprising, as sailcraft behaviour is complex and difficult to predict from Earth, and thus solar-sail mission design is bound to be burdened with uncertainties.

This thesis addresses the significance of uncertainty quantification in solar-sail missions, focusing on the uncertainties associated with the sail's optical coefficients, structural deformation, and attitude profiles for missions in the near-Earth environment. The analysis is presented for sailcrafts in low-Earth Sun-synchronous orbits that use locally-optimal steering laws to increase their altitude or inclination [1, 2], a set of conditions that are inspired by the future Advanced Composite Solar Sail System mission [3].

The solar-sail dynamics are modelled considering the Earth's gravitational, solar radiation pressure, and aerodynamic accelerations. The solar radiation pressure acceleration is computed through the Generalized Sail Model devised by Rios-Reyes and Scheeres [4], which is used to model the acceleration of non-ideal, non-flat sails efficiently. The shape of the sail is assumed to follow the deformation model presented by Gauvain and Tyler for the Solar Cruiser spacecraft [5], which features parabolic boom deflection and membrane billowing. The aerodynamic acceleration is computed through the non-rotating flat-plate hyperthermal free-molecular flow model proposed by Storch [6]. Finally, the attitude uncertainty is modelled through two angular offsets from a nominal direction, whose evolution's are described as Ornstein-Uhlenbeck processes [7].

The analyses performed in this thesis aim to quantify the uncertainties in the altitude-increase and inclination-changing capabilities of solar sails, given some known uncertainties in the sail model parameters and attitude control profile. To achieve this, two uncertainty propagation methods are used, namely the Gauss von Mises and Monte Carlo methods. The former is a very computationally efficient σ-point method specifically designed for perturbed two-body problems [8]. The Monte Carlo method, on the other hand, achieves a higher accuracy at the cost of a larger computational effort. In light of this, the Monte Carlo method is used to validate the Gauss von Mises method or whenever the latter method cannot be employed.

The findings highlight the substantial impact of uncertainty in the sail's optical coefficients on mission performance. By considering uncertainties corresponding to the current state of the art in solar-sail manufacturing, it was found that the maximum altitude gain achievable by sailcraft in Earth-bound orbit is associated with a significant uncertainty, which can reach values even in the order of 8.1% of the altitude increase found when no uncertainties are accounted for. On the other hand, for the case of inclination-increase maneuvers, a worst-case uncertainty of 16.5% is found. The largest uncertainties in altitude gain appear for orbits with a local time of the ascending node at approximately 6 AM or 6 PM. For sailcraft performing inclination-increasing maneuvers, the largest uncertainties in mission performance appear for orbits with local time of the ascending node at approximately 2 AM and 2 PM. Among all optical coefficients, the uncertainty in specularity played the largest role in performance uncertainty, followed by the uncertainty in reflectivity. The sail's structural deformation was found to have a minimal impact on the performance uncertainty.

The analysis on attitude uncertainty revealed that the magnitude and speed of change of the solar-sail attitude offset from a nominal profile strongly impact the mean and spread of the distributions of the achieved altitude and inclination gains. The Ornstein-Uhlenbeck process was found to be an effective tool in modelling angular offsets with varying characteristics, demonstrating its flexibility and suitability for the analyses

at hand.

To the best of the author's knowledge, research on the effects of uncertainties on the solar-sail dynamics and mission design has been conducted only to a limited-first order extent for Earth-bound missions. In light of this, the findings presented in this thesis provide a thorough insight into this topic. This work highlights the importance of characterizing this uncertainty, and it provides valuable insights for improved mission planning, risk assessment, and decision-making. It additionally demonstrates novel techniques for the modelling and propagation of uncertainties, such as the use of the Ornstein-Uhlenbeck process and the Gauss von Mises method.

References

[1] M. Macdonald and C. R. Mcinnes. "Realistic Earth Escape Strategies for Solar Sailing". In: *Journal of Guidance, Control, and Dynamics* 28.2 (Apr. 2005). DOI: `10.2514/1.5165`.

[2] M. Macdonald and C. R. Mcinnes. "Analytical Control Laws for Planet-Centered Solar Sailing". In: *Journal of Guidance, Control, and Dynamics* 28.5 (Oct. 2005). DOI: `10.2514/1.11400`.

[3] W. K. Wilkie. "Overview of the NASA Advanced Composite Solar Sail System (ACS3) Technology Demonstration Project". In: *AIAA Scitech 2021 Forum*. 2021. DOI: `10.2514/6.2021-1260`.

[4] L. Rios-Reyes and D. Scheeres. "Trajectory Control for General Solar Sails". In: *AIAA Guidance, Navigation and Control Conference and Exhibit*. 2008. DOI: `10.2514/6.2008-6830`.

[5] B. M. Gauvain and D. A. Tyler. "A Solar Sail Shape Modeling Approach for Attitude Control Design and Analysis". In: *6th International Symposium on Space Sailing (ISSS)*. 2023.

[6] J. A. Storch. "Aerodynamic Disturbances on Rapidly Rotating Spacecraft in Free-Molecular Flow". In: *Engineering Construction and Operations in Challenging Environments Earth and Space 2004: Proceedings of the Ninth Biennial ASCE Aerospace Division International Conference*. American Society of Civil Engineers (ASCE), 2004, pp. 429–436. DOI: `10.1061/40722(153)60`.

[7] G. E. Uhlenbeck and L. S. Ornstein. "On the Theory of the Brownian Motion". In: *Physical Review* 36.5 (Sept. 1930), p. 823. DOI: `10.1103/PhysRev.36.823`.

[8] J. T. Horwood and A. B. Poore. "Gauss von Mises distribution for improved uncertainty realism in space situational awareness". In: *SIAM-ASA Journal on Uncertainty Quantification* 2.1 (2014), pp. 276–304. DOI: `10.1137/130917296`.

Contents

List of Figures

List of Tables

List of Abbreviations

- **ACS3**: Advanced Composite Solar Sail System
- **AU**: astronomical unit
- **ECI**: Earth-Centered Inertial
- **FoM**: figure of merit
- **GVM**: Gauss von Mises
- **J2000**: January 1st, 2000
- **JAXA**: Japanese Aerospace Exploration Agency
- **LTAN**: Local Time of the Ascending Node
- **MC**: Monte Carlo
- **MET-07**: Marshall Engineering Thermosphere 07
- **NASA**: National Aeronautics and Space Administration
- **NRLMSISE-00**: Naval Research Laboratory Mass Spectrometer and Incoherent Scatter Radar Extended
- **pdf**: probability density function
- **RTN**: Radial-Transverse-Normal
- **SMA**: semi-major axis
- **SRP**: solar radiation pressure
- **TSI**: Total Solar Irradiance

List of Symbols

- A: surface area of the solar sail
- A_v: area of the intersection of the Sun planet disks in the conincal shadow model
- A_i: area of the i-th discretized face of the solar sail
- a: semi-major axis
- a_1, a_2, a_3: Generalized Sail Model cofficients
- a_v, b_v, c_v: sides of a triangle in the conincal shadow model
- a_{ij}, b_i, c_i, d_i, d_i^*: coefficients of the stochastic Runge-Kutta integrator
- $\mathbf{a}_{\text{total}}$: total solar-sail acceleration
- $\mathbf{a}_{\mathrm{J_2}}$: acceleration due to Earth oblateness
- $\mathbf{a}_{\text{SRP}}$: solar radiation pressure acceleration
- $\mathbf{a}_{\text{aero}}$: aerodynamic acceleration
- B_f, B_b: Lambertian coefficients of the solar-sail front and back sides, respectively
- C: real constant
- $\mathcal{C}^n_P$: space of n-times continuous differentiable functions
- C_D, C_L: drag and lift coefficients
- c: speed of light
- $\hat{\mathbf{D}}$, $\hat{\mathbf{L}}$: drag and lift directions
- e: eccentricity
- F: correction factor for the finite disk of the Sun
- $\mathbf{F}_{\text{SRP}}$: solar radiation pressure force
- $\mathbf{F_r}$: force due to the reflection of photons
- $\mathbf{F_a}$: force due to absorption of photons
- $\mathbf{F_e}$: force due emission (re-radiation) of photons
- $\bar{f}$ true anomaly
- $f(t, y)$: drift term of a stochastic differential equation that defines the evolution y
- $\mathrm{GM}_\oplus$: Earth's gravitational parameter

- $\mathcal{GVM}$: (probability density function of the) Gauss von Mises distribution
- $g(x)$: function contained in the functional space $\mathcal{C}_P^n$
- h: altitude
- $\mathbf{h}$: orbital momentum vector
- $I_{\odot,1AU}$: total solar irradiance at one astronomical unit from the Sun
- i: inclination
- J_2: oblateness gravity coefficient of the Earth
- J_l, J_l^*: random variables that drawn from at every integration step of a stochastic Runge-Kutta integrator
- $\mathbf{J}^1$, $\mathbf{J}^2$, $\mathbf{J}^3$: Generalized Sail Model tensors
- k_l: auxiliary value used in the stochastic Runge-Kutta integrator
- m: mass of the sailcraft
- N_{faces}: number of faces to discretize the solar-sail surface
- N_{samples}: number of samples in a Monte Carlo simulation
- $\mathcal{N}$: (probability density function of the) Gaussian (Normal) distribution
- $\hat{\mathbf{n}}$: normal vector to the solar-sail plane with positive component towards the Sun
- $\hat{\mathbf{n}}_{\text{in}}$: inner sail normal with respect to the incident airflow
- $\hat{\mathbf{n}}_{\text{nom}}$: nominal (desired) normal direction of the sail plane
- $\hat{\mathbf{n}}_{\text{off}}$: offset (perturbed) normal direction of the sail plane
- $\hat{\mathbf{n}}_{\text{optimal}}$: optimal normal direction of the sail plane
- $\hat{\mathbf{n}}_{\text{plane,1}}$, $\hat{\mathbf{n}}_{\text{plane,2}}$: normals to the planes used to define an attitude offset
- $\bar{\mathbf{n}}$: local normal to the solar-sail surface
- $\bar{\mathbf{n}}_i$: local normal of the i-th discretized face of the solar sail
- l: boom (half-diagonal) length of the sail
- $\mathcal{O}_I(\hat{\mathbf{x}}_I, \hat{\mathbf{y}}_I, \hat{\mathbf{z}}_I)$: Earth-Centered Inertial reference frame
- $\mathcal{O}_F(\hat{\mathbf{x}}_F, \hat{\mathbf{y}}_F, \hat{\mathbf{z}}_F)$: Sail-fixed reference frame
- $\mathcal{O}_{\text{RTN}}(\hat{\mathbf{x}}_{\text{RTN}}, \hat{\mathbf{y}}_{\text{RTN}}, \hat{\mathbf{z}}_{\text{RTN}})$: Radial-Transverse-Normal reference frame
- $\mathcal{O}_S(\hat{\mathbf{x}}_S, \hat{\mathbf{y}}_S, \hat{\mathbf{z}}_S)$: Sunlight reference frame
- $\mathcal{O}_{\text{off}}(\hat{\mathbf{x}}_{\text{off}}, \hat{\mathbf{y}}_{\text{off}}, \hat{\mathbf{z}}_{\text{off}})$: angular offset reference frame
- P: solar radiation pressure
- P^*: radiation pressure of a point source

- $\{p_{\text{eq}}, f_{\text{eq}}, g_{\text{eq}}, h_{\text{eq}}, k_{\text{eq}}, \ell_{\text{eq}}\}$: modified equinoctial orbital elements
- R: gas constant
- $R_{\oplus}$: radius of the Earth
- $\mathbb{R}^n$: n-dimensional space
- $\mathbf{r}_{\odot}$: position of the Sun with respect to the sail
- $\mathbf{r}$: position of the spacecraft in the Earth-Centered Inertial reference frame
- r_p, θ_p: polar coordinates of the point p in the sail plane
- $\mathbf{S}_{\mathcal{G}}$: lower-triangular Cholesky decomposition of $\boldsymbol{\Sigma}_{\mathcal{G}}$
- $\mathbb{S}$: one-dimensional circular space
- s: solar-sail specularity coefficient
- T_w: mean surface temperature of the sail
- t: time
- $\hat{\mathbf{t}}$: tangent vector to the solar-sail plane
- $\mathcal{VM}$: (probability density function of the) von Mises distribution
- $\mathbf{v}$: velocity of the spacecraft in the Earth-Centered Inertial reference frame
- v_w: average normal air velocity
- X, Y: random variables
- $\mathbf{X}$: vector of random variables
- x_1, x_2, x_3: scalar values with evolution governed by a stochastic differential equation
- $\tilde{Y}^{(\Delta t)}$: random variable corresponding to the approximation of the random variable Y obtained with a stochastic integrator using time step Δt
- y: solution to an integration, cartesian coordinate
- y_0: initial value of y
- $\tilde{y}^{(\Delta t)}$: approximation of the solution y of an integration obtained with an integrator using time step Δt
- α, δ: pitch and clock control angles
- β_{attack}: solar-sail angle of attack
- $\beta_{\text{Br}}(t)$: one dimensional Brownian motion process
- γ_1, γ_2: angular offsets of the solar-sail attitude
- Δh, Δi: averaged final increase in altitude and inclination
- Δh_{nom}, Δi_{nom}: averaged final increase in altitude and inclination for the nominal case without uncertainties

- Δt: time step
- Δz_p: displacement of point p along the z-axis of the sail-fixed reference frame
- Δz_{tip}: displacement of the booms' tips
- Δz_{billow}: maximum displacement due to billow
- ε_f, ε_b: emissivity coefficients of the solar-sail front and back sides, respectively
- ν: shadow factor
- $\Theta_{\mathcal{G}}$: parameter of the von Mises distribution
- θ, σ: characteristic parameters of the Ornstein-Uhlenbeck process
- Λ: weak order of a stochastic integrator
- $\hat{\boldsymbol{\lambda}}_{\text{ref}}$: reference direction used to define the angular offset reference frame
- $\hat{\boldsymbol{\lambda}}_{\text{œ}}$: optimal thrust direction to maximize the rate of change of the orbital element œ
- μ_X: mean of the scalar random variable X
- $\mu_{\Delta h}$, $\mu_{\Delta i}$: mean of the distribution of the averaged final altitude and inclination increases
- $\boldsymbol{\mu}_{\mathbf{X}}$: mean vector of the vector of random variables $\mathbf{X}$
- $\boldsymbol{\mu}_{\mathcal{G}}$, $\boldsymbol{\Sigma}_{\mathcal{G}}$, $\alpha_{\mathcal{G}}$, $\boldsymbol{\beta}_{\mathcal{G}}$, $\boldsymbol{\Gamma}_{\mathcal{G}}$, and $\kappa_{\mathcal{G}}$: parameters of the Gauss von Mises distribution
- Π: order of an integrator
- ρ: solar-sail reflectivity coefficient
- ρ_{aero}: atmospheric density
- $\boldsymbol{\Sigma}_{\mathbf{X}}$: covariance matrix of the vector of random variables $\mathbf{X}$
- $\boldsymbol{\Sigma}_{\mathbf{Y},(i,i)}$: i-th diagonal element of the covariance matrix of the vector of random variables $\mathbf{Y}$
- Σ_l: diffusion term of the l-th noise source of a stochastic differential equation
- σ_{load}: solar-sail's loading parameter
- $\sigma_{\Delta h}$, $\sigma_{\Delta i}$: standard deviation of the distribution of the averaged final altitude and inclination increases
- σ_2, σ_1: sets of standard deviation of the uncertain parameters describing the sail
- σ_s: standard deviation of the specularity distribution
- σ_X: standard deviation of the random variable X
- $\sigma_{\mathbf{Y}_i}$: standard deviation of the i-ith element of the vector of random variables $\mathbf{Y}$
- σ_{st}: stationary standard deviation of the Ornstein-Uhlenbeck process
- σ_n, σ_t: normal and tangential momentum accommodation coefficients
- τ: random variable that represents an angular value
- ϕ: arbitrary map
- Ω: right ascension of the ascending node
- ω: argument of the periapsis

A

Introduction

Space exploration captivates our imagination and drives our inquisitiveness, compelling us to extend the frontiers of knowledge and embark on journeys into uncharted territories. This thesis delves into the field of solar sailing, an innovative concept in space propulsion that harnesses the power of sunlight to traverse the vast expanse of space. In particular, the many uncertainties associated with this nascent technology are investigated, and their impact on mission performance in the near-Earth environment is quantified.

A.1. Solar sailing

Solar sails represent a promising form of spacecraft propulsion offering an alternative to conventional methods that rely on the expulsion of reaction mass. Indeed, these solar sails harness the inherent momentum carried by solar photons, enabling spacecraft to traverse space without the need for propellant-based systems, in a similar fashion to how ships navigate the oceans.

The physical principle underlying solar sailing is solar radiation pressure (SRP), wherein photons transfer momentum to the sail when they are reflected or re-emitted from the sail, thus generating a propulsive acceleration. To maximize this acceleration, solar sails necessitate the interception of a significant number of photons, thus requiring the use of large sail surfaces. By increasing the sail area, the total momentum imparted by the photons is amplified, therefore resulting in enhanced acceleration and travel capabilities.

The reflectivity of the sail's surface also plays a significant role in maximizing propulsion. A solar sail should function as a near-perfect reflector, ensuring minimal energy loss during the reflection process. This requirement calls for the development of advanced materials and coating techniques that can achieve high reflectivity across a broad range of wavelengths, while also being able to withstand thermal and structural loads. By reflecting photons with minimal absorption or scattering, solar sails maximize the momentum transfer from the incoming sunlight into a desired thrust direction.

Critical to the success of solar sails is the consideration of their mass. To achieve optimal acceleration, solar sails must be constructed using lightweight materials that minimize the overall mass of the spacecraft-sail system. Low masses and moments of inertia allow the solar sail to respond more efficiently to the pressure exerted by sunlight as well as to control efforts, which translates into greater propulsion and maneuverability.

Control over the orientation of the solar sail is crucial to maneuvering: Sailcraft can increase or reduce the generated SRP acceleration, as well as orient it in a desired direction, by modifying the sail's attitude with respect to the incident sunlight. However, not all thrust directions are possible, as the thrust generated by SRP cannot be directed opposite to the direction of sunlight. Thus, unlike traditional propulsion methods, thrust magnitude and direction are not only intrinsically coupled, but also highly constrained.

Unlike conventional propulsion systems that rely on finite resources or chemical reactions, solar sails harness the inexhaustible power emitted by the Sun, which might enable previously unthought-of mission durations. Decades long station-keeping, both around planetary bodies or around Lagrange points, might only be achievable through solar sails [1–3]. Travel to distant starts, which would take decades even at relativistic velocities, may be enabled through solar photonic assists or laser-propelled light sails [4].

In summary, solar sails are a groundbreaking propulsion technology that leverages the momentum of photons to navigate space. Through strategic sail design, lightweight materials, high reflectivity, and precise control over its orientation, solar sails unlock new avenues for efficient interplanetary travel and orbital maneuvering. Thus, as humanity continues to push the boundaries of exploration, solar sailing stands as a promising frontier, enabling us to venture further into the cosmos.

A.2. Solar-sailing heritage

The concept of solar sailing originated in the early 20th century, when visionaries such as Fridrickh Tsander and Konstantin Tsiolkovsky pondered the possibility of utilizing the pressure of light for space travel [5]. Tsiolkovsky introduced the idea of propulsion through light as early as 1921, while Tsander developed more practical solar-sailing concepts in 1924. However, it was not until the 1950s that solar sailing regained the attention of the scientific community. In 1951, Carl Wiley published his theoretical research on feasible solar sailing, where he showed considerable optimism about the concept. In 1958, similar optimism would be shared by Richard Gawkin, who remarked on the elegance of solar sails arguing that the inherent practical difficulties of solar sailing were relatively small compared to other challenges associated with space travel.

Research on solar sailing would continue during the following decades, with each study further proving the potential of solar sailing. In 1976, Jerome Wright and Janice Warmke found a trajectory that would allow a spacecraft propelled solely through a solar sail to rendezvous with the Haley comet at its perihelion in only 4 years [6]. Because this perihelion passage occurred in 1986, this would require a 1982 launch, allowing for 6 years of mission development. Given the incredible scientific value of a rendezvous with the comet, the National Aeronautics and Space Administration (NASA) started working on the mission in the same year, 1976 [5]. Two propulsion systems were considered to reach the Haley comet: on the one hand, a solar sail, and, on the other, a more traditional solar-electric propulsion system. However, given the higher technology readiness level of solar-electric propulsion and, therefore, its lower mission risks, in 1977 NASA opted to drop the solar-sail concept. In spite of this, the entire mission would be cancelled a short time later due to cost issues, and NASA never achieved rendezvous with the comet.

Despite the fact that a solar sail never saw the light of space in the 1980s, the Halley comet's mission concept boosted interest for the technology. During the 1980s and 1990s further research was conducted on several solar-sail mission concepts, for applications both in the Earth-Moon environment and interplanetary regime. It was during the 1990s, however, that the first experiments on deployment of gossamer structures took place. Cosmonauts aboard the MIR space station observed the successful spin-deployment of a stowed reflector surface. Shortly after, an inflatable antenna was deployed during a Space Shuttle mission, which demonstrated the potential of deployable thin structures in space.

The first attempt at deploying an actual solar sail, a thin reflective surface whose main goal is propulsion through radiation pressure, took place in 2005, when the Planetary Society launched their solar sail in a sub-orbital rocket. However, the launcher promptly failed and thus the mission was lost [9]. The first successful solar-sail mission came only five years later, when the Japan Aerospace Exploration Agency made history with the deployment of the IKAROS solar power sail [10]. They demonstrated the feasibility of solar sailing for interplanetary propulsion and attitude control through a fly-by mission to Venus. Figure A.1 shows a photo of the deployed sail in space. A year later, NASA would also achieve success through the NanoSail-

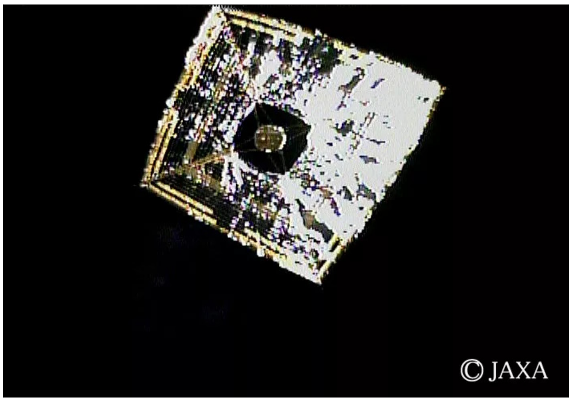

Figure A.1: Deployed IKAROS sail in space. Image credit JAXA [7].

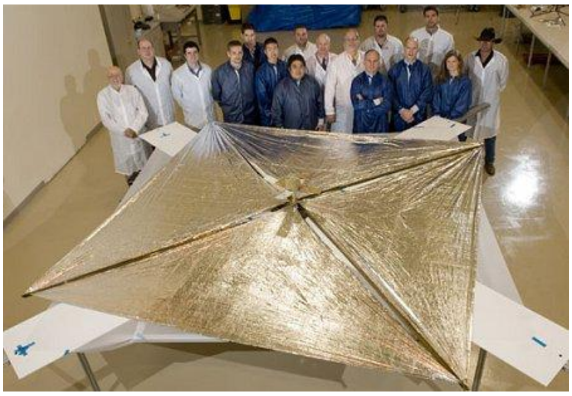

Figure A.2: Fully deployed NanoSail-D. Image credit NASA [8].

D2 mission, a solar sail in low Earth orbit whose main goal was to demonstrate the feasibility of drag sails for faster debris reentry [11]. Figure A.2 shows the deployed NanoSail-D spacecraft on Earth, which had the same configuration as NanoSail-D2.

In 2015, the Planetary Society would finally achieve successful sail deployment in low Earth orbit through the Light-Sail 1 mission, which re-entered the atmosphere after just a week in orbit [12]. Its successor, Light-Sail 2, remained in orbit from its launch date in June 2019 until reentry on November 2022 [13]. During this period, the Planetary Society was able to downlink images of the sail, which would later be used to study the deployment performance and degradation of the sail in orbit. Furthermore, they were able to perform orbit raising by a measurable amount through a solar sail, thus becoming the first mission to prove the feasibility of solar sailing as a propulsion mechanism for missions in low Earth orbit [14].

In November, 2022, the Near-Earth Asteroid (NEA) Scout mission, a CubeSat designed to fly-by and return data from a near-Earth asteroid, was launched. Unfortunately, the NEA Scout team was unable to make contact with the spacecraft, and the mission was considered lost in December, 2022, without ever leaving the Earth-Moon system [15]. Finally, solar sailing has also gained some traction on the private sector, with the newly founded “Gama” start-up promising “low-cost, reliable and scalable solar sails” for the exploration of the Solar System [16]. In January, 2023, they successfully launched and deployed their “Gama Alpha” 6U CubeSat, which was equipped with a 73.3 m^2 solar sail.

A.3. Future solar sailing missions

It took almost a century for solar sailing to evolve from the imagination of early space pioneers to reality, and it is hard to imagine what humanity will achieve in the next century through solar sailing. The solar-sail missions mentioned in the previous section proved that solar sailing has great mission-enabling potential, which will be tested in the future missions discussed in this section.

The Advanced Composite Solar Sail System (ACS3) mission will likely be the next solar-sail-propulsed spacecraft to be launched from the Earth [17, 18]. The ACS3 mission is a collaborative project lead by a team at NASA Langley; its primary objective will be the demonstration of the use of composite, hollow structural support booms. These have the advantage of being lighter and more easily stowed than metallic booms, while also reducing by two orders of magnitude the thermal deformations in space. While the ACS3 mission will feature a solar sail of approximately 75 m^2, the demonstrated boom technology will be able to support sail sizes of 500 m^2, and follow-on composite technologies are expected to be able to enable the deployment of sails with areas up to 2,000 m^2.

NASA’s Marshall Space Flight Center’s Solar Cruiser mission is intended to be a technological follow-up on the failed NEA Scout mission, mounting a much larger 1,653 m^2 sail supported by composite booms [19]. The mission objective is to demonstrate several key technologies for the future of solar sailing, such as precise attitude control through active mass translation and reflective control devices on the sail. Its proposed trajectory features a temporary stay in a sub-L$_1$ orbit, followed by a prolonged heliocentric inclination-increase maneuver. Consequently, this mission shall also demonstrate the use of solar sails for stabilized orbiting of Lagrange points and the achievement of high-inclination heliocentric orbits. Solar Cruiser is expected to serve as a pathfinder mission for a follow-on solar-sail mission to be placed in a high-inclination solar orbit [20]. This mission would be the first to produce images of the Sun's polar regions, which would be of incredible value to the heliophysics science community.

The Japan Aerospace Exploration Agency (JAXA) has also shown interest in developing new solar-sail missions. Their Oversize Kite-craft for Exploration and AstroNautics in the Outer Solar System (OKEANOS) was a proposed L-class mission that used a 2000 m^2 sail to produce thrust through photon reflection and power through ultra-thin solar cells embedded in the sail surface [21]. The sail would have rendezvous with a Trojan asteroid, where it would have released a lander to perform in-situ sample science. Unfortunately, this mission was not selected for launch due to cost concerns. However, many of the technologies developed during its conception will enable the future generation of JAXA solar sail missions. Some of the early mission concepts include the use of solar sails to enable the next JAXA sample-return mission or a 6U solar sail CubeSat deployed as a piggyback payload of a Lunar-bound spacecraft [22].

The private company Gama also has plans for future missions. While they are working on “Gama Beta”, a mission to demonstrate navigation of commercial solar sails, their more ambitious plans envision a 2030 mission, “Gama Epsilon”, which aims to be the first space exploration mission ever to reach the Oort Cloud [16]. Other organizations aim for scientific targets even further away than the Oort cloud. The “Breakthrough Initiatives”, for example, are a suite of privately-funded space science programs, among which is the “StarShot” project, which aims to visit our neighbouring star system, Alpha Centauri [4]. Their mission proposal consists of hundreds of ultra-light nanocrafts equipped with lightsails propelled by lasers beamed from the Earth. With a theoretical maximum speed of 100 million miles an hour, i.e., 20% of the speed of light, this constellation of sailcraft would reach Alpha Centauri in only 20 years. In this way, the constellation would then be able to send back to Earth images of the planet “Proxima b”. However, as one might imagine, this project has a significant number of technological challenges.

A.4. Sources of uncertainty in solar sailing

In contrast to the optimism of the early pioneers of solar sailing, real sailcraft missions have proved to be extremely difficult to design and fly. On the one hand, this has been due to the technological burdens associated with deploying large lightweight, flexible structures in space, and controlling them accurately. On the other hand, these systems are also associated with several uncertainties, which render the design of solar-sail missions highly challenging.

The force that a solar sail is able to produce depends on many factors. One of these is the amount of sunlight that reaches the sail, which depends on the distance from the sail to the Sun, the Sun's activity, and the potential shadowing of this light due to occulting bodies. Assuming that the position of the sail is known, one could assume that the distance between the Sun and the sail can be estimated with considerable accuracy. In contrast, the solar activity, or more specifically the Total Solar Irradiance (TSI), is very complicated to predict accurately. As shown in Figure A.3, the TSI presents significant rapidly and randomly evolving changes, with values approximately 1 W/m^2 smaller or larger than its yearly average. In light of this and the difficulty in predicting such alterations in the solar radiation intensity, it is inevitable to consider the TSI as an uncertainty in the solar-sail dynamics.

Shadowing of the sunlight due to the presence of the Earth and other celestial bodies is an additional

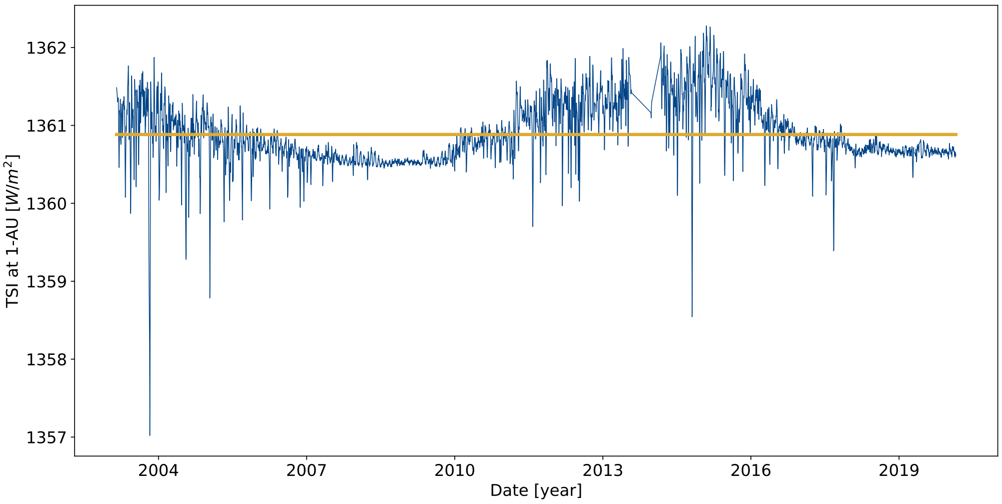

Figure A.3: Total Solar Irradiance (TSI) at 1 AU from the Sun in the 2004-2020 period. Data obtained from the SORCE mission TIM instrument [23]. The yellow line represents the average during this period.

source of uncertainty. Srivastava et al. [24] conducted a study on how the conical and cylindrical shadow models were able to predict eclipse times compared to onboard data from four low Earth orbit satellites. According to their findings, the cylindrical model tends to miss the entry and exit epochs by periods of $10-5$ s, while the conical model achieves errors of approximately 5 s. For reference, these satellites spend an average period of $16-22$ s in penumbra during each orbit, while umbra occurs for approximately 35 min. On the other hand, the work of Vokrouhlicky et al. [25] showed the effects of Earth oblateness and the atmosphere (Rayleigh scattering) on the effective shadow factor. They conducted long-term propagations including or ignoring these effects and concluded that, while considering Earth oblateness did not have a significant effect on the orbit, the atmospheric effects did have a noticeable impact [25–27]. However, their models for Rayleigh scattering heavily depend on several atmospheric parameters, which given the atmosphere seasonal and geographical dependencies and generally chaotic behaviour, should be treated as uncertain values [27]. Finally, Srivastava et al. [24, 28] considered the effects of Lunar eclipses on the solar radiation pressure and found that these eclipses are rare (between 0 and 4 per year), short (a few tens of minutes), and usually only partial; therefore, they are generally safe to neglect. Overall, however, it is clear that shadowing is difficult to predict and represent another potential source of uncertainty.

The solar radiation pressure that a sail is able to generate is also strongly dependant on its optical characteristics. The degree to which a sail is able to reflect, diffract, or absorb incoming photons depends on many factors, such as the materials being used, the degradation of the sail, imperfections in the surface (such as tears and wrinkles), the sail's attitude relative to the incoming photons, and so forth. In 2015 and 2017, Heaton and Artusio-Glimpse [29, 30] published two reviews of the optical coefficients used in the NASA solar-sail standard model, which corresponds with the optical coefficients of the NEA Scout sail. They collected data from tests performed on a specific film material and published values for the obtained effective optical coefficients. Because these results are material-dependant, they are not generally applicable to all solar-sail missions. Nevertheless, an important qualitative conclusion can be drawn: determining a sail's optical coefficients is an empirical process with associated uncertainty. On the other hand, several authors have remarked on the significant effects of solar-sail degradation for long-term missions, which cause a continuous change in the optical coefficients [31–33]. Because these models have not been verified yet through

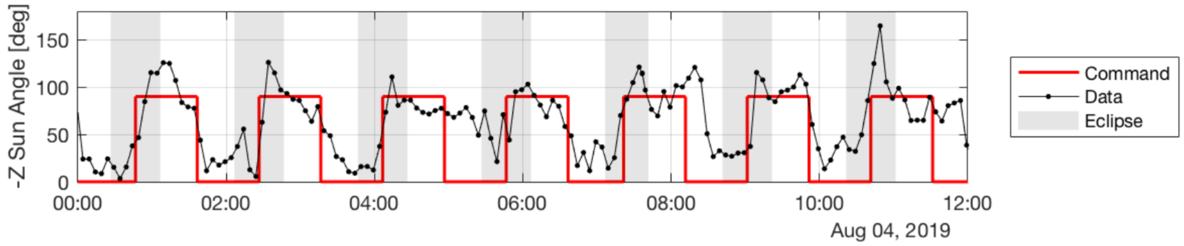

Figure A.4: Commanded and real attitude profile of the LightSail-2 mission. Figure extracted, as is, from Reference [35].

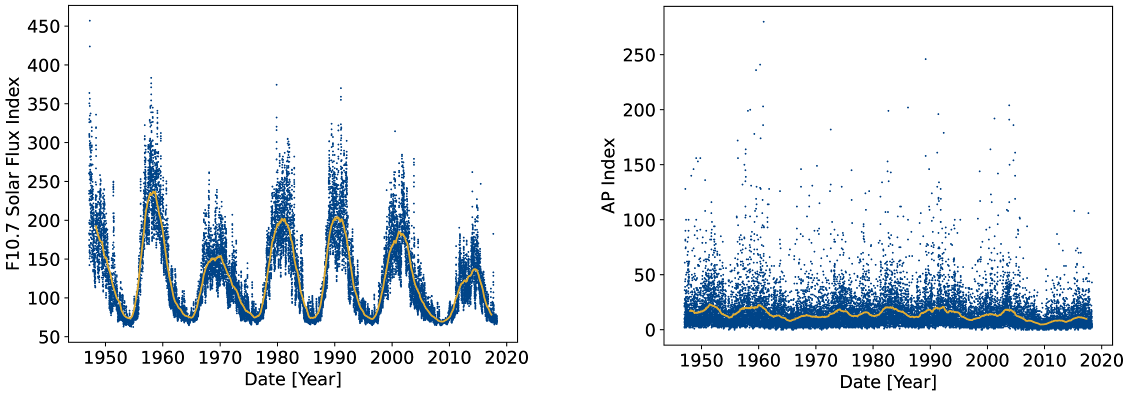

(a) Solar flux index.

(b) Geomagnetic activity index.

Figure A.5: Historic data of the daily average F10.7 and AP indices. The yellow line represents a 2-year moving average. Data from the National Centers for Environmental Information (NCEI) database [37].

mission data, it would also be sensible to treat the solar-sail degradation process as uncertain.

Finally, one of the largest unknowns in the design of real solar-sail missions is the shape that the sail's membrane assumes after its in-orbit deployment [34]. Indeed, predicting the behavior of the sail during and after its deployment is a highly complex task, as performing ground tests that perfectly replicate zero-gravity conditions is impossible. Despite this, different factors can be considered which affect the sail shape. For example, tension imbalance between support booms can lead to sail membranes being slightly skewed, while thermal deformation and aerodynamic or radiation pressure lead to boom bending and membrane billowing. Also, deployment errors and unexpected buckling can lead to deployed booms of different lengths. Finally, rapid maneuvers can cause the sail film and booms to flex and change shapes until they stabilize again. All these phenomena alter the effective surface of the sail and reflection angle with respect to sunlight, thus changing the acceleration produced. As such, it is necessary to consider the sail's shape in orbit as a highly uncertain parameter.

All the previously mentioned sources of uncertainty not only affect the force that a sail is able to produce, but also its torque. This, coupled with other factors such as sensor or actuator error, leads to the real attitude profile of a sail differing from its commanded profile. Recent flight data from the LightSail-2 mission supports this argument, as it has shown how difficult it is for solar sails to adhere even to a simple "on-off" commanded attitude profile, see Figure A.4. Moreover, following a similar rationale, the control design for the NEA Scout mission took these expected uncertainties into account and developed robust control algorithms accordingly [36]. In light of the above, a certain degree of uncertainty ought to be considered also in the attitude of a solar sail and, in particular, in its ability to follow a nominal control profile.

The large surface area of solar sails not only makes them sensitive to radiation pressure, but also causes

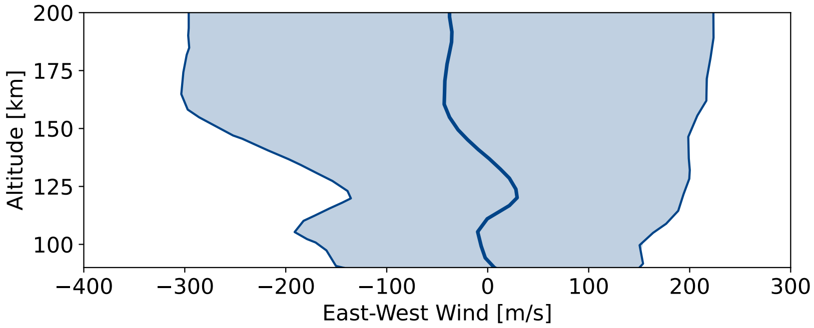

Figure A.6: Mean and 3-σ dispersion of East-West wind speed in January according to the MET-07 model. Data from Reference [38].

significant aerodynamic forces on the spacecraft. These aerodynamic forces are usually difficult to predict given how they depend on the generally chaotic behaviour of the atmosphere as well as the surface properties of the spacecraft. The atmospheric density on the thermosphere, for instance, largely depends on the geomagnetic (AP) and solar activity (F10.7) indices. Figure A.5 shows the evolution of these parameters during the past decades [37]. While some general trends can be appreciated, it is also apparent that the behaviour is chaotic and hard to predict accurately. This, in turn, makes atmospheric density predictions highly uncertain.

Similarly, the local wind speed that a sail might be subject to in the thermosphere depends on many factors. Figure A.6 displays the mean and 3-σ dispersion of the East-West wind according to the Marshall Engineering Thermosphere 07 (MET-07) model, and similar results can be obtained for the North-South and upward wind. As seen in the figure, the uncertainty associated with the wind is significant. This, in turn, impacts the velocity of the impinging flow on the sail and therefore the aerodynamic force produced.

Additionally, the shape and building materials of the spacecraft also introduce uncertainty in the aerodynamic forces. Among other factors, the drag and lift coefficients of the sail depend on the momentum accomodation coefficients of its surface. However, the literature on these coefficients suggests that they are very difficult to estimate: they depend on the surface material (and its degree of contamination), on the composition of the air (and thus altitude in the atmosphere), on the velocity of the impinging molecules, and on their incidence angle [39–41]. Knechtel and Pitts [42] performed an in-depth experimental study of the momentum accommodation coefficients for nitrogen ions impacting on aluminum. They found that these coefficients depend very strongly on the energy of the ions and the incidence angle. For instance, they reported a change in the normal coefficient from 0.4 to 0.15 when the incidence angle changes from 20 to 50 degrees. Additionally, a more expansive study was completed by Cook and Hoffbauer [39] including different gases and surface materials, which highlighted the strong dependence of these coefficients on these factors. All these studies indicate that any estimate of these coefficients is likely strongly uncertain. These findings, along with the already discussed uncertainty in sail shape, indicate that the drag and lift coefficients of the sail are bound to be uncertain.

Finally, other perturbing accelerations in the solar-sail dynamics are affected by uncertainty. Among these is the planetary radiation pressure acceleration, i.e., the acceleration due to the radiation reflected and reemitted by planetary bodies. To this date, analyses on the effect of the planetary radiation pressure acceleration on the sailcraft dynamics have been conducted only to a limited extent. There are only a few studies in the literature providing models to predict this perturbing acceleration and quantifying their accuracy. As such, there are very few papers in the literature suggesting models and quantifying their error. The most accurate models available are arguably those that consider empirical albedo and infrared radiation maps, assuming a non-ideal sail model [43]. Nevertheless, while these empirical maps provide a way to capture the geographical variability of the Earth's albedo index and infrared radiation intensity, one finds that these parameters also depend on other factors, such as the light scattering properties of the atmosphere, cloud coverage, time of the year, and so forth [44]. Because of its complex behaviour, it is difficult to exactly predict the Earth's albedo at future dates. This, along with the uncertainties on solar activity and sail configuration already discussed, makes planetary radiation pressure highly uncertain. Moreover, the lack of mission data to verify these models suggests that there might be other uncertainties that are yet to be discovered and quantified. The upcoming ACS3 mission may be the first solar sail to employ calibration steering laws to provide some insight into the real forces caused by planetary radiation pressure on sailcraft [45].

In conclusion, the forces acting on a solar sail in the Earth environment are riddled with uncertainty. While future technology development and experimental data will help ameliorate the effects of these uncertainties, currently the design of solar sail missions should take into account these uncertainties and plan for their effect on mission performance.

A.5. Studies on uncertainty in solar sailing

The issue of significant uncertainties in solar-sail mission design has been identified and investigated in the literature before. For instance, Yamaguchi et al. [46] discussed the challenges of developing precise solar-sail force models on the ground and proposed estimation strategies based on orbital data. They argued that certain factors that influence the solar radiation pressure force, like wrinkles, billowing, or material degradation, are difficult to predict on ground, and thus should be treated as uncertain parameters to be estimated from flight data.

Eldad et al. [47] developed robust attitude control algorithms that account for uncertainties in sail deformation, moment of inertia, and effective reflectivity. They remark on the difficulties of ground-testing fully deployed sails, as sail structures are designed for zero-gravity environments. Consequently, fully characterizing their flexible behaviour, and thus their shape and torque, is impossible. In response, they argued for a robust attitude control strategy that would account for this uncertainty.

Nicolai et al. [48] presented a study on the impact of uncertain optical parameters and solar irradiance on heliocentric solar-sail trajectories. Their study was the first to attempt to quantify the impact of thrust vector uncertainty on solar-sail trajectories. In doing so, they neglected degradation effects on the sail material, billowing of the structure, and did not consider any kind of attitude uncertainty. They employed a generalized polynomial chaos procedure for uncertainty propagation and showed that the specularity optical coefficient constitutes the largest source of uncertainty for heliocentric trajectories.

Finally, Oguri et al. [36] devised a robust trajectory design for the NEA Scout mission, considering uncertainty in the SRP thrust vector. They developed robust attitude profiles under the assumption that the generated force magnitude and direction might be uncertain. Based on estimates from the NEA Scout guidance, navigation and control team, they assumed a pointing error with standard deviation of 1.5 deg and thrust magnitude error of 1.5%. Their stochastic approach achieved resilient trajectories able to meet the mission requirements.

As one can see, the current body of research concerning uncertainty in solar sails encompasses only heliocentric trajectories, neglecting the Earth's orbital domain. In light of this, the research presented in this thesis aims to fill this knowledge gap by investigating the impact of uncertainty in this uncharted environment.

A.6. Uncertainty propagation

Uncertainty propagation algorithms allow one to propagate some known uncertainty about a system so as to determine the uncertainty in some figure of merit that is of interest. For example, when the solar-sail dynamics are considered, uncertainties in the sail's optical coefficients and attitude can be propagated to assess their impact on a sailcraft's ability to raise its orbit, as indicated by the altitude increase achieved after a given amount of time. The distribution of the input uncertainties must be known a priori, while the distribution of the output uncertainty is approximated by the results of the uncertainty propagation process. There exist many uncertainty propagation methods in the literature, the most significant of which are presented hereinafter.

Solving the Fokker-Planck equation allows one to obtain exact solutions to the evolution of uncertainty, but this method is still considered computationally prohibitive for astrodynamics [49, 50]. In contrast, linearization methods linearize the dynamics in order to find an analytical expression for the propagation of covariance matrices, which make them very computationally efficient [51, 52]. However, these methods generally lack accuracy for very non-linear systems like the perturbed two-body problem.

Sample-based methods are those algorithms that propagate a finite number of samples of the input uncertainty to obtain information about the output uncertainty. Monte Carlo (MC) simulations are the most well-known sample-based technique for uncertainty propagation; the rely on randomly drawing a large amount of samples from the input uncertainties. σ-point methods, on the other hand, employ a small set of samples chosen ad hoc to produce as much information about the output distribution as possible. These methods make assumptions about the shape of the output distribution, which can be a source of inaccuracy if the chosen shape does not correspond with the real shape of the distribution.

The unscented transform method is an example of a σ-point method. This algorithm is based on a generalization of the Kalman filter for non-linear systems and it assumes that the output distribution is normally distributed [53, 54]. For perturbed two-body problems, however, this assumption is not justified, as orbital uncertainties usually lie on a non-Gaussian banana-shaped arc [55]. The Gauss von Mises (GVM) method, another σ-point algorithm, aims to account for this effect by carefully selecting the system with which to represent the spacecraft's state and by assuming a different output distribution shape [56].

Polynomial chaos expansion methods approximate the map that propagates inputs to outputs of interest through a finite series of polynomials [57, 58]. However, the computational cost of the PCE method grows exponentially with the number of dimensions of the problem and the desired accuracy, which leads to large computational costs for astrodynamic problems [55].

The previously discussed linearization methods can be understood as a first-order Taylor expansion method of the solution of the propagation. Other methods attempt to provide higher-order expansions to improve on the accuracy of linearization methods. Both the state-transition tensor and differential algebra methods aim to achieve this. The state-transition tensor method is based on integrating partial derivatives of the system's dynamics along the trajectory [59]. Differential algebra, on the other hand, avoids the issue of having to find analytical expressions for the partial derivatives of the dynamics. Instead, it leverages a new set of algebra that is capable of obtaining a Taylor expansion for an arbitrarily complex function by building from the Taylor expansions of a limited set of fundamental functions [60].

This work focuses on the use of the MC and GVM methods for uncertainty propagation. As a σ-point method, the GVM method is very computationally efficient and allows one to treat the propagation as a black-box. The MC method, on the other hand, is used whenever the GVM method is not applicable and as a validation tool for the GVM method. Despite its large computational cost, the MC method has been chosen as it can provide high-fidelity results, is very simple to implement, and is well understood in the engineering community. As such, this thesis stands to provide the first validation of the efficient GVM method for uncertainty propagation for solar-sail mission design.

A.7. Research questions

This section introduces the research questions to be addressed in this thesis. These questions were drawn after analyzing the previously discussed existing knowledge gaps in the literature and considering what might be of interest for future solar-sail missions in the near-Earth environment.

- Q1. Which of the uncertainty sources affecting the solar radiation pressure acceleration is the strongest?

- Q2. How does each of the sources of uncertainty affect the achievable altitude and inclination change after a maneuver (which are key figures of merit)?
- Q3. Is there significant coupling between different uncertainty sources? To what extent can one approximate the combined effect of all uncertainty sources be approximated by considering a reduced number of sources (can some sources of uncertainty be neglected)?
- Q4. How does the uncertainty in figures of merit evolve in time?
- Q5. Is the Gauss von Mises uncertainty propagation method an accurate estimator of uncertainty?
- Q6. How does the answer to previous questions change when considering different orbits, mission dates, or figures of merit?

A.8. Thesis structure

Hereinafter the main content of the thesis is presented. This content is structured as a paper, which will be submitted to a relevant journal following the defense of this thesis. In light of this, the “Paper” Chapter B is organized in a format amenable for publication. It features a brief introduction, Section 1, which might re-estate some of the concepts introduced in the thesis’ “Introduction” Chapter A. This is followed by a section on the dynamical models considered in this work, introducing relevant reference frames, forces acting on the sail, and attitude control algorithms, see Section 2. Then, a section on uncertainty modelling is presented, which describes the sail’s optical coefficient, shape, and attitude uncertainties, see Section 3. This section also covers the uncertainty propagation algorithms used in the rest of the work. Following, Sections 4 and 5 present the analysis on the effect of these uncertainties on selected figures of merit for mission design. Some brief conclusions to the work presented in the paper are given next, see Section 6, which are immediately followed by the more expansive “Conclusion” Chapter C. This focuses on conclusions of the entire thesis project, addressing how the research questions were answered and possible future work on the topic. Finally, a series of appendices are presented, see Appendices D-J. These mostly cover implementation details and further details on the methodology that were deemed not crucial for the paper to be published.

Introduction Bibliography

[1] D. Lawrence and S. Piggott. “Solar sailing trajectory control for Sub-L1 stationkeeping”. In: *AIAA Guidance, Navigation, and Control Conference and Exhibit.* 2004.

[2] M. Macdonald et al. “Solar Polar Orbiter: A Solar Sail Technology Reference Study”. In: *Journal of Spacecraft and Rockets* 43 (2006). DOI: `10.2514/1.16408`.

[3] M. Leipold et al. “Mercury sun-synchronous polar orbiter with a solar sail”. In: *Acta Astronautica* 39 (July 1996), pp. 143–151. DOI: `10.1016/S0094-5765(96)00131-2`.

[4] *Breakthrough Initiatives.* Accessed July 31, 2023. URL: `https://breakthroughinitiatives.org/`.

[5] C. R. Mcinnes. *Solar sailing: technology, dynamics and mission applications.* Springer Science & Business Media, 2004.

[6] J. Wright and J. Warmke. “Solar sail mission applications”. In: *Astrodynamics Conference.* Guidance, Navigation, and Control and Co-located Conferences. American Institute of Aeronautics and Astronautics, Aug. 1976. DOI: `10.2514/6.1976-808`.

[7] Japan Aerospace Exploration Agency. *Small Solar Power Sail Demonstrator 'IKAROS' Successful Image Shooting by Separation Camera.* Accessed July 31, 2023. 2010. URL: `https://global.jaxa.jp/press/2010/06/20100616_ikaros_e.html`.

[8] NASA Science. *NASA to Attempt Historic Solar Sail Deployment | Science Mission Directorate.* Accessed July 31, 2023. 2008. URL: `https://science.nasa.gov/science-news/science-at-nasa/2008/26jun_nanosaild/`.

[9] NBC News. *Russians say solar-sail vehicle was lost.* Accessed July 31, 2023. 2005. URL: `https://www.nbcnews.com/id/wbna8304717`.

[10] Y. Tsuda et al. “Achievement of IKAROS Japanese deep space solar sail demonstration mission”. In: *Acta Astronautica* 82.2 (Feb. 2013), pp. 183–188. DOI: `10.1016/J.ACTAASTRO.2012.03.032`.

[11] G. Vulpetti, L. Johnson, and G. L. Matloff. “The NanoSAIL-D2 NASA Mission”. In: *Solar Sails* (2015), pp. 173–178. DOI: `10.1007/978-1-4939-0941-4_16`.

[12] R. Ridenoure et al. “LightSail Program Status: One Down, One to Go”. In: *Small Satellite Conference.* Aug. 2015.

[13] B. H. Betts et al. “LightSail 2 Image-Based Engineering Assessment”. In: *6th International Symposium on Space Sailing (ISSS).* 2023.

[14] J. R. Mansell et al. “LightSail 2 Orbit Evolution and Attitude Control Performance”. In: *6th International Symposium on Space Sailing (ISSS).* 2023.

[15] D. Dickinson. *Status Update: Artemis 1's CubeSat Missions.* Accessed July 31, 2023. Dec. 2022. URL: `https://skyandtelescope.org/astronomy-news/status-update-artemis-1s-smallsat-missions/`.

[16] Gama. *Gama - enabling deep space.* Accessed July 31, 2023. 2023. URL: `https://www.gamaspace.com/`.

[17] W. K. Wilkie. “Overview of the NASA Advanced Composite Solar Sail System (ACS3) Technology Demonstration Project”. In: *AIAA Scitech 2021 Forum.* 2021. DOI: `10.2514/6.2021-1260`.

[18] L. Hall. *Advanced Composite Solar Sail System.* Accessed July 31, 2023. 2021. URL: `http://www.nasa.gov/directorates/spacetech/small_spacecraft/ACS3`.

[19] NASA Science. *Solar Cruiser: Enabling new vistas for Heliophysics Science | Science Mission Directorate.* Accessed July 31, 2023. Jan. 2023. URL: `https://science.nasa.gov/heliophysics/programs/solar-cruiser`.

[20] J. B. Pezent et al. “Preliminary trajectory design for NASAs Solar Cruiser: A technology demonstration mission”. In: *Acta Astronautica* 183 (June 2021), pp. 134–140. DOI: `10.1016/J.ACTAASTRO.2021.03.006`.

[21] O. Mori et al. “Solar power sail mission of OKEANOS”. In: *Astrodynamics* 4.3 (Sept. 2020), pp. 233–248. DOI: `10.1007/S42064-019-0067-8`.

[22] O. Mori et al. “New Solar Power Sail Program in the Post-OKEANOS Era”. In: *6th International Symposium on Space Sailing (ISSS).* 2023.

[23] G. Kopp. *SORCE Total Solar Irradiance Data - SORCE.* Accessed July 31, 2023. 2020. URL: `https://lasp.colorado.edu/home/sorce/data/tsi-data/`.

[24] V. K. Srivastava et al. “Eclipse prediction methods for LEO satellites with cylindrical and cone geometries: A comparative study of ECSM and ESCM to IRS satellites”. In: *Astronomy and Computing* 2 (2013), pp. 11–17. DOI: `10.1016/J.ASCOM.2013.06.001`.

[25] D. Vokrouhlicky et al. “Effects of the Earth’s polar flattening on the shadow structure and the penumbra transitions.” In: *Astronomy and Astrophysics* 307 (1996), pp. 635–644.

[26] D. Vokrouhlicky, P. Farinella, and F. Mignard. “Solar radiation pressure perturbations for Earth satellites. III. Global atmospheric phenomena and the albedo effect”. In: *Astronomy and Astrophysics* 290 (1994), pp. 324–334.

[27] D. Vokrouhlicky et al. “Solar radiation pressure perturbations for Earth satellites. I: A complete theory including penumbra transitions”. In: *Astronomy and Astrophysics* 280 (1993), pp. 295–312.

[28] V. K. Srivastava et al. “Lunar shadow eclipse prediction models for the Earth orbiting spacecraft: Comparison and application to LEO and GEO spacecrafts”. In: *Acta Astronautica* 110 (2015), pp. 206–213. DOI: `10.1016/J.ACTAASTRO.2015.01.020`.

[29] A. F. Heaton and A. Artusio-Glimpse. “An update to the NASA reference solar sail thrust model”. In: *AIAA SPACE 2015 conference and exposition.* 2015.

[30] A. F. Heaton, N. Ahmad, and K. Miller. “Near Earth Asteroid Scout thrust and torque model”. In: *4th International Symposium on Solar Sailing (ISSS).* 2017.

[31] B. Dachwald et al. “Impact of Optical Degradation on Solar Sail Mission Performance”. In: *Journal of Spacecraft and Rockets* 44 (May 2007), pp. 740–749. DOI: `10.2514/1.21432`.

[32] M. A. Rozhkov, O. L. Starinova, and I. V. Chernyakina. “Influence of optical parameters on a solar sail motion”. In: *Advances in Space Research* 67 (May 2021), pp. 2757–2766. DOI: `10.1016/j.asr.2020.06.017`.

[33] B. Dachwald et al. “Parametric model and optimal control of solar sails with optical degradation”. In: *Journal of Guidance, Control, and Dynamics* 29 (2006), pp. 1170–1178. DOI: `10.2514/1.20313`.

[34] B. M. Gauvain and D. A. Tyler. “A Solar Sail Shape Modeling Approach for Attitude Control Design and Analysis”. In: *6th International Symposium on Space Sailing (ISSS).* 2023.

[35] J. R. Mansell et al. “Orbit and attitude performance of the lightsail 2 solar sail spacecraft”. In: *AIAA Scitech 2020 Forum* 1 Part F (2020), pp. 1–18. DOI: `10.2514/6.2020-2177`.

[36] K. Oguri, G. Lantoine, and T. H. Sweetser. “Robust Solar Sail Trajectory Design under Uncertainty with Application to NEA Scout Mission”. In: *AIAA SCITECH 2022 Forum*. 2022, pp. 16–27.

[37] National Centers for Environmental Information. *Data and products*. Dec. 2005.

[38] P. W. White and J. Hoffman. *Earth Global Reference Atmospheric Model (Earth-GRAM): User Guide*. Tech. rep. NASA, Marshall Space Flight Center, 2021.

[39] S. R. Cook and M. A. Hoffbauer. *Measurement of Momentum Transfer Coefficients for H2, N2, CO, and CO2 Incident Upon Spacecraft Surfaces*. Tech. rep. NASA, Lyndon B. Johnson Space Center, 1997.

[40] D. Mostaza Prieto, B. P. Graziano, and P. C. Roberts. “Spacecraft drag modelling”. In: *Progress in Aerospace Sciences* 64 (2014), pp. 56–65. DOI: `10.1016/J.PAEROSCI.2013.09.001`.

[41] R. M. Fredo and M. H. Kaplan. “Procedure for obtaining aerodynamic properties of spacecraft”. In: *Journal of Spacecraft and Rockets* 18.4 (1981), pp. 367–373. DOI: `10.2514/3.28061`.

[42] E. D. Knechtel and W. C. Pitts. “Normal and Tangential Momentum Accommodation for Earth Satellite Conditions”. In: *Astronautica Acta* 18.3 (1973).

[43] L. Carzana, P. Visser, and J. Heiligers. “A New Model for the Planetary Radiation Pressure Acceleration for Solar Sails”. In: *2022 AAS/AIAA Astrodynamics Specialist Conference*. 2022.

[44] P. R. Goode et al. “Earthshine observations of the earth’s reflectance”. In: *Geophysical Research Letters* 28.9 (2001), pp. 1671–1674. DOI: `10.1029/2000GL012580`.

[45] L. Carzana et al. “Solar-sail Steering Laws to Calibrate the Accelerations from Solar Radiation Pressure, Planetary Radiation Pressure, and Aerodynamic Drag”. In: *6th International Symposium on Solar Sailing (ISSS)*. 2023.

[46] T. Yamaguchi et al. “Trajectory Analysis of Small Solar Sail Demonstration Spacecraft IKAROS Considering the Uncertainty of Solar Radiation Pressure”. In: *Transactions of the Japan Society for Aeronautical and Space Sciences* 8.ists27 (2010), 37–43. DOI: `10.2322/TASTJ.8.PD_37`.

[47] O. Eldad, E. G. Lightsey, and C. Claudel. “Minimum-time attitude control of deformable solar sails with model uncertainty”. In: *Journal of Spacecraft and Rockets* 54.4 (June 2017), pp. 863–870. DOI: `10.2514/1.A33713`.

[48] L. Niccolai et al. “Effects of optical parameter measurement uncertainties and solar irradiance fluctuations on solar sailing”. In: *Advances in Space Research* 67.9 (May 2021), pp. 2784–2794. DOI: `10.1016/J.ASR.2019.11.037`.

[49] M. Kumar, S. Chakravorty, and J. L. Junkins. “A semianalytic meshless approach to the transient Fokker-Planck equation”. In: *Probabilistic Engineering Mechanics* 25.3 (July 2010), pp. 323–331. DOI: `10.1016/J.PROBENGMECH.2010.01.006`.

[50] Y. Sun and M. Kumar. “Uncertainty propagation in orbital mechanics via tensor decomposition”. In: *Celestial Mechanics and Dynamical Astronomy* 124.3 (Mar. 2016), pp. 269–294. DOI: `10.1007/s10569-015-9662-z`.

[51] P. S. Maybeck. *Stochastic models, estimation, and control Vol 1*. Academic Press, 1979.

[52] J. Taylor. “Handbook for the direct statistical analysis of missile guidance systems via CADET”. In: *Analytic Sciences Corporation* 13397 (1975).

[53] S. J. Julier, J. K. Uhlmann, and H. F. Durrant-Whyte. “A new method for the nonlinear transformation of means and covariances in filters and estimators”. In: *IEEE Transactions on Automatic Control* 45.3 (2000), pp. 477–482. DOI: `10.1109/9.847726`.

[54] S. J. Julier and J. K. Uhlmann. “Unscented filtering and nonlinear estimation”. In: *Proceedings of the IEEE*. Vol. 92. 3. Mar. 2004, pp. 401–422. DOI: `10.1109/JPROC.2003.823141`.

[55] Y. zhong Luo and Z. Yang. “A review of uncertainty propagation in orbital mechanics”. In: *Progress in Aerospace Sciences* 89 (Feb. 2017), pp. 23–39. DOI: `10.1016/j.paerosci.2016.12.002`.

[56] J. T. Horwood, N. D. Aragon, and A. B. Poore. “Gaussian sum filters for space surveillance: theory and simulations”. In: *Journal of Guidance, Control, and Dynamics* 34.6 (2011), pp. 1839–1851.

[57] B. A. Jones and A. Doostan. “Satellite collision probability estimation using polynomial chaos expansions”. In: *Advances in Space Research* 52.11 (Dec. 2013), pp. 1860–1875. DOI: `10.1016/j.asr.2013.08.027`.

[58] B. A. Jones, A. Doostan, and G. H. Born. “Nonlinear propagation of orbit uncertainty using non-intrusive polynomial chaos”. In: *Journal of Guidance, Control, and Dynamics* 36.2 (2013), pp. 430–444. DOI: `10.2514/1.57599`.

[59] R. S. Park and D. J. Scheeres. “Nonlinear mapping of Gaussian statistics: Theory and applications to spacecraft trajectory design”. In: *Journal of Guidance, Control, and Dynamics* 29.6 (2006), pp. 1367–1375. DOI: `10.2514/1.20177`.

[60] M. Berz. “Differential Algebraic Techniques”. In: *Advances in Imaging and Electron Physics* 108.C (Jan. 1999), pp. 81–117. DOI: `10.1016/S1076-5670(08)70228-3`.

B

Paper

Uncertainty quantification for solar sails in the near-Earth environment

Juan Garcia-Bonilla[1,a]

[a] *Faculty of Aerospace Engineering, Delft University of Technology, Delft, the Netherlands*

Abstract

Solar sailing is a promising propellantless propulsion method that employs large reflective surfaces to harness solar radiation pressure for spacecraft propulsion. Despite the fact that several solar-sail near-Earth missions will launch in the coming years, there is notable lack of published studies on the uncertainties associated with missions of this kind. This paper addresses this gap in knowledge by quantifying uncertainties related to the solar sail's optical coefficients, structural deformations, and attitude profiles. Through two uncertainty propagation methods, namely Monte Carlo simulations and the Gauss von Mises method, the study reveals the significant impact of the optical coefficient uncertainties on mission performance. The results indicate a worst-case 3-σ uncertainty of 8.1% in altitude gain and 16.5% uncertainty in inclination gain for the NEA Scout solar sail model. Specularity coefficient uncertainty emerges as the primary driver of performance uncertainty among the analyzed optical coefficients. Structural deformation, on the other hand, exerts minimal impact. Uncertainty in the attitude profile is modelled through Ornstein-Uhlenbeck processes and is found to impact mean mission performance as well as introduce performance uncertainty. Overall, this work demonstrates the critical importance of characterizing uncertainties and provides insights crucial for mission planning and decision-making.

Keywords: Solar sailing; near-Earth environment; Uncertainty quantification; Gauss von Mises; Stochastic Differential Equation

---

1. Introduction

Solar sailing is a concept that originated in the early 20th century and has since drawn the interest of space enthusiasts and researchers. A solar sail offers a promising means of propellantless propulsion by harnessing the pressure of light for space travel. While solar sailing missions have demonstrated remarkable achievements in the last two decades, the design and execution of real sailcraft missions remain challenging. These challenges stem, among others, from the technological complexities of deploying and controlling large flexible structures in space, as well as the uncertainties inherent to solar-sail systems. This

---

[1] Corresponding author: juan@garciabonilla.com

papers addresses these uncertainties, hoping to provide a comprehensive understanding of their effect on solar-sail missions in the near-Earth environment.

One primary source of uncertainty in solar sailing lies in the estimation of the solar radiation pressure (SRP) acceleration. The acceleration generated by a solar sail depends on multiple factors, including the amount of light reaching the sail, which is influenced by the distance from the Sun, solar activity, and potential shadowing due to occulting bodies. The solar irradiance, which depends on the solar activity, exhibits complex temporal variations that are challenging to predict accurately [1]. Moreover, shadowing caused by the Earth or other celestial bodies introduces additional uncertainty, as estimating the exact duration and impact of shadowing events is inherently difficult [2].

Uncertainty is also present in knowledge of the optical characteristics of the sail's surface and their variation in time. Factors such as the sail's material properties, its degradation, surface imperfections, and attitude relative to incoming photons influence the reflectivity, diffraction, and absorption of light. Determining precise optical coefficients is an empirical process, subject to uncertainty and continuous change due to material degradation over time [3–5].

Sail deployment and control in space present further challenges. The behavior of sail membranes and supporting structures in zero-gravity environments is difficult to predict accurately from Earth. Factors such as tension imbalances, thermal deformations, aerodynamic pressures, and deployment errors can affect the sail's shape, leading to uncertainties in its effective illuminated surface and therefore the exerted force and torque [6].

The attitude control of a solar sail is also subject to uncertainties. Attitude data from the LightSail-2 mission has demonstrated that real sailcraft often deviate from nominal attitude profiles due to the complexity of maintaining precise control of these structures with large moments of inertia [7]. Deviation from the desired attitude introduces uncertainties in the generated acceleration and thus in the overall mission performance.

Existing studies have shed light on uncertainty in solar sailing, solely focusing on heliocentric trajectories and neglecting the Earth's orbital domain [1]. This paper aims to fill this knowledge gap by investigating the impact of uncertainty in Earth-bound solar sail missions. In particular, three primary sources of uncertainty are considered, namely the uncertainties in the optical coefficients, sail deformation, and attitude errors. Quantifying the effects of these uncertainties on mission performance will contribute to improve the design capabilities of future solar-sail missions and, in particular, their robustness. This will allow space agencies and companies to exploit the full potential of solar sailing and enable novel mission applications.

Following this introduction, the next sections discuss the models, analyses, results and conclusions of this paper. The dynamical model considered in this work is presented in Section 2, where the relevant reference frames, solar-sail accelerations, and attitude control algorithms are introduced. Then, a section discussing the modeling and propagation of the solar sail's optical coefficient, shape, and attitude uncertainties is presented, see Section 3.

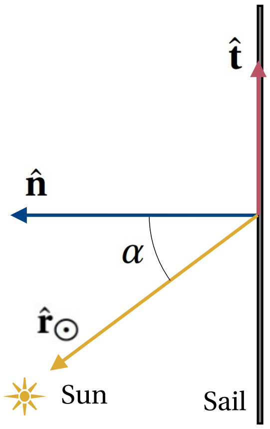

Figure 1: Sketch of relevant vectors for the dynamics of a solar sail.

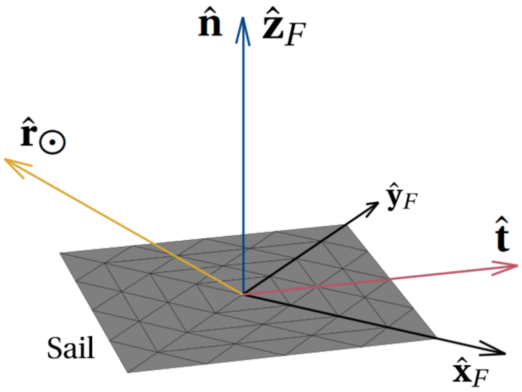

Figure 2: Sail-fixed reference frame $\mathcal{O}_F(\hat{\mathbf{x}}_F, \hat{\mathbf{y}}_F, \hat{\mathbf{z}}_F)$.

Results for the effect of these uncertainties on selected figures of merit (FoMs) for mission design are presented in the following sections, see Sections 4 and 5. Some brief conclusions to the work presented in the paper are given next, see Section 6.

2. Dynamical model

This section introduces the relevant reference frames used in this paper, followed by a comprehensive review of the models used to compute the acceleration acting on the sail. Finally, the attitude control algorithms considered are explained.

2.1. Reference frames

This section introduces the reference frames used in this paper to express the dynamics of the solar sail.

Earth-Centered Inertial reference frame

The Earth-Centered Inertial (ECI) reference frame, $\mathcal{O}_I(\hat{\mathbf{x}}_I, \hat{\mathbf{y}}_I, \hat{\mathbf{z}}_I)$, is an inertial frame centered at the Earth's center of mass, used to propagate the dynamics of the sailcraft. The frame has its $\hat{\mathbf{x}}_I$ axis pointing towards the mean vernal equinox on January 1st, 2000 (J2000). The $\hat{\mathbf{z}}_I$ axis is perpendicular to the mean equatorial plane on J2000 and points towards the North Hemisphere. Finally, the $\hat{\mathbf{y}}_I$ axis completes the right-handed reference frame.

Sail-fixed reference frame

Figure 1 shows the vectors used in the definition of the sail-fixed reference frame. Note that, while this work assumes that the solar sail may be deformed, a flat (undeformed) sail plane is still used throughout this paper for the development of theory. $\hat{\mathbf{n}}$ is the normal vector to this sail plane, with positive component in the direction of the Sun, $\hat{\mathbf{r}}_\odot$ indicates the sail-to-Sun direction, and $\hat{\mathbf{t}}$ is the tangent vector to the sail plane, which is contained in the plane defined by $\hat{\mathbf{n}}$ and $\hat{\mathbf{r}}_\odot$ and points away from the Sun. Finally, α is the pitch angle, defined as the angle between $-\hat{\mathbf{n}}$ and $\hat{\mathbf{r}}_\odot$.

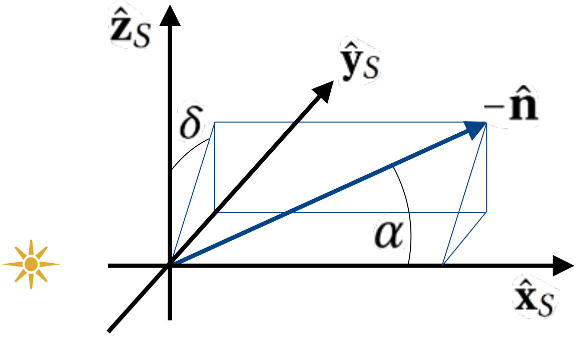

Figure 3: Sunlight reference frame and solar-sail control angles: the pitch angle α and clock angle δ.

The sail-fixed reference frame, $\mathcal{O}_F(\hat{\mathbf{x}}_F, \hat{\mathbf{y}}_F, \hat{\mathbf{z}}_F)$, is a non-inertial reference frame centered at the spacecraft. As displayed in Figure 2, the $\hat{\mathbf{z}}_F$ axis points in the direction of the solar-sail normal vector $\hat{\mathbf{n}}$, the $\hat{\mathbf{x}}_F$ axis points along the direction of one of the booms of the sail (arbitrarily chosen, without loss of generality), and finally, $\hat{\mathbf{y}}_F$ completes the right-handed reference frame.

Radial-Transverse-Normal reference frame

The Radial-Transverse-Normal (RTN) reference frame, $\mathcal{O}_{\text{RTN}}(\hat{\mathbf{x}}_{\text{RTN}}, \hat{\mathbf{y}}_{\text{RTN}}, \hat{\mathbf{z}}_{\text{RTN}})$, is a non-inertial reference frame centered at the spacecraft. The $\hat{\mathbf{x}}_{\text{RTN}}$ axis points along the position of the spacecraft in the ECI reference frame, $\hat{\mathbf{r}}$. The $\hat{\mathbf{z}}_{\text{RTN}}$ axis is directed along the orbital angular momentum vector, $\hat{\mathbf{h}} = (\mathbf{r} \times \mathbf{v})/||\mathbf{r} \times \mathbf{v}||$, where $\mathbf{r}$ and $\mathbf{v}$ are the position and velocity vectors of the sailcraft. The $\hat{\mathbf{y}}_{\text{RTN}}$ axis completes the right-handed reference frame.

Sunlight reference frame

The Sunlight reference frame, $\mathcal{O}_S(\hat{\mathbf{x}}_S, \hat{\mathbf{y}}_S, \hat{\mathbf{z}}_S)$, is a non-inertial reference frame centered at the spacecraft, first introduced by Macdonald and McInnes [8]. The $\hat{\mathbf{x}}_S$ axis points in the Sun-to-sailcraft direction (i.e., the direction of sunlight). The $\hat{\mathbf{y}}_S$ axis corresponds to the heliocentric velocity vector of the Earth, and the $\hat{\mathbf{z}}_S$ axis completes a right-handed reference frame.

This reference frame is used to define the sail's control angles, namely the pitch angle α and clock angle δ, as shown in Figure 3. Within this frame, the pitch angle α is the angle between the sail's normal, $-\hat{\mathbf{n}}$, and the $\hat{\mathbf{x}}_S$ axis, while the clock angle δ is measured between the $\hat{\mathbf{z}}_S$ axis and the projection of the opposite to the normal direction, $-\hat{\mathbf{n}}$, to the $(\hat{\mathbf{y}}_S,\ \hat{\mathbf{z}}_S)$ plane.

Angular offset reference frame

The angular offset reference frame, $\mathcal{O}_{\text{off}}(\hat{\mathbf{x}}_{\text{off}}, \hat{\mathbf{y}}_{\text{off}}, \hat{\mathbf{z}}_{\text{off}})$, is a non-inertial reference frame centered at the spacecraft that is used to conveniently define angular offsets from a reference direction, $\hat{\boldsymbol{\lambda}}_{\text{nom}}$. Within this frame, the $\hat{\mathbf{z}}_{\text{off}}$ axis corresponds to the reference direction, $\hat{\mathbf{z}}_{\text{off}} = \hat{\boldsymbol{\lambda}}_{\text{nom}}$, and the $\hat{\mathbf{x}}_{\text{off}}$ axis is directed perpendicular to $\hat{\mathbf{z}}_{\text{off}}$ and lies in the plane defined by $\hat{\mathbf{z}}_I$ and $\mathbf{r}_\odot$:

$$\hat{\mathbf{x}}_{\text{off}} = \frac{\hat{\boldsymbol{\lambda}}_{\text{nom}} \times (\hat{\mathbf{z}}_I \times \mathbf{r}_\odot)}{\left|\left|\hat{\boldsymbol{\lambda}}_{\text{nom}} \times (\hat{\mathbf{z}}_I \times \mathbf{r}_\odot)\right|\right|} \tag{1}$$

Finally, the $\hat{\mathbf{y}}_{\text{off}}$ axis completes the right-handed reference frame.

Because the Sun's position in the inertial reference frame remains approximately constant for short periods of time, the vector $(\hat{\mathbf{z}}_I \times \mathbf{r}_\odot)$ can also be considered constant. Moreover, the use of the Sun's position, $\mathbf{r}_\odot$, makes it so that the reference frame is never ill-defined for the case of $\hat{\boldsymbol{\lambda}}_{\text{nom}} = \hat{\mathbf{n}}$ and small pitch angles, α.

2.2. Equations of Motion

The dynamics of the solar sail are expressed in the ECI reference frame through the following equation of motion:

$$\frac{d\mathbf{v}}{dt} = \mathbf{a}_{\text{total}} = \frac{\text{GM}_\oplus}{r^3}\mathbf{r} + \mathbf{a}_{\text{J}_2} + \mathbf{a}_{\text{SRP}} + \mathbf{a}_{\text{aero}} \tag{2}$$

where $\text{GM}_\oplus = 398600.4415\ \text{km}^3/\text{s}^2$ is the Earth's gravitational parameter [9], r is the magnitude of $\mathbf{r}$, i.e. the distance between sailcraft and the Earth, $\mathbf{a}_{\text{J}_2}$ is the acceleration due the Earth's gravitational J_2 spherical harmonics coefficient, $\mathbf{a}_{\text{SRP}}$ is the SRP acceleration, and $\mathbf{a}_{\text{aero}}$ is the aerodynamic acceleration. Expressions for these accelerations are given in the following sections. Note that for this first investigation into uncertainty quantification in the solar-sail near-Earth orbital dynamics, accelerations with smaller magnitude due to planetary radiation pressure, third-body effects, and higher-order Earth gravity terms are neglected.

J_2 perturbation

The J_2 acceleration, $\mathbf{a}_{\text{J}_2}$, is modelled as per Eq. 20.6 in Reference [9]:

$$\mathbf{a}_{\text{J}_2} = -\nabla\left[\frac{1}{2}\text{GM}_\oplus \text{J}_2 \frac{R_\oplus^2}{r^3}\left(3\frac{z^2}{r^2} - 1\right)\right] \tag{3}$$

where z is coordinate of the spacecraft position vector along $\hat{\mathbf{z}}_I$, and $R_\oplus$ is the reference radius of the Earth and J_2 is the Earth's J_2 gravitational coefficient, both taken from the GGM03 model [10].

Solar radiation pressure acceleration

The SRP acceleration, $\mathbf{a}_{\text{SRP}}$, is modelled through the Generalized Sail Model developed by Rios-Reyes and Scheeres [11]. This method can compute the SRP acceleration of non-ideal, non-flat solar sails at small computational costs under the following assumptions: the sail shape is fixed over time, the same side of the sail is always illuminated, and there is no self-shadowing. Being a non-ideal SRP model, this method allows to compute the SRP acceleration accounting for reflection, refraction, and re-radiation of photons. According to this model, the differential SRP force, $d\mathbf{F}_{\text{SRP}}$, produced by a differential area of sail dA is given by:

$$d\mathbf{F}_{\text{SRP}} = P\,dA\left[-\left(a_1\cos^2\alpha + a_2\cos\alpha\right)\hat{\mathbf{n}} + a_3\cos\alpha\sin\alpha\hat{\mathbf{t}}\right] \tag{4}$$

where P is the SRP at the sailcraft location, $\hat{\mathbf{n}}$ is the normal direction to this differential area, and the a_1, a_2, and a_3 coefficients are given by:

$$a_1 = 1 + \rho s \qquad a_2 = B_f(1-s)\rho + (1+\rho)\frac{\varepsilon_f B_f - \varepsilon_b B_b}{\varepsilon_f + \varepsilon_b} \qquad a_3 = 1 - \rho s \tag{5}$$

where ρ is the fraction of photons that are reflected (reflectivity); s is the fraction of reflected photons that are reflected specularily (specularity); B_f and B_b are the Lambertian coefficient describing the sail's deviation of the front (illuminated) and back (non-illuminated) sides from Lambertian surfaces, respectively; and ε_f and ε_b are the emissivity coefficients for the sail's front and back sides, respectively. If one were to integrate over the surface of the solar sail one would obtain the total acceleration exerted by the sail, independently of its shape.

Rios-Reyes and Scheeres developed an analytical formula for this acceleration, assuming that the surface can be expressed through its local normal vector at any point in the sail plane [11]:

$$\mathbf{a_{SRP}} = \frac{PA}{m}\nu\left[\mathbf{J}^2 \cdot \hat{\mathbf{r}}_\odot - 2\hat{\mathbf{r}}_\odot \cdot \mathbf{J}^3 \cdot \hat{\mathbf{r}}_\odot - \left(\mathbf{J}^1 \cdot \hat{\mathbf{r}}_\odot\right)\hat{\mathbf{r}}_\odot\right] \tag{6}$$

where m is the mass of the sailcraft, ν is the shadow factor, $\mathbf{J}^k$ are tensors of k-th order defined by the geometry and optical properties of the sail, and A is the projected area of the sail on the sail plane. When the vector $\hat{\mathbf{r}}_\odot$ is expressed in the sail-fixed reference frame presented in Section 2.1, the tensors $\mathbf{J}^k$ are independent of the position and orientation of the sail. These tensors are given by the formulas:

$$\mathbf{J}^1 = \frac{1}{A}\int_A a_3 \bar{\mathbf{n}}\, dA \qquad \mathbf{J}^2 = \frac{1}{A}\int_A a_2 \bar{\mathbf{n}} \otimes \bar{\mathbf{n}}\, dA \qquad \mathbf{J}^3 = \frac{1}{A}\int_A \rho s \bar{\mathbf{n}} \otimes \bar{\mathbf{n}} \otimes \bar{\mathbf{n}}\, dA \tag{7}$$

where $\otimes$ is the outer product (thus $\mathbf{J}^2$ is a 3×3 dyadic and $\mathbf{J}^3$ is a $3 \times 3 \times 3$ triadic), and $\bar{\mathbf{n}}$ is the local normal to the surface.

The shadow factor, ν, is used to account for the potential shadowing of the sailcraft due to the presence of the Earth and Moon. In this paper, the so called conical shadow model described in References [12] and [13] is used to obtain the value of ν, which is equal to 0 when in umbra, between 0 and 1 when in penumbra, and 1 when the sailcraft is completely illuminated. Within this model, both the umbra and penumbra regions are modelled as cones whose geometry is uniquely determined by the occulting body and the Sun's diameter and the distance between them [13].

Solar Radiation Pressure

According to McInnes, the SRP P at a distance $r_\odot$ from the Sun can be expressed as [14]:

$$P(r_\odot) = P^*(r_\odot) \cdot F(r_\odot) \tag{8}$$

where $P^*(r_\odot)$ is the radiation pressure of a point source [11, 14]:

$$P^*(r_\odot) = \frac{I_{\odot,1AU}}{c}\left(\frac{1\ AU}{r_\odot}\right)^2 \tag{9}$$

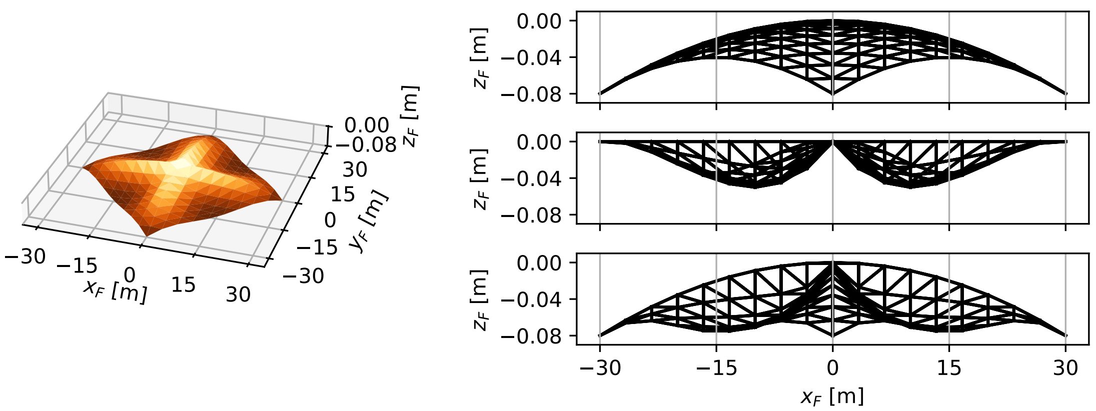

Figure 4: Deformed sail with boom length of 30 m, boom tip displacement of 0.08 m, and billow displacement of 0.05 m, as per the Solar Cruiser model of Gauvain and Tyler [6]. Isometric view on the left and side views of the tip-displaced, billowed, and tip-displaced+billowed sail on the top, center, and bottom right, respectively.

with $I_{\odot,1AU}$ the Total Solar Irradiance (TSI) at a distance of 1 astronomical unit (AU) from the Sun, c the speed of light, and $F(r_\odot)$ a correction factor accounting for the finiteness of the solar disk as seen from the sailcraft, which is assumed to be $F \approx 1$ in this work given the large distance between Sun and the Earth. Note that, while the TSI varies noisily depending on the solar activity, a constant value of 1360.88 W/m^2 is assumed in this work. This value corresponds to the average TSI over the 2004-2020 period, as obtained from the SORCE mission TIM instrument [15].

Sail shape model

Equation 7 defines the $\mathbf{J}^k$ tensors as a function of the solar sail's shape. This study assumes that the sail is deformed according to the model presented by Gauvain and Tyler for the Solar Cruiser sailcraft [6]. This shape assumes a four-quadrant sail with booms along the diagonals. These booms are assumed to deform parabolically due to the thermal loads caused by the difference in temperature between the sunlit and dark sides of the sail. Moreover, a billowing effect is also considered to account for scenarios where the deflected booms produce reduced tension on the membrane. Figure 4 displays a deformed sail with this shape, as well as side views to clearly show the effects of billowing and tip displacement, both individually and collectively.

Assuming that the four booms are deflected equally, the surface of a quadrant of the sail can be expressed as [6]:

$$\Delta z_p(r_p,\theta_p) = -\Delta z_{\text{tip}} \left(\frac{r_p}{l}\right)^2 - \Delta z_{\text{billow}} \left| \sin(2\theta_p) \sin\left(\frac{r_p}{\frac{2}{3}\left(\frac{l}{\sqrt{2}}\right)} \frac{\pi}{2} \right) \right| \tag{10}$$

where $\Delta z_p < 0$ is the displacement of point p along the $\hat{\mathbf{z}}_F$ axis of the sail-fixed frame; (r_p,θ_p) is the position in polar coordinates of point p in the plane that the sail would lie in if it were undeformed, with $\theta_p \in [0,\ 90]$ deg; $\Delta z_{\text{tip}} > 0$ is the displacement of the booms'

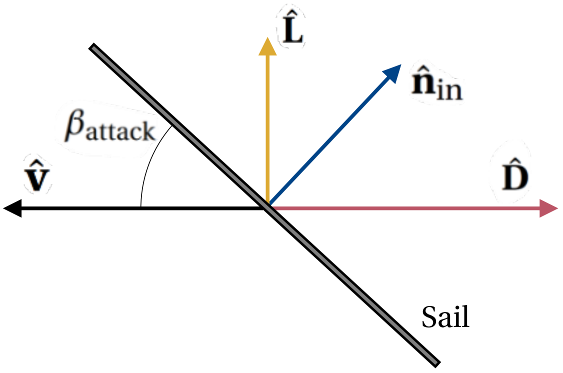

Figure 5: Direction of the aerodynamic drag, $\hat{\mathbf{D}}$, and lift, $\hat{\mathbf{L}}$, for a flat sail with angle of attack β_{attack}.

tips; $\Delta z_{\text{billow}} > 0$ is the maximum displacement due to billowing; and l is the boom length, corresponding to the sail's half-diagonal length.

Given the analytical formula for the surface of the sail, it is possible to discretize this surface into a finite number of triangular flat mesh elements, N_{faces}. From the area of each of these triangles, A_i, and their normal vectors, $\bar{\mathbf{n}}_i$, it is possible to approximate the $\mathbf{J}^k$ tensors as:

$$\mathbf{J}^1 \approx \frac{1}{A}\sum_{i}^{N_{\text{faces}}} a_3 \bar{\mathbf{n}}_i A_i \qquad \mathbf{J}^2 \approx \frac{1}{A}\sum_{i}^{N_{\text{faces}}} a_2 \bar{\mathbf{n}}_i \otimes \bar{\mathbf{n}}_i A_i \qquad \mathbf{J}^3 \approx \frac{1}{A}\sum_{i}^{N_{\text{faces}}} \rho s \bar{\mathbf{n}}_i \otimes \bar{\mathbf{n}}_i \otimes \bar{\mathbf{n}}_i A_i \tag{11}$$

In this paper, the sail is modeled with $10,000$ faces, which is computationally inexpensive and shown to produce relative errors in the SRP acceleration of less than $10^{-5}\%$.

Aerodynamic acceleration

The aerodynamic acceleration, $\mathbf{a}_{\text{aero}}$, is obtained by assuming a non-rotating flat sail in hyperthermal free-molecular flow. The non-rotating sail assumption is justified given the small angular rate of the sail compared to its orbital velocity. Moreover, given that the aerodynamic acceleration is an order of magnitude weaker than the SRP acceleration, the sail's deformation is considered negligible when computing the aerodynamic acceleration. Furthermore, the effect of wind in the upper atmosphere is neglected so that the spacecraft's velocity is equal and opposite to the impinging flow velocity.

The assumption of a hyperthermal free-molecular flow has been used often in the literature to describe the dynamics of air particles relative to a sailcraft in Earth orbit [16, 17]. It assumes the random thermal motion of the air molecules to be much slower than the velocity of the spacecraft and is valid for large Knudsen numbers, meaning that the fluid-continuum assumption of the air is no longer applicable [18].

Storch [18] provides the following formula for the aerodynamic acceleration of a flat plate under these assumptions:

$$\mathbf{a}_{\mathbf{aero}} = \frac{\rho_{\text{aero}} v^2 A}{2m}\left[\mathrm{C}_D \hat{\mathbf{D}} + \mathrm{C}_L \hat{\mathbf{L}}\right] \tag{12}$$

where ρ_{aero} is the atmospheric density, v is the spacecraft's inertial speed, $\hat{\mathbf{D}}$ and $\hat{\mathbf{L}}$ are the drag and lift directions, and C_D and C_L are the drag and lift coefficients. The drag direction, $\hat{\mathbf{D}}$, points opposite to the direction of the velocity vector, $\mathbf{v}$. The lift direction, $\hat{\mathbf{L}}$, on the other hand, is contained in the plane defined by the velocity vector and the sail's normal. Its direction is perpendicular to the velocity vector, and meets the condition $\hat{\mathbf{L}} \cdot \hat{\mathbf{n}}_{\text{in}} \geqslant 0$, where $\hat{\mathbf{n}}_{\text{in}}$ is the inner sail normal with respect to the incident flow ($\hat{\mathbf{D}} \cdot \hat{\mathbf{n}}_{\text{in}} \geqslant 0$), see Figure 5. These conditions can be expressed as:

$$\hat{\mathbf{L}} = \operatorname{sign}(\widetilde{\mathbf{L}} \cdot \hat{\mathbf{n}}_{\text{in}}) \cdot \frac{\widetilde{\mathbf{L}}}{||\widetilde{\mathbf{L}}||} \qquad \text{where} \qquad \widetilde{\mathbf{L}} = \hat{\mathbf{v}} \times (\hat{\mathbf{v}} \times \hat{\mathbf{n}}_{\text{in}}) \tag{13}$$

The drag and lift coefficients, C_D and C_L, respectively, are given by [18]:

$$\begin{aligned} C_L &= \left[\sigma_n \frac{v_w}{v} + (2 - \sigma_n - \sigma_t) \sin\beta_{\text{attack}}\right] \sin(2\beta_{\text{attack}}) \\ C_D &= 2\left[\sigma_t + \sigma_n \frac{v_w}{v} \sin\beta_{\text{attack}} + (2 - \sigma_n - \sigma_t) \sin^2\beta_{\text{attack}}\right] \sin\beta_{\text{attack}} \end{aligned} \tag{14}$$

where β_{attack} is the angle of attack of the sail, see Figure 5; σ_n and σ_t are the normal and tangential momentum accommodation coefficients; and v_w is the average normal velocity of diffusely reflected molecules which are in thermal equilibrium with the surface, and which is given by [18]:

$$v_w = \sqrt{\pi R T_w / 2} \tag{15}$$

where R is the gas constant and T_w is the mean surface temperature.

Estimating the momentum accommodation coefficients, σ_n and σ_t, is complicated; they depend on the surface material and its degree of contamination, the composition of the air (which is related to the sailcraft's altitude), the velocity of the impinging molecules, and their incidence angle [19–21]. Much like previous research on trajectory design [22–24], this work avoids this complexity by assuming these coefficients to be constant and equal to $\sigma_n = \sigma_t = 0.8$.

The surface temperature of the sail, T_w, and therefore the average normal velocity v_w, see Eq. 15, also depend on several factors: the distance from the Sun, membrane materials, sunlight incidence angle, and whether the sail is in eclipse. Kang et al. provide sail temperature minima and maxima for different orientations and sail materials according to environmental thermal analysis performed with a finite element solver [25]. Similar to the approach used for the momentum accomodation coefficients, in this paper this complexity is avoided by assuming a constant value for the ratio between the average normal velocity and the flow's velocity of $v_w / v = 0.05$, based on References [23] and [24].

Finally, the atmospheric density, ρ_{aero}, is computed using the 1976 U.S. Standard Atmosphere [26]. This exponential model is chosen due to its simplicity compared to other alternatives, such as the Marshall Engineering Thermosphere 07 (MET-07) or the Naval Research Laboratory Mass Spectrometer and Incoherent Scatter Radar Extended (NRLMSISE-0) [27, 28].

2.3. Attitude Control

Both the SRP and aerodynamic accelerations strongly depend on the attitude of the sail. Because of this, attitude control is the primary control strategy for solar-sailcraft. This paper considers ideal locally optimal steering laws for planet-centered solar sailing, as described by Macdonald and McInnes [8, 29]. Fundamental to this family of control laws is determining the unit vector, $\hat{\boldsymbol{\lambda}}_{\text{œ}}$, along which one needs to maximize the SRP acceleration in order to maximize the rate of change of the orbital element œ. Each orbital element has a different expression for $\hat{\boldsymbol{\lambda}}_{\text{œ}}$, which depends only on the instantaneous state of the spacecraft. From the reference vector expressed in the sunlight reference frame, $\hat{\boldsymbol{\lambda}}_{\text{œ}}$, it is possible to derive the locally optimal control angles as follows:

$$\tan\alpha = \frac{-3\cos\tilde{\alpha} + \sqrt{9\cos^2\tilde{\alpha} + 8\sin^2\tilde{\alpha}}}{4\sin\tilde{\alpha}} \qquad \text{where} \qquad \tilde{\alpha} = \arccos\left(\hat{\lambda}_{\text{œ},x}\right) \tag{16}$$

$$\delta = \arccos\left(\frac{\hat{\lambda}_{\text{œ},z}}{\sqrt{\hat{\lambda}^2_{\text{œ},y} + \hat{\lambda}^2_{\text{œ},z}}}\right) \tag{17}$$

From these control angles, it is possible to obtain the optimal sail normal direction in the sunlight reference frame:

$$\hat{\mathbf{n}}_{\text{optimal}} = -\begin{bmatrix} \cos\alpha \\ \sin\alpha\sin\delta \\ \sin\alpha\cos\delta \end{bmatrix} \tag{18}$$

Macdonald and McInnes [8, 29] provide expressions for the unit vector $\hat{\boldsymbol{\lambda}}_{\text{œ}}$ for various orbital parameters. These are given as a function of the instantaneous modified equinoctial elements, $\{p_{\text{eq}}, f_{\text{eq}}, g_{\text{eq}}, h_{\text{eq}}, k_{\text{eq}}, \ell_{\text{eq}}\}$, defined in Reference [30]. Of interest to this work are the expressions of $\hat{\boldsymbol{\lambda}}_{\text{œ}}$ for the semi-major axis (SMA), a, and the inclination, i. Within the RTN frame, these directions are indicated as $\boldsymbol{\lambda}_a^{\text{RTN}}$ and $\boldsymbol{\lambda}_i^{\text{RTN}}$, respectively, and their definition is given by [8, 29]:

$$\boldsymbol{\lambda}_a^{\text{RTN}} = \begin{bmatrix} f_{\text{eq}}\sin\ell_{\text{eq}} - g_{\text{eq}}\cos\ell_{\text{eq}} \\ 1 + \left(f_{\text{eq}}\cos\ell_{\text{eq}} + g_{\text{eq}}\sin\ell_{\text{eq}}\right) \\ 0 \end{bmatrix} \tag{19}$$

$$\boldsymbol{\lambda}_i^{\text{RTN}} = \begin{bmatrix} 0 \\ 0 \\ \operatorname{sign}\left(h_{\text{eq}}\cos\ell_{\text{eq}} + k_{\text{eq}}\sin\ell_{\text{eq}}\right) \end{bmatrix} \tag{20}$$

Note that $\boldsymbol{\lambda}_a^{\text{RTN}}$ and $\boldsymbol{\lambda}_i^{\text{RTN}}$ must be converted to the sunlight reference frame, see Section 2.1, before being used in Eqs. 16 and 17.

When the sail is in umbra (complete shadow), the SRP acceleration generated by the sail is zero. In this case, the locally optimal control law is ignored and the sail is oriented edgewise to the direction of velocity to minimize atmospheric drag, with its normal direction, $\hat{\mathbf{n}}$, parallel to the angular momentum direction, $\hat{\mathbf{h}}$.

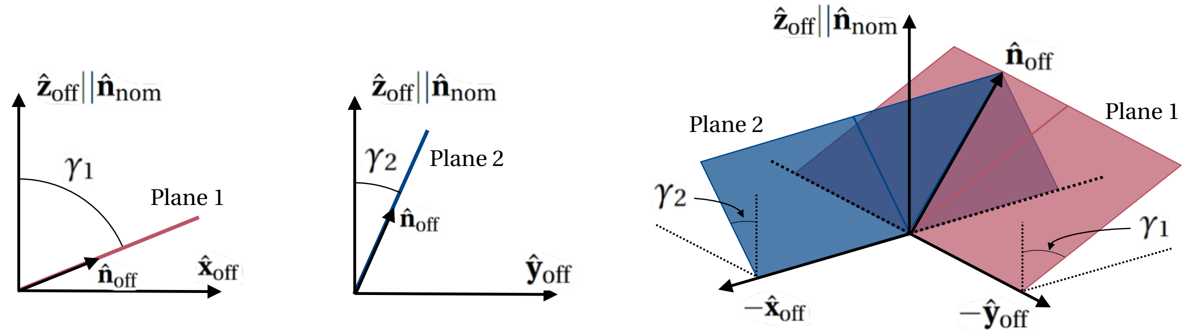

Figure 6: Sketch of how the offset normal, $\hat{\mathbf{n}}_{\mathrm{off}}$, is built from the intersection of two planes.

3. Uncertainty

This section encompasses the modelling of uncertainties and their propagation into FoMs.

3.1. Constant random value uncertainties

In this paper, the uncertainties due to unknown sail deformation parameters (Δz_{tip}, $\Delta z_{\mathrm{billow}}$) and optical coefficients (ρ, s, B_f, B_b, ε_f, ε_b) are examined. These values are assumed to be normally distributed random variables that remain constant during propagation.

The uncertainty in these input parameters is propagated into the uncertainty in some FoM through Monte Carlo (MC) simulations and the Gauss von Mises (GVM) method [31]. A comprehensive review of these methods is presented in Section 3.3.

3.2. Stochastic process uncertainties

In order to consider uncertainties in the attitude control of the sail over the mission profile, some simulations presented in this paper also consider an attitude offset with respect to the nominal attitude profile (given by the ideal locally optimal steering laws). This attitude offset is used to represent more realistic attitude profiles, such as those found in solar-sail missions with imperfect guidance, navigation and control systems [7].

Definition of the angular offset

The attitude offset is defined by means of the offset normal direction, $\hat{\mathbf{n}}_{\mathrm{off}}$, which represents the actual sail normal direction as opposed to the nominal one provided by the ideal locally optimal steering laws, $\hat{\mathbf{n}}_{\mathrm{nom}}$. To define the offset normal direction, two parameters, γ_1 and γ_2, are used, which represent angular displacements along two perpendicular directions with respect to $\hat{\mathbf{n}}_{\mathrm{nom}}$, see Figure 6. When the angular offset reference frame presented in Section 2.1 is considered with $\boldsymbol{\lambda}_{\mathrm{nom}} = \hat{\mathbf{n}}_{\mathrm{nom}} = \hat{\mathbf{z}}_{\mathrm{off}}$, these two directions correspond to the $\hat{\mathbf{x}}_{\mathrm{off}}$ and $\hat{\mathbf{y}}_{\mathrm{off}}$ axes.

Given the above, two planes can be constructed, whose normals are given by:

$$\hat{\mathbf{n}}_{\mathrm{plane},1} = \sin\gamma_1 \hat{\mathbf{z}}_{\mathrm{off}} + \cos\gamma_1 \hat{\mathbf{x}}_{\mathrm{off}} \tag{21}$$

$$\hat{\mathbf{n}}_{\mathrm{plane},2} = \sin\gamma_2 \hat{\mathbf{z}}_{\mathrm{off}} + \cos\gamma_2 \hat{\mathbf{y}}_{\mathrm{off}} \tag{22}$$

Finally, the offset normal direction, $\hat{\mathbf{n}}_{\text{off}}$, can be found from the intersection of these two planes, i.e., $\hat{\mathbf{n}}_{\text{off}} = \hat{\mathbf{n}}_{\text{plane},1} \times \hat{\mathbf{n}}_{\text{plane},2}$. Figure 6 illustrates how these planes are uniquely defined from the orthogonal offset angles, γ_1 and γ_2, in the angular offset reference frame. Note that for the case where the offset angles are zero, the offset normal coincides with the nominal normal.

Evolution of the angular offset

The angular offsets, γ_1 and γ_2, are assumed to vary randomly in time and thus are modelled as independent and identical stochastic Ornstein-Uhlenbeck processes [32]. These processes can be regarded as variations of "random walks" (Wiener) processes, in which there is a tendency to drift towards the mean value $\gamma_1 = \gamma_2 = 0$. This tendency towards zero simulates a sail attitude that constantly tries to "target" the nominal attitude. Ornstein-Uhlenbeck processes are defined by the following stochastic differential equation [32]:

$$d\gamma_i = -\theta\gamma_i dt + \sigma d\beta_{\text{Br},i}(t) \tag{23}$$

where θ and σ are the characteristic parameters of the Ornstein-Uhlenbeck process, and $\beta_{\text{Br}}(t)$ is a one-dimensional Brownian motion process. An important characteristic of these processes is that they have a bounded stationary standard deviation, given by $\sigma_{\text{st}} = \sigma/\sqrt{2\theta}$.

Because the angular offsets, γ_1 and γ_2, determine the direction of the sail normal and, therefore, the accelerations experienced by the sailcraft, Eqs. 2 and 23 are coupled. Consequently, they must be propagated in parallel through the following system of differential equations:

$$d\begin{bmatrix} \mathbf{r} \\ \mathbf{v} \\ \gamma_1 \\ \gamma_2 \end{bmatrix} = \begin{bmatrix} \mathbf{v} \\ \mathbf{a}_{\text{total}} \\ -\theta\gamma_1 \\ -\theta\gamma_2 \end{bmatrix} dt + \begin{bmatrix} \mathbf{0} & \mathbf{0} \\ \mathbf{0} & \mathbf{0} \\ \sigma_{\text{st}}\sqrt{2\theta} & 0 \\ 0 & \sigma_{\text{st}}\sqrt{2\theta} \end{bmatrix} \begin{bmatrix} d\beta_{\text{Br},1}(t) \\ d\beta_{\text{Br},2}(t) \end{bmatrix} \tag{24}$$

Due to the presence of stochastic differential equations in the above system of equations, propagation must be performed using a stochastic integrator. In this paper, the weak third-order, additive-noise stochastic integrator proposed by Debrabant is used with a time step of $h = 16$ s [33].

3.3. Uncertainty propagation

Uncertainty propagation algorithms allow one to propagate some known uncertainty about a system so as to determine the uncertainty in some FoM that is of interest. For example, when the solar-sail dynamics are considered, uncertainties in the sail's optical coefficients and attitude can be propagated to assess their impact on a sailcraft's ability to raise its orbit, as indicated by the altitude increase achieved after a given amount of time. The distribution of the input uncertainties must be known a priori, while the distribution of the output uncertainty is approximated by the results of the uncertainty propagation process. There exist many uncertainty propagation methods in the literature, but this work focuses on the use of two sample-based methods: the MC method and GVM method.

Sample-based methods are those algorithms that propagate a finite number of samples of the input uncertainty to obtain information about the output uncertainty. MC simulations are the most well-known sample-based technique for uncertainty propagation. In MC simulations, many samples are drawn randomly from the input uncertainties. σ-point methods, on the other hand, employ a small set of samples chosen ad hoc to produce as much information about the output distribution as possible. σ-point methods make assumptions about the shape of the output distribution, which can be a source of inaccuracy if the chosen shape does not correspond with the real shape of the distribution.

The GVM method is of interest to this work because, as a σ-point method, it is very computationally efficient and allows one to treat the propagation as a black-box. The MC method, on the other hand, is used whenever the GVM method is not applicable and as a validation tool for the GVM method. Despite its large computational cost, the MC method has been chosen as it can provide high-fidelity results, is very simple to implement, and is well understood in the engineering community.

Monte Carlo method

MC simulations are a well-known method for obtaining the probability density function of a random variable Y that is the result of an arbitrary map ϕ such that $Y = \phi(X)$. Its implementation is very simple: one only needs to draw a set of N_{samples} independent samples of the random variable $X^{(i)}$ and then compute the corresponding results $Y^{(i)}$ of the map ϕ. Given the law of large numbers, it is possible to prove that by increasing the number of samples, N_{samples}, the distribution of $Y^{(i)}$ will approximate the real distribution Y almost surely (as long as Y has existing and finite moments) [34].

Given a set of output samples, $\left\{\mathbf{Y}^{(1)}, \mathbf{Y}^{(2)}, \dots, \mathbf{Y}^{(i)}, \dots, \mathbf{Y}^{(N_{\text{samples}})}\right\}$ where $\mathbf{Y}^{(i)} \in \mathbb{R}^n$, then the mean vector of the distribution, $\boldsymbol{\mu}_{\mathbf{Y}} \in \mathbb{R}^n$, can be approximated as [35]:

$$\boldsymbol{\mu}_{\mathbf{Y}} \approx \frac{1}{N_{\text{samples}}} \sum_{i=1}^{N_{\text{samples}}} \mathbf{Y}^{(i)} \tag{25}$$

while the covariance matrix, $\boldsymbol{\Sigma}_{\mathbf{Y}} \in \mathbb{R}^{n\times n}$, is approximated by:

$$\boldsymbol{\Sigma}_{\mathbf{Y}} \approx \frac{1}{N_{\text{samples}} - 1} \sum_{i=1}^{N_{\text{samples}}} \left[\mathbf{Y}^{(i)} - \boldsymbol{\mu}_{\mathbf{Y}}\right] \left[\mathbf{Y}^{(i)} - \boldsymbol{\mu}_{\mathbf{Y}}\right]^T \tag{26}$$

From the covariance matrix, $\boldsymbol{\Sigma}_{\mathbf{Y}}$, one may obtain the standard deviation of the i-th element of the random variable vector $\mathbf{Y}$ by taking the square of the i-th diagonal element of $\boldsymbol{\Sigma}_{\mathbf{Y}}$, i.e., $\sigma_{\mathbf{Y}_i} = \sqrt{\boldsymbol{\Sigma}_{\mathbf{Y},(i,i)}}$.

Gauss von Mises method

The Unscented Transform method is an example of a σ-point method. This algorithm is based on a generalization of the Kalman filter for non-linear systems and it assumes that the output distribution is normally distributed [36, 37]. For perturbed two-body problems, however, this assumption is not justified, as orbital uncertainties usually lie on a non-Gaussian banana-shaped arc [35]. The GVM method, another σ-point algorithm, aims to account for this effect by carefully selecting the coordinate system with which to represent the spacecraft's state and by assuming a different output distribution shape [38].

Horwood and Poore proposed using the GVM joint distribution on an orbital element space [31]. Let $\mathbf{X} \in \mathbb{R}^n$ and $\tau \in \mathbb{S}$ be random variables[2] jointly distributed according to a GVM distribution. Then, their probability density function (pdf) is given by:

$$\mathcal{GVM}(\mathbf{X},\tau) = \mathcal{N}_{\mathbf{X}}(\boldsymbol{\mu}_{\mathcal{G}},\boldsymbol{\Sigma}_{\mathcal{G}}) \cdot \mathcal{VM}_{\tau}(\Theta_{\mathcal{G}}(\mathbf{X}),\kappa_{\mathcal{G}}) \tag{27}$$

where $\mathcal{N}_{\mathbf{X}}(\boldsymbol{\mu}_{\mathcal{G}},\boldsymbol{\Sigma}_{\mathcal{G}})$ refers to the pdf of a Gaussian distribution with mean $\boldsymbol{\mu}_{\mathcal{G}}$ and covariance matrix $\boldsymbol{\Sigma}_{\mathcal{G}}$, and $\mathcal{VM}_{\tau}(\Theta_{\mathcal{G}}(\mathbf{X}),\kappa_{\mathcal{G}})$ refers to the pdf of the von Mises distribution with parameters $\Theta_{\mathcal{G}}(\mathbf{X})$ and $\kappa_{\mathcal{G}}$. The parameter $\Theta_{\mathcal{G}}(\mathbf{X})$ is given by:

$$\Theta_{\mathcal{G}}(\mathbf{X}) = \alpha_{\mathcal{G}} + \boldsymbol{\beta}_{\mathcal{G}}^T\mathbf{z} + \frac{1}{2}\mathbf{z}^T\boldsymbol{\Gamma}_{\mathcal{G}}\mathbf{z} \qquad \text{where} \qquad \mathbf{z} = \mathbf{S}_{\mathcal{G}}^{-1}(\mathbf{X}-\boldsymbol{\mu}_{\mathcal{G}}) \qquad \text{and} \qquad \boldsymbol{\Sigma}_{\mathcal{G}} = \mathbf{S}_{\mathcal{G}}\mathbf{S}_{\mathcal{G}}^T \tag{28}$$

In Eqs. 27 and 28, $\boldsymbol{\mu}_{\mathcal{G}} \in \mathbb{R}^n$, $\boldsymbol{\Sigma}_{\mathcal{G}} \in \mathbb{R}^{n\times n}$ must be symmetric positive-definite, $\alpha_{\mathcal{G}} \in \mathbb{R}$, $\boldsymbol{\beta}_{\mathcal{G}} \in \mathbb{R}^n$, $\boldsymbol{\Gamma}_{\mathcal{G}} \in \mathbb{R}^{n\times n}$ must be symmetric, $\kappa_{\mathcal{G}} > 0$, and the matrix $\mathbf{S}_{\mathcal{G}}$ must be lower-triangular, which means that $\mathbf{S}_{\mathcal{G}}$ can be generated from the Cholesky decomposition of $\boldsymbol{\Sigma}_{\mathcal{G}}$.

The GVM distribution presents attractive properties. For example, it satisfies the periodicity property, so that pdf$(\mathbf{X},\tau)$ =pdf$(\mathbf{X},\tau+2\pi)$. This means that the τ variable can be treated as the fast-changing angular variable of an orbital element set, while the variable $\mathbf{X}$ can absorb the remaining elements. Moreover, the parameter $\boldsymbol{\Gamma}_{\mathcal{G}}$ can be tuned so that the distribution takes the "banana" shape distinctive to the (perturbed) two-body problem.

Horwood and Poore provide a formulation to apply the well known σ-point methodology to the GVM distribution. They provide formulas for the equivalent 3rd degree method, which similarly to its Gaussian counterpart, requires only $2n+3$ samples to propagate, where n is the number of uncertain parameters in the system. Higher order methods are also derivable, but they are not included in the original paper.

The GVM method can be applied as follows. One assumes a known initial distribution that is Gaussian in the Cartesian space, which can be approximated as a GVM distribution through the method given by Horwood and Poore [31]. Once this distribution is known, the appropriate σ-points and their weights are computed according to the formulas by Horwood and Poore. Each σ-point is converted from the orbital element space to the Cartesian state and then propagated through the relevant ordinary differential equations. Once propagated, these points are reconverted to the orbital element space and the final GVM distribution is recovered from the transformed σ-points by finding the optimal values of $\alpha_{\mathcal{G}}$, $\boldsymbol{\beta}_{\mathcal{G}}$, and $\boldsymbol{\Gamma}_{\mathcal{G}}$ through an optimization process. The final GVM distribution can then be converted to a Gaussian distribution in the Cartesian space, if necessary, or sampled at a very small computational cost.

---

[2] The notation $\tau \in \mathbb{S}$ is used to convey that the parameter τ is defined in the circle $\mathbb{S}$. Thus, the full state definition $(\mathbf{X},\tau) \in \mathbb{R}^n \times \mathbb{S}$ is given in a hyper-cylindrical space where τ is the angular parameter.

In practice, Horwood and Poore observe that the GVM method can extend the effective life of the Unscented Transform with almost the same computational costs (the same number of σ-points, but with a slight overhead due to the optimization problem associated with recovering the final GVM distribution). They found that the GVM technique could provide accurate depictions of the uncertainty for periods up to eight times larger than the Unscented Transform [31].

4. Analysis of constant random value uncertainties

This section covers selected results from an analysis on the effect of constant random value uncertainties on the uncertainties of two FoM uncertainties. These FoMs are the altitude increase (i.e., SMA increase) and inclination increase obtained after maneuvering using the ideal locally optimal orbit-raising and inclination-raising steering laws, respectively. Note that, given that the studied orbits are approximately circular, one should understand the altitude of the orbit simply as the SMA minus the Earth's radius.

First, in-depth studies are presented for two specific orbits: different uncertainty sources are studied independently and later coupled, and the time evolution of the uncertainty is analyzed. Three test cases are considered for this analysis. In the first two, orbits with Local Time of the Ascending Node (LTAN) either at 6AM or 12AM are considered and the sailcraft employs an orbit-raising steering law. The third test case, on the other hand, considers an initial LTAN at 12 AM and an inclination-increase steering law. All test cases consider November 1st 2023 as the simulation (mission) start date, i.e., the current estimated launch date of the ACS3 mission. For the first two cases, the FoM is the altitude gain, and for the third case the FoM is the inclination gain. After this detailed study, a parametric analysis of the influence of the orbit's initial LTAN and the mission start date on the uncertainty of the FoMs is presented.

4.1. Nominal scenarios

The test case presented in this section is inspired primarily by the ACS3 mission. Similarly to this mission, circular Sun-Synchronous orbits with the following classical orbital elements are considered:

$$\left\{a, e, i, \Omega, \omega, \bar{f}, t\right\}_0 = \{7071\ \text{km},\ 0,\ 98.16\ \text{deg},\ \Omega(\text{LTAN}, \text{M}),\ 0\ \text{deg},\ 0\ \text{deg},\ 2023/\text{M}/01\} \quad (29)$$

where multiple right ascension of the ascending node and initial times are studied. The right ascension of the ascending node, Ω, is a function of the LTAN of the orbit and the month, M, when propagation takes place, while the initial time is the first day of the selected month in 2023. LTANs at approximately 6 AM and 6 PM tend to have the shortest time (or no time) in the Earth's shadow, while LTANs at approximately 12 AM and 12 PM have the longest time in shadow.

Table 1 shows the nominal parameters that define the solar sail considered in this paper. The sail's loading parameter, σ_{load}, which is the ratio between the sail's mass to its area, and

Table 1: Nominal solar-sail parameters considered in this paper.

σ_{load} [kg/m^2]	l [m]	ρ [-]	s [-]	B_f [-]	B_b [-]	ε_f [-]	ε_b [-]	Δz_{billow} [m]	Δz_{tip} [m]
0.20266	7.0	0.91	0.89	0.79	0.67	0.025	0.27	0.0117	0.0187

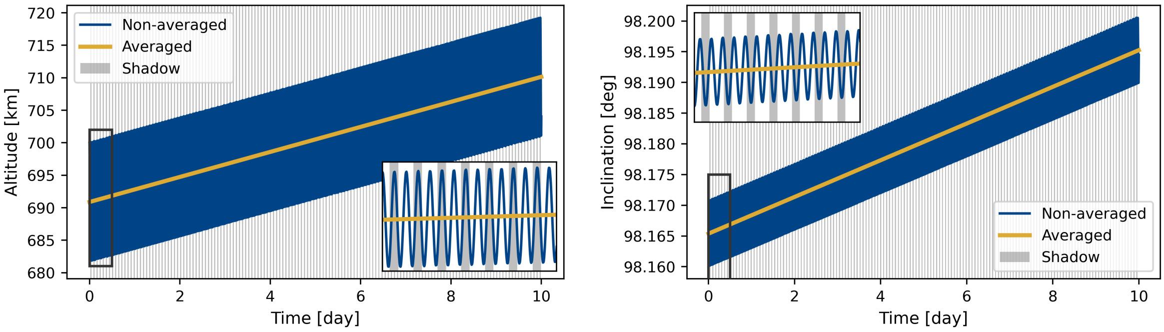

Figure 7: Nominal (uncertainty-free) increase in altitude and inclination using the orbit-raising and inclination raising steering law for 10 days, with initial LTAN at 12AM and simulation start date on November 1, 2023.

its boom length, l, are obtained from data relevant to the Advanced Composite Solar Sail (ACS3)[3]. The sail's optical coefficient data is obtained from the NEA Scout solar sail model [4]. Finally, the nominal tip displacement and billowing are taken as the nominal values for these values presented in Reference [6] but scaled by $7/30$, which is the ratio between the boom length of the sail considered in this paper and the boom length of the sail considered in Reference [6].

Figure 7 shows the altitude and inclination increase of two example nominal scenarios/orbits when employing the orbit-raising and inclination-increase steering laws, respectively, for an LTAN at 12AM and simulation start date on November 1, 2023. As one can see, the inclusion of J_2 perturbations introduces a strong oscillatory behaviour in both the altitude and inclination. Because this renders the retrieval of the effective altitude and inclination increases more challenging, in this paper an averaging procedure is performed to remove these oscillations, hence yielding a more accurate depiction of the orbital changes due to the solar sail. As can be observed in the figure, the averaged increases were found to be linear for both orbital elements. Similar linear behaviour was found for all nominal scenarios studied in this paper.

In this paper, the FoMs considered are the averaged altitude and inclination increase obtained after maneuvering through the locally optimal steering laws for some days, Δh and Δi, respectively. Because these FoM are generally randomly distributed, one may talk about the mean, $\mu_{\Delta h}$ and $\mu_{\Delta i}$, and standard deviation, $\sigma_{\Delta h}$ and $\sigma_{\Delta i}$, of their distributions. Moreover, these FoM might sometimes be scaled by the averaged nominal FoM, Δh_{nom} or Δi_{nom}, as obtained in the nominal case (without perturbations) and as presented in the "Averaged" lines in Figure 7.

Table 2 shows the sail parameter uncertainties studied in this paper. These parameters

---

[3] Data taken from communication with the ACS3 team at NASAs Langley Research Center.

Table 2: Standard deviations for the uncertain sail parameters studied in this paper. Note that $\sigma_2 = 2\sigma_1$.

	ρ [-]	s [-]	B_f [-]	B_b [-]	ε_f [-]	ε_b [-]	Δz_{billow} [m]	Δz_{tip} [m]
σ_1	0.005	0.045	0.05	0.05	0.005	0.005	0.00585	0.00935
σ_2	0.01	0.09	0.1	0.1	0.01	0.01	0.0117	0.0187

Table 3: $\sigma_{\Delta h}$ according to the MC method and relative difference for this value according to the MC and GVM methods. Different input uncertainties are considered individually for a solar sail in an orbit with 6 AM LTAN.

	σ_1		σ_2	
	$\sigma_{\Delta h,\text{MC}}$ [m]	$\frac{\sigma_{\Delta h,\text{GVM}} - \sigma_{\Delta h,\text{MC}}}{\sigma_{\Delta h,\text{MC}}}$ [%]	$\sigma_{\Delta h,\text{MC}}$ [m]	$\frac{\sigma_{\Delta h,\text{GVM}} - \sigma_{\Delta h,\text{MC}}}{\sigma_{\Delta h,\text{MC}}}$ [%]
s	583.7	2.32	991.3	3.97
ρ	182.2	1.31	372.6	-1.31
B_f	94.65	1.51	177.7	8.73
B_b	71.99	1.83	146.6	0.19
ε_f	36.57	-0.46	68.77	6.58
ε_b	3.41	-1.44	6.593	2.74
Δz_{billow}	0.1174	-100.00	0.7555	-73.67
Δz_{tip}	0.04514	-100.00	0.2996	-73.82

are considered normally distributed with standard deviation σ_1 or σ_2. The σ_1 distribution of the optical coefficients is obtained from data published for the NEA Scout solar sail [4]. On the other hand, the standard deviation of the deformation parameters is set to half of their nominal value. This causes the parameters to appear with 95% probability within zero and twice of their nominal value when drawn from the normal distribution. In their parametric study, Gauvain and Tyler [6] considered values for these parameters between zero and twice of their nominal value. Finally, a second set of standard deviations, σ_2, is considered, which is twice the values of σ_1. This is done to test the limits of the GVM and represent missions in which the sail characteristics are not so finely known as for NASA's NEA Scout and Solar Cruiser.

A fixed-step Runge-Kutta integrator of order 8 with time step 64 s is used, which was found to create integration position errors below 10 m after 10 days of maneuvers. Whenever the MC method is used, 1000 samples are employed.

4.2. Uncertainty due to uncoupled uncertainties

This section presents the uncertainty in the FoM after 1 day of maneuvers due the input uncertainties displayed in Table 1. Each source of uncertainty is studied independently, and two standard deviations are considered for each input uncertainty, σ_1 and σ_2.

Tables 3, 4 and 5 show the standard deviation of the FoM caused by each input uncertainty, as well as the relative error of the GVM method with respect to the MC method when obtaining this value. The tables provide a clear hierarchy of the most impactful input uncertainties. Independently of the LTAN and the FoM under analysis, the uncertainty in

Table 4: $\sigma_{\Delta h}$ according to the MC method and relative difference for this value according to the MC and GVM methods. Different input uncertainties are considered individually for a solar sail in an orbit with 12 AM LTAN.

	σ_1		σ_2	
	$\sigma_{\Delta h,\text{MC}}$ [m]	$\frac{\sigma_{\Delta h,\text{GVM}}-\sigma_{\Delta h,\text{MC}}}{\sigma_{\Delta h,\text{MC}}}$ [%]	$\sigma_{\Delta h,\text{MC}}$ [m]	$\frac{\sigma_{\Delta h,\text{GVM}}-\sigma_{\Delta h,\text{MC}}}{\sigma_{\Delta h,\text{MC}}}$ [%]
s	267.3	1.39	436.9	6.89
ρ	108.2	1.17	221.3	-1.61
B_f	62.23	4.09	121.4	5.61
B_b	50.2	-1.59	96.24	2.69
ε_f	24.1	1.09	48.83	-0.02
ε_b	2.237	1.70	4.668	-2.15
Δz_{billow}	0.08068	-100.00	0.4225	-72.00
Δz_{tip}	0.02729	-100.00	0.1937	-75.91

Table 5: $\sigma_{\Delta i}$ according to the MC method and relative difference for this value according to the MC and GVM methods. Different input uncertainties are considered individually for a solar sail in an orbit with 12 AM LTAN.

	σ_1		σ_2	
	$\sigma_{\Delta i,\text{MC}}$ [milli deg]	$\frac{\sigma_{\Delta i,\text{GVM}}-\sigma_{\Delta i,\text{MC}}}{\sigma_{\Delta i,\text{MC}}}$ [%]	$\sigma_{\Delta h,\text{MC}}$ [milli deg]	$\frac{\sigma_{\Delta i,\text{GVM}}-\sigma_{\Delta i,\text{MC}}}{\sigma_{\Delta i,\text{MC}}}$ [%]
s	0.8169	10.03	1.501	3.53
ρ	0.2607	-2.81	0.5185	-2.51
B_f	0.1304	-3.98	0.2363	6.13
B_b	0.09694	-0.95	0.1955	-1.67
ε_f	0.04677	1.94	0.09428	0.58
ε_b	0.004428	-1.22	0.008791	-0.15
Δz_{billow}	0.0001672	-100.00	0.001045	-73.60
Δz_{tip}	0.00006113	-100.00	0.0004102	-73.61

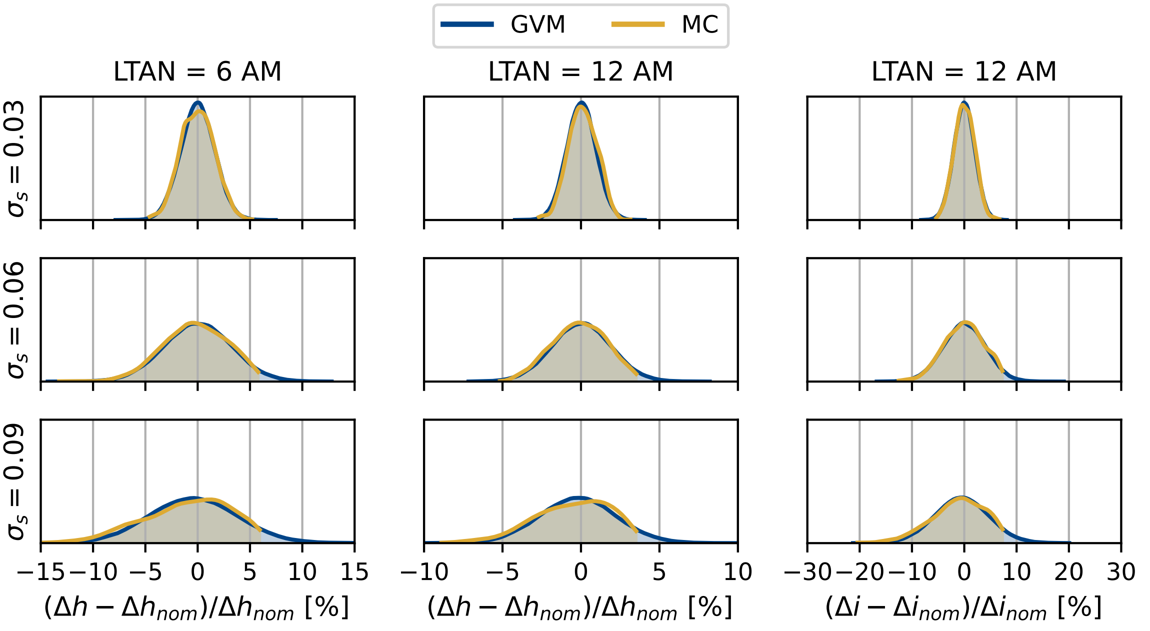

Figure 8: Distribution of the FoMs after 10 days of maneuvers according to MC and GVM simulations. Results are presented for three different specularity standard deviations, σ_s, and for different LTANs and control laws.

specularity has the strongest effect, followed by the uncertainty in reflectivity. On the other hand, the uncertainty due to the emissivity coefficients and the deformation parameters is considerably smaller. The impact of the deformation is almost negligible, a finding that coincides with previous research suggesting that small deviations from flatness in solar sails barely impact the acceleration produced by them [39].

Tables 3, 4 and 5 additionally reflect that the GVM method provides relatively accurate estimates of the MC method's standard deviations (taken as ground truth) independently of the input uncertainty, its magnitude, the orbit's initial LTAN, or the FoM under study, although requiring a computational cost orders of magnitude smaller than MC simulations. The most notable exception to this statement appears for the deformation parameters, Δz_{billow} and Δz_{tip}, whose influence is so small that the GVM method fails to capture any influence at all.

4.3. Detailed analysis of the uncertainty in specularity

The previous section provided a first order characterization of the impact of every input uncertainty on the FoMs. This section, in turn, provides a deeper exploration of the FoM distributions due to a single uncertain input, the specularity, which proved to be the most impactful system uncertainty.

Figure 8 shows the distribution of the FoMs after 10 days of maneuvers for the sail parameters given in Table 1 and three specularity standard deviations, $\sigma_s = \{0.3, 0.6, 0.9\}$. In order to display the results more intuitively, the FoMs are provided in terms of relative difference with respect to the FoMs of the nominal cases. By doing so, the plots of Figure 8

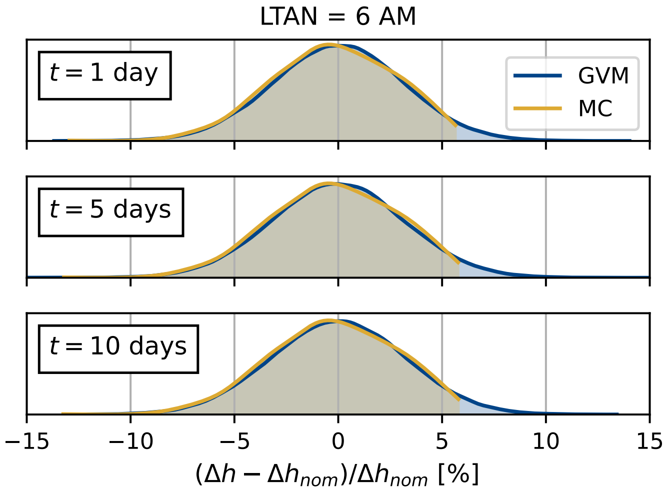

Figure 9: Distribution of the altitude increase due to a specularity standard deviation of $\sigma_s = 0.06$ for an initial LTAN at 6 AM.

clearly show how much the uncertainty in specularity causes results that under-perform or over-perform compared to the nominal cases. If a larger specularity is considered, for instance, then a more performant sail is obtained and thus above-nominal gains are obtained. The opposite is true for smaller-than-nominal specularities.

The plots of Figure 8 show that the FoM distributions approximately follows a normal distribution, independently of the LTAN or the FoM considered. Moreover, the GVM method is capable of accurately capturing the same behaviour as the more computationally expensive MC simulations, as the GVM and MC distributions assume similar mean and standard deviation values independently of the standard deviation of the specularity. The main discrepancy between the MC and GVM distributions take place for positive relative FoM gains; the truncation behaviour that the MC method exhibits is not captured by the GVM method. This is likely because, when the MC method is used, random samples of the specularity coefficient are drawn. Whenever these samples have non-physical values, i.e., $s > 1$, then the sample is re-drawn, which causes the effective distribution of specularity resemble a truncated normal distribution. This truncation permeates to the FoM distribution. However, this behaviour is missed by the GVM method, as all GVM samples (σ-points) are all within physical limits, and thus the GVM method has no knowledge of the truncation.

To better examine how the FoMs vary in time, Figure 9 shows the time evolution of the altitude distribution particularly for the case with $\sigma_s = 0.06$ and LTAN at 6AM. The figure shows how the altitude gain distribution remains normal at different times along the propagation (1, 5, and 10 days from the simulation start), with the results from the GVM method once again closely agreeing with the results from MC simulations. Interestingly, the spread of the distributions remains essentially the same for the three times shown in the figure. This suggests that the standard deviation of the altitude gain, $\sigma_{\Delta h}$, grows at the same rate as the nominal value, Δh_{nom}, and thus their ratio, $\sigma_{\Delta h}/\Delta h_{\text{nom}}$, remains constant

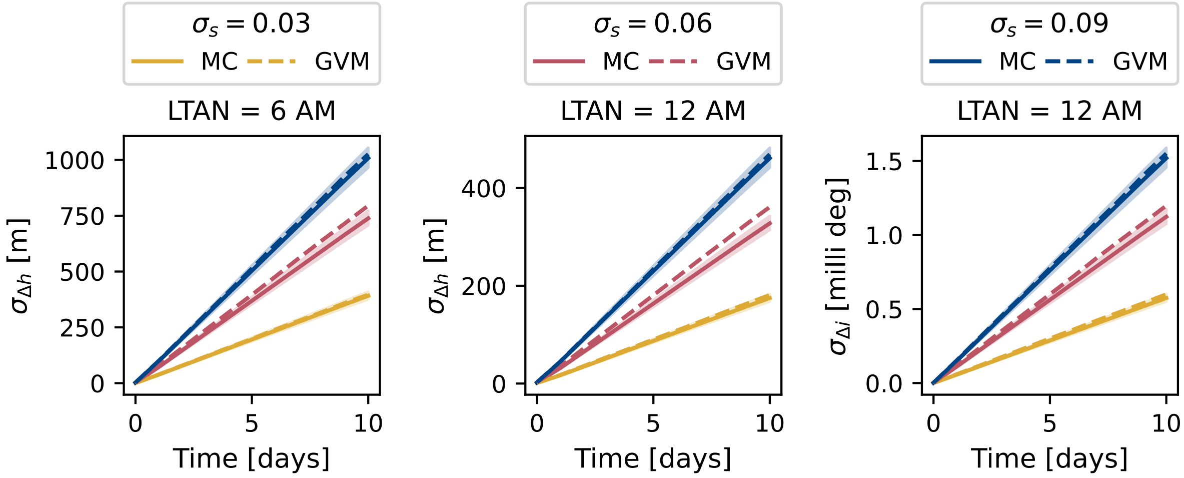

Figure 10: Evolution in time of $\sigma_{\Delta h}$ and $\sigma_{\Delta i}$ for different values of σ_s. The shaded areas represent the 95% confidence intervals of the MC results.

in time. Because this nominal value, Δh_{nom}, was found to grow linearly in time, see Section 4.1, one could expect $\sigma_{\Delta h}$ to also grow linearly. The left plot of Figure 10 confirms this hypothesis, meaning that, for example, if the standard deviation after 1 day of maneuvers is 100 m, then one could expect a standard deviation of 1 km after 10 days of maneuvers. As shown in the figure, the slope of these trends is driven by the standard deviation of the input uncertainty, the specularity. Larger input uncertainties lead to faster growing altitude uncertainties. The center and right plots of this figure additionally show that the standard deviation of the distribution of the FoM grows linearly independently of the LTAN or the orbital element studied. Note, however, that the LTAN does seem to affect the rate of increase of the standard deviation, as one can observe by comparing the left and center plots of the figure.

4.4. Uncertainty due to coupled uncertainties

Sections 4.2 and 4.3 dealt with the effects of individual input uncertainties on the uncertainty of the altitude or inclination increase. In contrast, this section discusses the effects of multiple input uncertainties acting simultaneously on these FoMs.

Figure 11 shows the distributions of the FoMs after 10 days of propagation for different sets of input uncertainties and LTANs, using the MC and GVM methods. The three sets of uncertainties considered are (from top to bottom): all uncertainties shown in Table 1, uncertainty only in specularity and reflectivity, and uncertainty only in specularity. All input uncertainties are normally distributed with standard deviations given by the row σ_1 of Table 1. As observed in the figure, the distribution obtained for “specularity and reflectivity” largely resembles the distribution when considering all uncertainties. This indicates that the specularity and reflectivity are very clearly dominant, with other uncertainties being essentially negligible. This is in-line with previous research on sail optical coefficient uncertainty, which found that specularity and reflectivity are the most significant uncertain

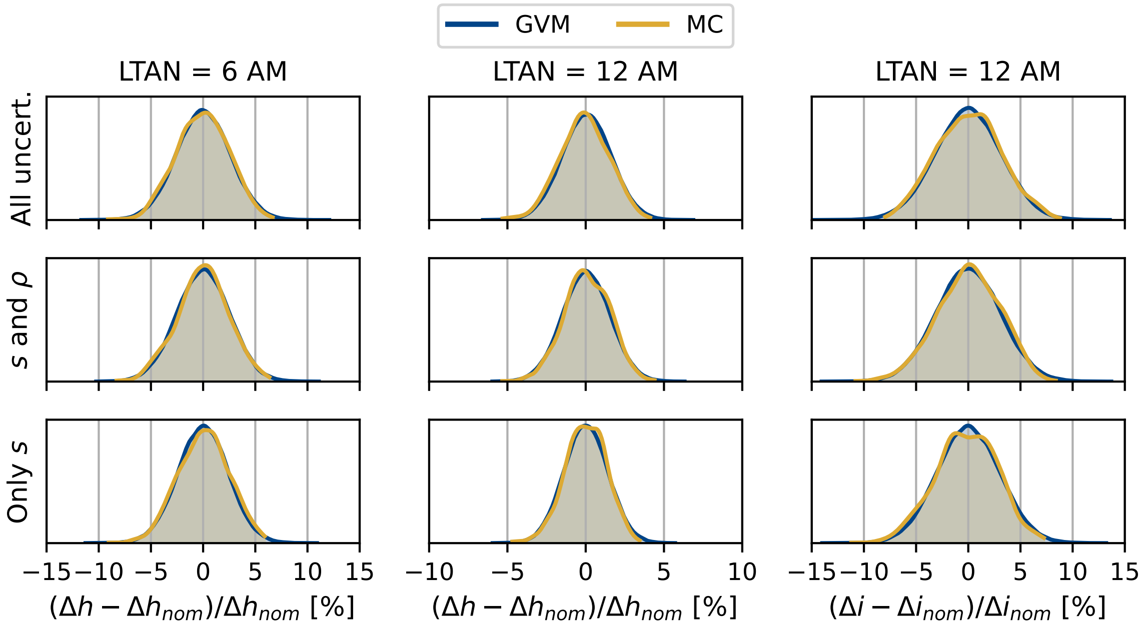

Figure 11: Distribution of the altitude and inclination increase after 10 days of maneuvers according to GVM and MC simulations for solar sails at different LTANs. Results are presented for different sets of input uncertainties.

optical coefficients when considering heliocentric trajectories [1]. These results demonstrate that analysis effort might be saved if the most dominant input uncertainties (or, alternatively, the negligible ones) are identified early on. Moreover, once again, the results from the GVM method seem to agree with those of the MC simulations.

It is important to highlight that these results indicate a 7.5% 3-σ uncertainty in altitude gain or a 9% 3-σ uncertainty in inclination gain due to the optical coefficient uncertainties found for the NEA Scout solar-sail model. For instance, if the nominal altitude increase was 10 km, this would translate to a 3-σ uncertainty of 750 m in the altitude increase. Such uncertainty could potentially have significant and detrimental effects on mission performance.

4.5. Effect of LTAN and mission date

Previous sections have presented results related to the distribution of the FoMs for solar sails in two orbits: one in a 6AM-LTAN orbit, and the other in a 12AM-LTAN orbit, and both during November 2023. This section aims to study the effect of considering many different orbit LTANs and simulation start times over the year on the distribution of the FoMs. In particular, the normalized standard deviation of these distributions, $\sigma_{\Delta h}/\Delta h_{\text{nom}}$ and $\sigma_{\Delta i}/\Delta i_{\text{nom}}$, is analyzed, as it was shown in Section 4.4 to remain constant in time. Nevertheless, all results presented in this section are obtained for sail orbits after 10 days of maneuvers. Moreover, all uncertainties shown in Table 2 are considered, with standard deviation as shown in the σ_1 row of the table.

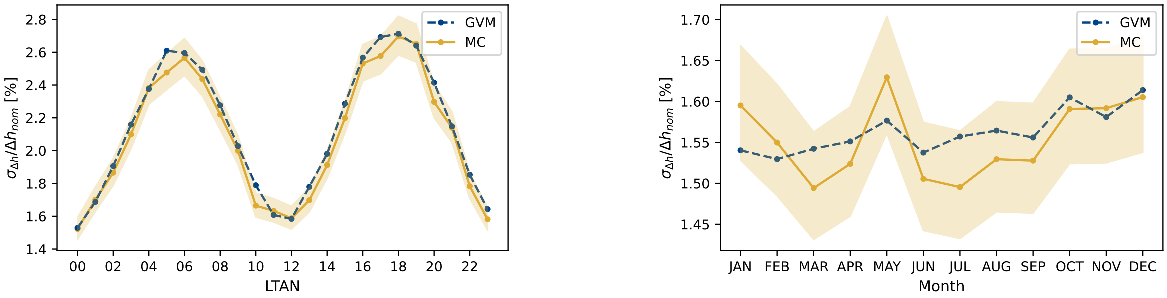

Figure 12: Normalized standard deviation of the altitude gain. Results of the left plot obtained for a simulation start date on November 1, 2023. Results of the right plot obtained for a 12 AM LTAN. The shaded regions represent the 95% confidence interval of the MC results.

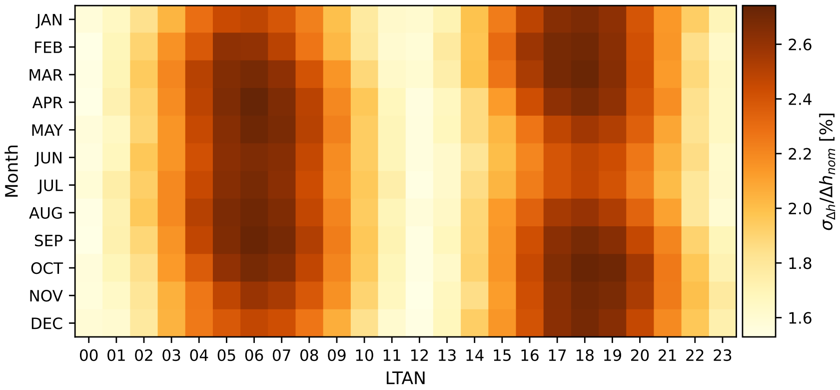

Figure 13: Normalized standard deviation of the altitude gain obtained for different LTANs and months of propagation.

Figure 12 displays the effect of different initial LTANs and simulation times on the standard deviation of the altitude increase, $\sigma_{\Delta h}/\Delta h_{\text{nom}}$. As one can see on the left plot, the largest standard deviations are found for orbits with LTANs at approximately 6 AM and 6 PM, which correspond to orbits that spend the shortest periods of time in shadow. These orbits also correspond to the largest nominal increase in altitude, Δh_{nom}. In contrast, the right plot of this figure shows no strong correlation between the month during which propagation happens and the normalized standard deviation. Both the standard deviation, $\sigma_{\Delta h}$, and the the nominal increase, Δh_{nom}, are largest near the Earth's perihelion, in January. However, because they seem to grow at a similar same rate, the obtained normalized standard deviation, $\sigma_{\Delta h}/\Delta h_{\text{nom}}$, remains approximately constant throughout the year.

Finally, it is worth noting that the results found through the GVM method generally remain within the confidence interval of the MC results. This indicates that the GVM method can provide accurate estimates of the FoM distribution independently of the LTAN or month of propagation.

Figure 13 shows the joint influence of the orbit's initial LTAN and the month of propagation on the normalized standard deviation of the altitude increase. These results were produced through the GVM method for the sake of computational efficiency. As one can

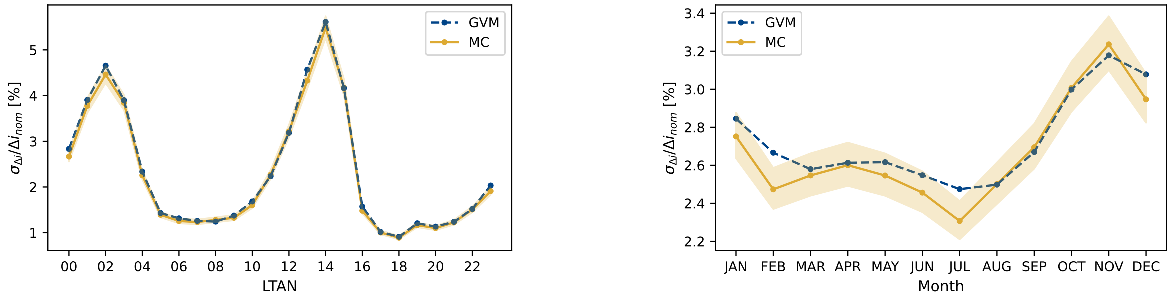

Figure 14: Normalized standard deviation of the inclination gain. Results of the left plot obtained for a simulation start date on November 1, 2023. Results of the right plot obtained for a 12 AM LTAN. The shaded regions represent the 95% confidence interval of the MC results.

see, the largest normalized standard deviations take place for LTANs close to 6 AM and 6 PM. However, there is a noticeable interaction with the month. For instance, the normalized standard deviation is smaller for January or December for a 6 AM LTAN than for April or September at the same LTAN. Also, it should be noted that symmetry is found with respect to the July's horizontal line. Given that the Earth's orbit aphelion occurs in the beginning of July, this suggests that this symmetry is caused by the symmetry in the Earth's orbit around the Sun. In general, one can say that the standard deviation of the altitude increase is bounded between 1.5% and 2.7% of the nominal altitude increase. Thus, the worst-case 3-σ uncertainty for the altitude gain was found to be 8.1%.

Figure 14 shows the influence of the initial LTANs and simulation times on the normalized standard deviation of the inclination gain, $\sigma_{\Delta i}/\Delta i_{\text{nom}}$. The left plot reveals that, interestingly, the largest normalized standard deviations appear for the orbits with the smallest nominal inclination gain, Δi_{nom}, which are found for LTANs approximately at 2 AM and 2 PM. This goes in contrast with the results found for the normalized standard deviation of the altitude gain, $\sigma_{\Delta h}/\Delta h_{\text{nom}}$, which was maximum when the nominal altitude gain was also maximum. These results prove advantageous for mission design, as orbit LTANs that feature the largest nominal inclination change also have the lowest (relative) inclination uncertainty. The right plot of Figure 14 shows how the mission date impacts the inclination gain distribution. While the impact of this factor is smaller than the LTAN's, there is still some noticeable influence.

Figure 15 shows the joint influence of the orbit's initial LTAN and the mission date. Similarly to the results presented in Figure 13, these results were generated through the GVM method. Two narrow bands, at approximately 2 AM and 2 PM LTAN, feature the largest normalized standard deviations. Within these bands, the mission date has a significant impact: for an orbit with LTAN at 3 PM, the normalized standard deviation is over 5% during October but only 3% in July. These results display the same symmetry across the July horizontal line as those shown in Figure 13. One should also note that the normalized standard deviation of the inclination has a larger range of possible values than the normalized standard deviation of the altitude: between 0.9% and 5.5%. Thus, the worst-case scenario for

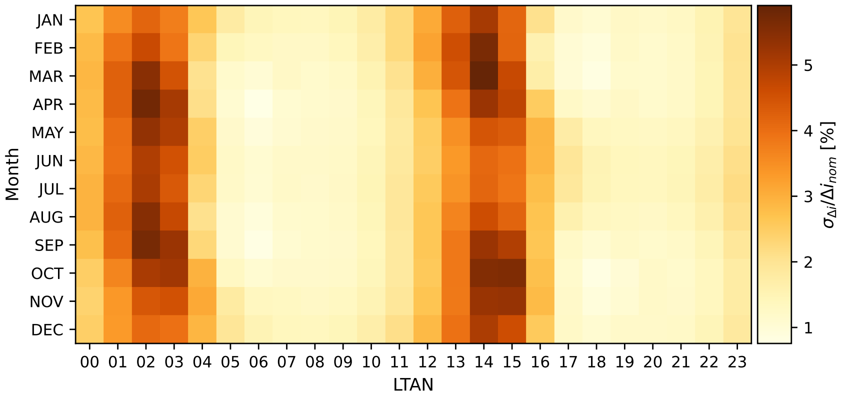

Figure 15: Normalized standard deviation of the inclination gain obtained for different LTANs and months of propagation. Results obtained through the GVM method.

the inclination increase presents a 3-σ uncertainty in inclination gain of 16.5%.

5. Analysis of stochastic process uncertainties

Previous sections dealt with constant random value uncertainties, where certain system parameters, such as the reflectivity or the billowing of the sail, were random but fixed during propagation. In contrast, this section discusses results for the uncertainty caused by considering a randomly evolving offset on the nominal attitude profile, as described in Section 3.2. The same test case as presented in Section 4.1 is used.

5.1. Evolution in time of the figure of merit distribution

This section presents the distribution of the FoMs due to attitude uncertainty and how it evolves in time for selected orbit LTANs, for four sets of Ornstein-Uhlenbeck parameters, and a simulation start date on November 1, 2023. Further study into the effect of the Ornstein-Uhlenbeck parameters is shown in Section 5.2, while the impact of the orbit LTAN and mission date is discussed in Section 5.3.

Figure 16 shows how different values of the Ornstein-Uhlenbeck parameters, θ and σ_{st}, affect the evolution of the distribution of the FoMs in time. Unlike previous results, the FoM distribution generally remains below the nominal FoM, as the nominal solution is obtained with a near-optimal steering law and any offset from this attitude profile is expected to worsen the performance of the trajectory. This makes the distribution heavily skewed towards negative values, see Figure 16. Note that, unlike for previous result shown in this paper, the standard deviation seems to differ between times, even when normalized by the nominal increase in FoM. The mean also behaves differently than in previous results; in this case, it does not coincide with the nominal increase in FoM, but it is smaller.

Figure 17 shows the evolution in time of the normalized relative mean, $\mu_{\Delta h}$ or $\mu_{\Delta i}$, and normalized standard deviation, $\sigma_{\Delta h}$ or $\sigma_{\Delta i}$, of the distributions. Studying the distributions' means holds significance due to its deviation from the nominal values, Δh_{nom} or Δi_{nom}, as illustrated in Figure 16. As seen in the top three plots, the normalized mean remains ap-

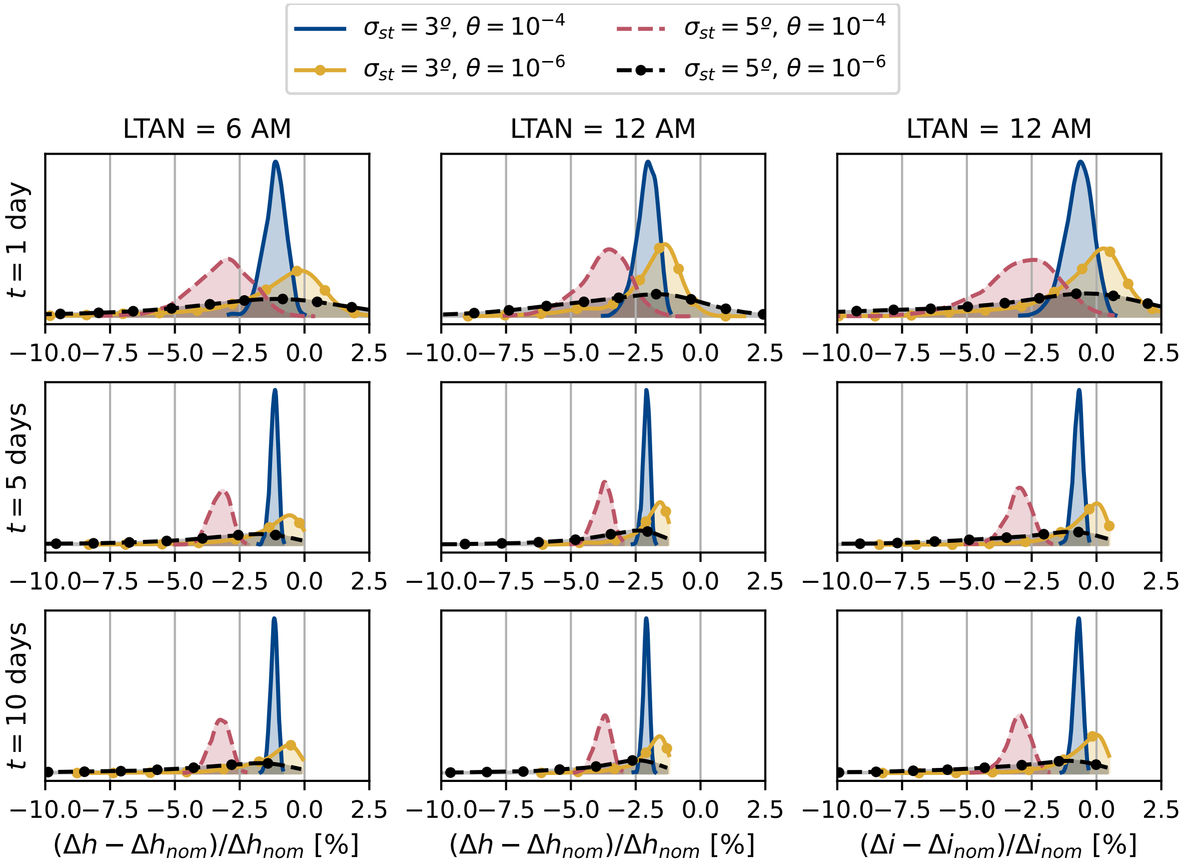

Figure 16: Distribution of the FoM increase after 1, 5, and 10 days of maneuvers for different Ornstein-Uhlenbeck parameters, θ and σ_{st}.

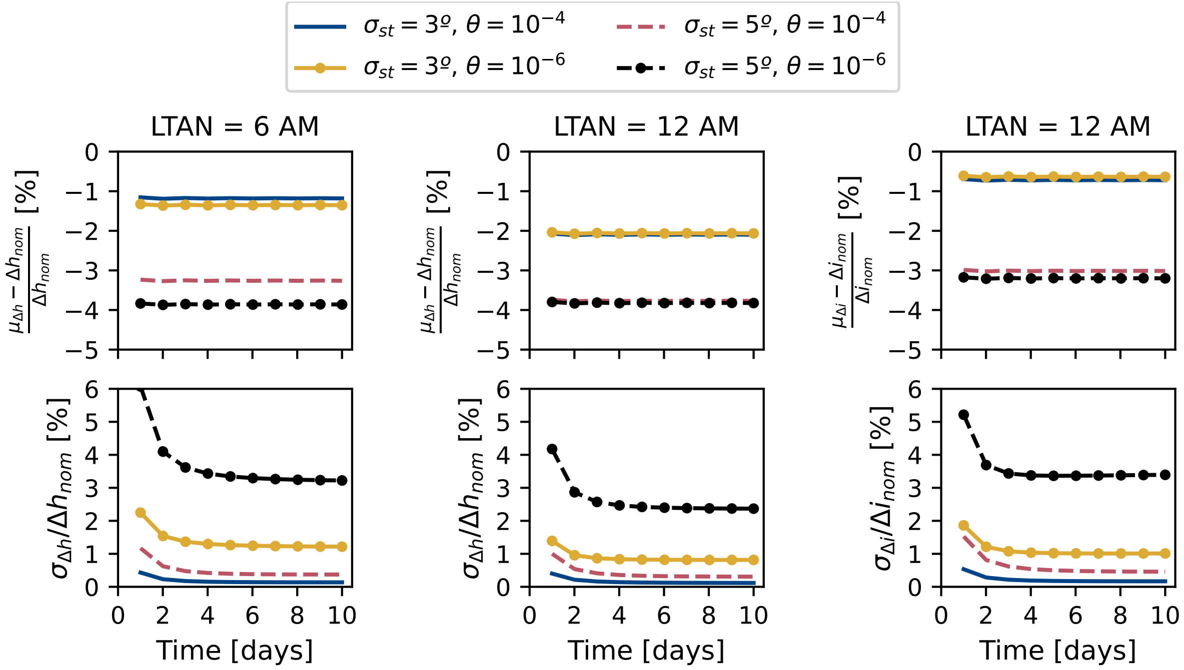

Figure 17: Time evolution of the normalized relative mean and normalized standard deviation of the distribution of the FoM for different Ornstein-Uhlenbeck parameters θ and σ_{st}.

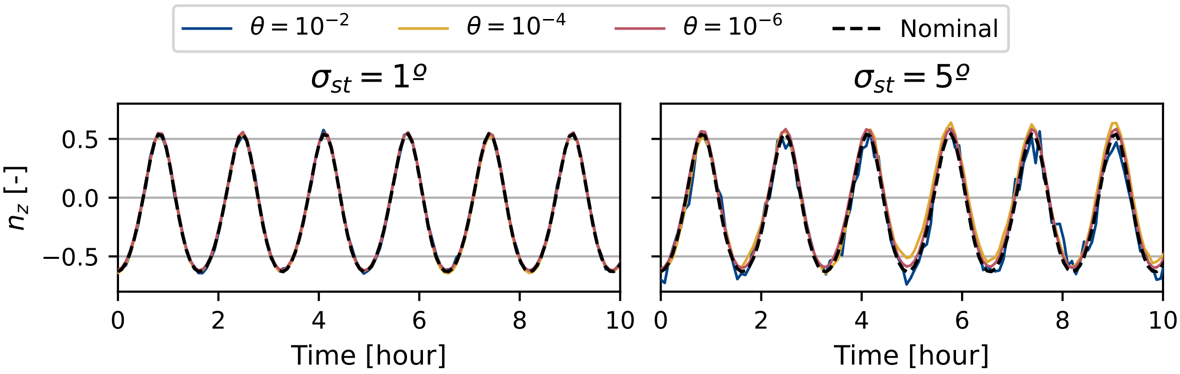

Figure 18: Evolution of the sail's attitude for different values of σ_{st} and θ. The "Nominal" line indicates the direction without random offset.

proximately constant in time, it is always below the nominal performance ($\mu_{\Delta h} < \Delta h_{\mathrm{nom}}$; $\mu_{\Delta i} < \Delta i_{\mathrm{nom}}$), and it seems to strongly depend on the σ_{st} parameter and less on the θ parameter. The normalized standard deviation, on the other hand, seems to be largest at the start of the mission, and it goes down and stabilizes as time passes. Moreover, it appears to be impacted by both the σ_{st} and θ parameters.

5.2. Effect of the Ornstein-Uhlenbeck parameters

The previous section provided some intuition on the effect of the Ornstein-Uhlenbeck parameters, σ_{st} and θ, on the distribution of the FoM increase. This section extends this understanding by studying the behaviour of both the mean, $\mu_{\Delta h}$ or $\mu_{\Delta i}$, and standard deviation, $\sigma_{\Delta h}$ or $\sigma_{\Delta i}$, as a function of the Ornstein-Uhlenbeck parameters.

Figure 18 shows the impact of the Ornstein-Uhlenbeck parameters θ and σ_{st} on the z component of the sail normal direction in the ECI reference frame when using the orbit-raising steering law for the nominal direction. This explanatory figure illustrates the evolution of the sail normal direction for six different combinations of the Ornstein-Uhlenbeck parameters during a 10-hour time window. By comparing these examples with the nominal evolution for this parameter, one can better understand the influence of θ and σ_{st} on the sail's behavior. The effect of the stationary standard deviation σ_{st} is relatively easy to understand: larger values of this parameter mean that the offset direction will generally be further away from the reference direction. The θ parameter, on the other hand, influences how rapidly the offset changes. As seen for the lines corresponding to $\theta = 10^{-2}$, the behaviour is clearly "noisy", with the offset rapidly moving above and below the reference. In constrast, for $\theta = 10^{-6}$, the offset evolves so slowly that it appears almost constant during the 10-hour window plotted in Figure 18. The line for $\theta = 10^{-4}$ represents a middle point: it is not as "noisy", but one can see it move with respect to the reference.

Figure 19 reveals the strong relationship between the stationary standard deviation σ_{st} and the mean gain in altitude, $\mu_{\Delta h}$, or inclination, $\mu_{\Delta i}$. In contrast, the parameter θ seems to have a less significant effect on this metric. As such, one concludes that mean perfor-

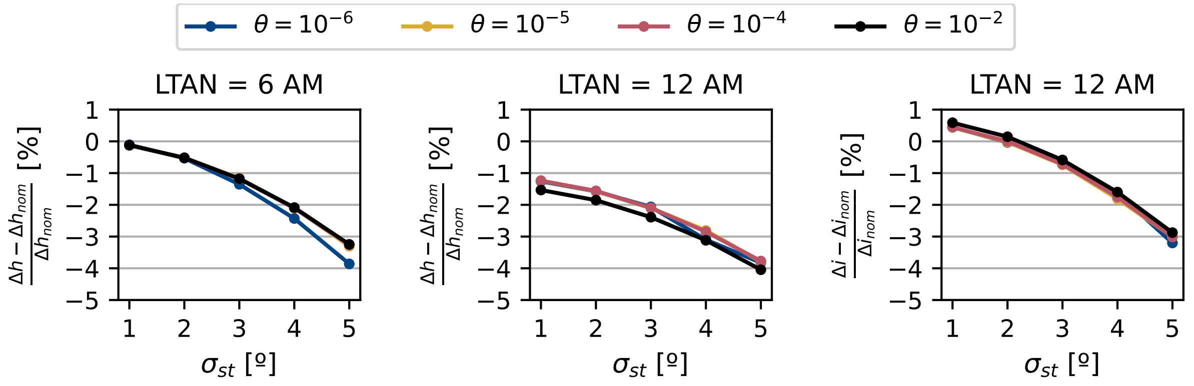

Figure 19: Mean FoM increase after 10 days of maneuvers as a function of the Ornstein-Uhlenbeck parameter σ_{st} for different values of θ.

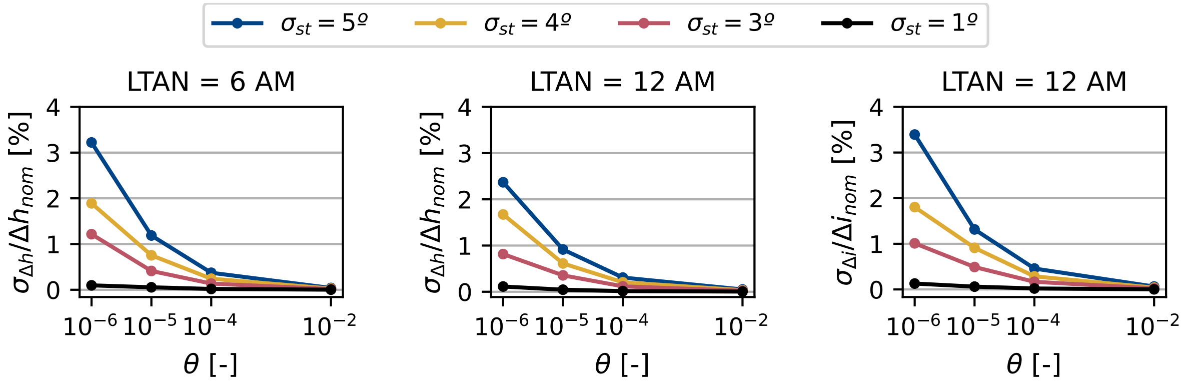

Figure 20: Normalized standard deviation of the FoM increase after 10 days of maneuvers as a function of the Ornstein-Uhlenbeck parameter θ for different values of σ_{st}.

mance loss due to uncertain attitude is mainly driven by the stationary standard deviation of the attitude with respect to the optimal control profile.

On the other hand, Figure 20 shows that both parameters θ and σ_{st} affect the spread of the altitude, $\sigma_{\Delta h}$, or inclination, $\sigma_{\Delta i}$, gain distributions. Perhaps unsurprisingly, larger values of the standard deviation of the attitude uncertainty σ_{st} lead to larger values of the standard deviation of the FoMs. In contrast, when considering smaller values of θ, there is a notable increase in the normalized standard deviation of the FoM gain. These smaller values of θ correspond to attitude offsets that evolve at a significantly slower pace, eventually reaching a point where they remain relatively constant over long periods of time. Consequently, the attitude profiles across different propagations exhibit substantial dissimilarities, resulting in a larger standard deviation in the FoM gain. Conversely, larger values of θ yield rapidly changing attitude offsets, which, on the long run, end up counteracting each other. As a result, individual propagations exhibit comparable attitude profiles, leading to a reduced standard deviation of the FoM increase.

Together, Figures 19 and 20 paint a positive picture for mission designers in terms of the effect of perturbed attitude profiles. As long as the stationary standard deviation of the

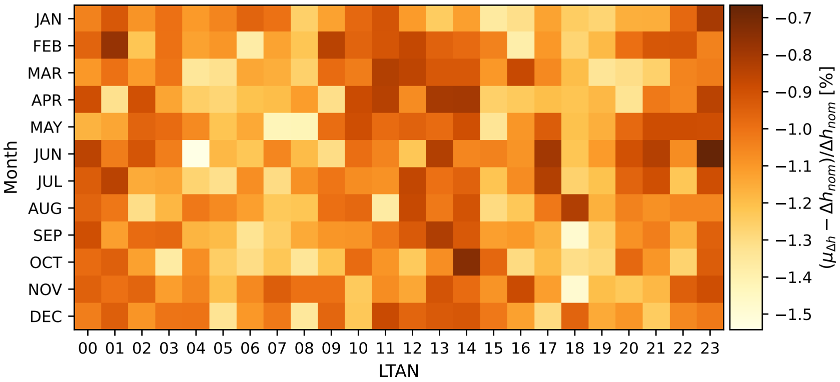

Figure 21: Normalized relative mean of the altitude gain after 10 days of maneuvers obtained for different LTANs and months of propagation.

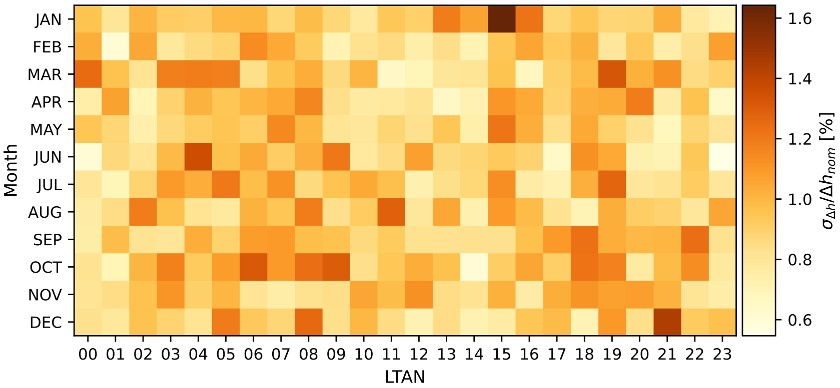

Figure 22: Normalized standard deviation of the altitude gain after 10 days of maneuvers obtained for different LTANs and months of propagation.

attitude error, σ_{st}, is kept relatively low, between 1 and 2 degrees, the mean performance loss is expected to remain quite low, at most at 2%. The uncertainty remains even lower, with a standard deviation of at most 1% of the magnitude of the nominal performance.

5.3. Effect of LTAN and mission date

Previous results for the impact of the attitude offset were shown for a mission starting on November 1, 2023 and two initial orbit's LTANs: 6 AM and 12 AM. In contrast, this section studies the influence of different mission dates and sail's orbit LTANs while assuming the following arbitrary Ornstein-Uhlenbeck parameters: $\sigma_{\mathrm{st}} = 3$ deg and $\theta = 10^{-6}$.

Figures 21 and 22 show the dependency of the normalized relative mean and normalized standard deviation of the altitude increase, respectively, on the mission date and LTAN. Neither of these figures reveal a strong correlation between the FoM and the mission date or LTAN. In general, one can say that the mean altitude increase is between 0.7% and 1.5% lower than the nominal altitude increase, while the standard deviation of this metric is bounded between 0.5% and 1.7% of the nominal increase.

Figures 23 and 24, on the other hand, show the join effect of the mission date and LTAN on the normalized relative mean and normalized standard deviation of the inclination in-

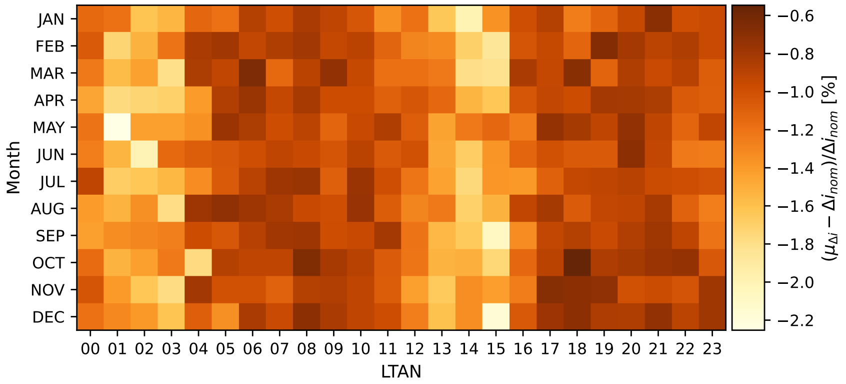

Figure 23: Normalized relative mean of the inclination gain after 10 days of maneuvers obtained for different LTANs and months of propagation.

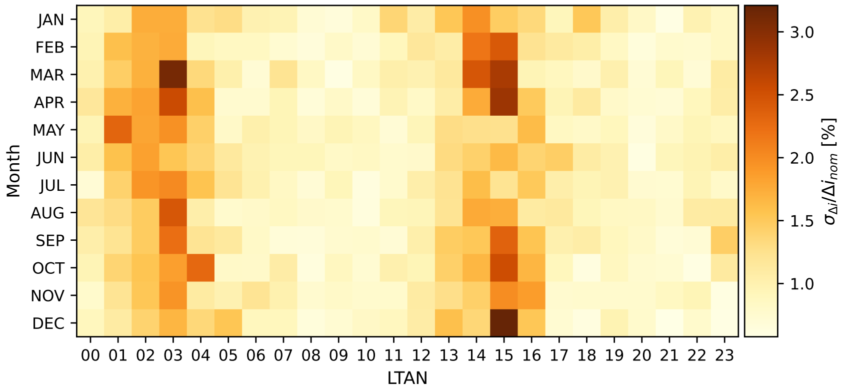

Figure 24: Normalized standard deviation of the inclination gain after 10 days of maneuvers obtained for different LTANs and months of propagation.

crease. Figure 23 reveals that the largest mean performance loss and standard deviation appear for LTANs approximately at 2 AM and 2 PM. These LTANs coincide with the orbits that show the lowest nominal inclination increase, which is advantageous to mission design, as smaller performance losses and uncertainties are found for the orbits with largest nominal inclination increase. Generally, one finds the normalized mean performance loss to be between 0.6% and 2.2%, while the normalized standard deviation remains between 0.5% and 3.25%.

6. Conclusion

In conclusion, this paper sheds light on the significance of uncertainty in solar-sail mission design. The findings highlight the substantial impact of uncertainty in the sail's optical coefficients on mission performance when attempting to increase the orbital altitude or inclination. When considering the optical coefficients' uncertainties published of NEA Scout solar-sail model, a worst-case 3-σ altitude gain uncertainty of 8.1% was observed. Similarly, a worst-case 16.5% 3-σ uncertainty on the inclination gain was found. The largest uncertainties in altitude gain appeared for orbits with Local Time of the Ascending Node (LTAN) at approximately 6 AM or 6 PM. For sailcraft performing inclination-increasing maneuvers, the largest uncertainties in mission performance appeared for orbits with LTANs at approximately 2 AM and 2 PM. The uncertainty in specularity played the largest role in performance uncertainty out of the analyzed optical coefficients, followed by uncertainty in reflectivity. The sail's structural deformation was found to have minimal influence on the performance uncertainty.

The study on attitude uncertainty revealed not only its impact on mission performance uncertainty, but also highlighted that assuming an ideal control profile most often leads to overestimated performance expectations. By incorporating the Ornstein-Uhlenbeck process with tunable parameters, different types of error in attitude profiles were modelled, resulting in distributions of the mission performance metrics with different means and spreads. The mission performance uncertainty due to attitude uncertainty was found to depend weakly on the initial LTAN and mission date, and strongly on the Ornstein-Uhlenbeck parameters, which define the nature of the attitude error. For the analyzed Ornstein-Uhlenbeck parameters, a worst-case mean performance loss of 1.5% was found for the altitude gain and of 2.2% for the inclination change. Furthermore, a worst-case 5.1% and 9.75% 3-σ uncertainty was observed for the altitude and inclination gains, respectively.

The Gauss von Mises method proved to be an efficient and effective uncertainty propagation technique, demonstrating its accuracy at a considerably smaller computational cost than MC simulations. Future research might expand on the analysis presented in this study by considering other orbits, nominal conditions, control laws, and FoMs to analyze. Such endeavors will further enhance our understanding of uncertainty in solar-sail mission design and contribute to the development of more robust and reliable missions.

References

[1] L. Niccolai et al. “Effects of optical parameter measurement uncertainties and solar irradiance fluctuations on solar sailing”. In: *Advances in Space Research* 67.9 (May 2021), pp. 2784–2794. DOI: `10.1016/J.ASR.2019.11.037`.

[2] V. K. Srivastava et al. “Eclipse prediction methods for LEO satellites with cylindrical and cone geometries: A comparative study of ECSM and ESCM to IRS satellites”. In: *Astronomy and Computing* 2 (2013), pp. 11–17. DOI: `10.1016/J.ASCOM.2013.06.001`.

[3] A. F. Heaton and A. Artusio-Glimpse. “An update to the NASA reference solar sail thrust model”. In: *AIAA SPACE 2015 conference and exposition*. 2015.

[4] A. F. Heaton, N. Ahmad, and K. Miller. “Near Earth Asteroid Scout thrust and torque model”. In: *4th International Symposium on Solar Sailing (ISSS)*. 2017.

[5] M. A. Rozhkov, O. L. Starinova, and I. V. Chernyakina. “Influence of optical parameters on a solar sail motion”. In: *Advances in Space Research* 67 (May 2021), pp. 2757–2766. DOI: `10.1016/j.asr.2020.06.017`.

[6] B. M. Gauvain and D. A. Tyler. “A Solar Sail Shape Modeling Approach for Attitude Control Design and Analysis”. In: *6th International Symposium on Space Sailing (ISSS)*. 2023.

[7] J. R. Mansell et al. “Orbit and attitude performance of the lightsail 2 solar sail spacecraft”. In: *AIAA Scitech 2020 Forum* 1 Part F (2020), pp. 1–18. DOI: `10.2514/6.2020-2177`.

[8] M. Macdonald and C. R. Mcinnes. “Analytical Control Laws for Planet-Centered Solar Sailing”. In: *Journal of Guidance, Control, and Dynamics* 28.5 (Oct. 2005). DOI: `10.2514/1.11400`.

[9] K. F. Wakker. *Fundamentals of Astrodynamics*. 2015.

[10] B. Tapley et al. “The GGM03 Mean Earth Gravity Model from GRACE”. In: *American Geophysical Union, Fall Meeting* (2007), G42A–03.

[11] L. Rios-Reyes and D. Scheeres. “Trajectory Control for General Solar Sails”. In: *AIAA Guidance, Navigation and Control Conference and Exhibit*. 2008. DOI: `10.2514/6.2008-6830`.

[12] C. R. Ortiz Longo. *Method for the calculation of spacecraft umbra and penumbra shadow terminator points*. Vol. 3547. National Aeronautics and Space Administration, 1995.

[13] O. Montenbruck, E. Gill, and F. H. Lutze. “Satellite Orbits: Models, Methods, and Applications”. In: *Applied Mechanics Reviews* 55.2 (Apr. 2002), B27–B28. DOI: `10.1115/1.1451162`.

[14] C. R. Mcinnes. *Solar sailing: technology, dynamics and mission applications*. Springer Science & Business Media, 2004.

[15] G. Kopp. *SORCE Total Solar Irradiance Data - SORCE*. Accessed July 31, 2023. 2020. URL: `https://lasp.colorado.edu/home/sorce/data/tsi-data/`.

[16] L. Carzana, P. Visser, and J. Heiligers. “A New Model for the Planetary Radiation Pressure Acceleration for Solar Sails”. In: *2022 AAS/AIAA Astrodynamics Specialist Conference*. 2022.

[17] G. Mengali and A. A. Quarta. “Near-optimal solar-sail orbit-raising from low earth orbit”. In: *Journal of Spacecraft and Rockets* 42.5 (2005), pp. 954–958. DOI: `10.2514/1.14184`.

[18] J. A. Storch. "Aerodynamic Disturbances on Rapidly Rotating Spacecraft in Free-Molecular Flow". In: *Engineering Construction and Operations in Challenging Environments Earth and Space 2004: Proceedings of the Ninth Biennial ASCE Aerospace Division International Conference*. American Society of Civil Engineers (ASCE), 2004, pp. 429–436. DOI: `10.1061/40722(153)60`.

[19] S. R. Cook and M. A. Hoffbauer. *Measurement of Momentum Transfer Coefficients for H2, N2, CO, and CO2 Incident Upon Spacecraft Surfaces*. Tech. rep. NASA, Lyndon B. Johnson Space Center, 1997.

[20] D. Mostaza Prieto, B. P. Graziano, and P. C. Roberts. "Spacecraft drag modelling". In: *Progress in Aerospace Sciences* 64 (2014), pp. 56–65. DOI: `10.1016/J.PAEROSCI.2013.09.001`.

[21] R. M. Fredo and M. H. Kaplan. "Procedure for obtaining aerodynamic properties of spacecraft". In: *Journal of Spacecraft and Rockets* 18.4 (1981), pp. 367–373. DOI: `10.2514/3.28061`.

[22] S. Firuzi and S. Gong. "Attitude control of a flexible solar sail in low earth orbit". In: *Journal of Guidance, Control, and Dynamics* 41.8 (2018), pp. 1715–1730. DOI: `10.2514/1.G003178`.

[23] V. Stolbunov et al. "Optimal law for inclination change in an atmosphere through solar sailing". In: *Journal of Guidance, Control, and Dynamics* 36.5 (2013), pp. 1310–1323.

[24] G. Mengali and A. A. Quarta. "Near-optimal solar-sail orbit-raising from low earth orbit". In: *Journal of Spacecraft and Rockets* 42 (2005), pp. 954–958. DOI: `10.2514/1.14184`.

[25] J. H. Kang et al. "Durability characterization of mechanical interfaces in solar sail membrane structures". In: *Advances in Space Research* 67.9 (May 2021), pp. 2643–2654. DOI: `10.1016/J.ASR.2020.08.015`.

[26] United States Air Force. *U.S. Standard Atmosphere 1976*. Tech. rep. United States Air Force, 1976.

[27] J. Owens et al. "NASA Marshall Engineering Thermosphere model 1999 version (MET-99) and implications for satellite lifetime predictions". In: *Advances in Space Research* 26 (Jan. 2000), pp. 157–162. DOI: `10.1016/S0273-1177(99)01042-X`.

[28] J. M. Picone et al. "NRLMSISE-00 empirical model of the atmosphere: Statistical comparisons and scientific issues". In: *Journal of Geophysical Research: Space Physics* 107 (2002). DOI: `10.1029/2002JA009430`.

[29] M. Macdonald and C. R. Mcinnes. "Realistic Earth Escape Strategies for Solar Sailing". In: *Journal of Guidance, Control, and Dynamics* 28.2 (Apr. 2005). DOI: `10.2514/1.5165`.

[30] M. J. Walker, B. Ireland, and J. Owens. "A set modified equinoctial orbit elements". In: *Celestial Mechanics* 36.4 (Aug. 1985), pp. 409–419. DOI: `10.1007/BF01227493/METRICS`.

[31] J. T. Horwood and A. B. Poore. "Gauss von Mises distribution for improved uncertainty realism in space situational awareness". In: *SIAM-ASA Journal on Uncertainty Quantification* 2.1 (2014), pp. 276–304. DOI: `10.1137/130917296`.

[32] G. E. Uhlenbeck and L. S. Ornstein. "On the Theory of the Brownian Motion". In: *Physical Review* 36.5 (Sept. 1930), p. 823. DOI: `10.1103/PhysRev.36.823`.

[33] K. Debrabant. "Runge-Kutta methods for third order weak approximation of SDEs with multidimensional additive noise". In: *BIT Numerical Mathematics* 50 (2010), pp. 541–558.

[34] F. M. Dekking et al. *A Modern Introduction to Probability and Statistics*. Springer London, 2005. DOI: `10.1007/1-84628-168-7`.

[35] Y. zhong Luo and Z. Yang. "A review of uncertainty propagation in orbital mechanics". In: *Progress in Aerospace Sciences* 89 (Feb. 2017), pp. 23–39. DOI: `10.1016/j.paerosci.2016.12.002`.

[36] S. J. Julier, J. K. Uhlmann, and H. F. Durrant-Whyte. "A new method for the nonlinear transformation of means and covariances in filters and estimators". In: *IEEE Transactions on Automatic Control* 45.3 (2000), pp. 477–482. DOI: `10.1109/9.847726`.

[37] S. J. Julier and J. K. Uhlmann. “Unscented filtering and nonlinear estimation”. In: *Proceedings of the IEEE*. Vol. 92. 3. Mar. 2004, pp. 401–422. DOI: `10.1109/JPROC.2003.823141`.

[38] J. T. Horwood, N. D. Aragon, and A. B. Poore. “Gaussian sum filters for space surveillance: theory and simulations”. In: *Journal of Guidance, Control, and Dynamics* 34.6 (2011), pp. 1839–1851.

[39] B. Diedrich. “Solar Sail Torque Model Characterization for the Near Earth Asteroid Scout Mission”. In: *6th International Symposium on Space Sailing (ISSS)*. 2023.

C

Conclusion

This chapter builds upon the conclusion presented in the "Paper" Chapter B of this thesis by evaluating how the thesis' research questions were answered, as well as through a detailed future work discussion.

C.1. Research questions

In light of the results and conclusions presented in this thesis, we re-visit the research questions posed in the "Introduction" Chapter A and evaluate how they have been answered through the work presented.

Q1. Which of the uncertainty sources affecting the solar radiation pressure acceleration is the strongest?
Section 4.2 discusses which of the sail optical coefficient or deformation parameters are the most influential uncertainty sources. The results show that the specularity is the most significant source of uncertainty, followed by the reflectivity. On the other hand, Section 5.2 evaluates the effects of the attitude uncertainty on the mean and standard deviation of the figures of merit, which strongly depend on the Ornstein-Uhlenbeck parameters selected. Thus, whether the attitude offset is a stronger uncertainty than the sail's optical coefficients or deformation depends on the nature of the offset.

Q2. How does each of the sources of uncertainty affect the achievable altitude and inclination change after a maneuver (which are key figures of merit)?
Sections 4.3 and 4.4 reveal that the influence of the uncertain sail optical coefficients and deformation parameters causes the figures of merit to behave as normal distributions, with the mean value being approximately equal to the nominal value. For large uncertainties, on the other hand, more complex behaviours appear, such as truncation and skewness of the distribution. Section 5.1, on the other hand, shows that under uncertain attitude, the figures of merit distributions skew towards the negative values. The mean of these distributions lays below the nominal performance, as this uncertainty causes a deviation from a near-optimal control profile.

Q3. Is there significant coupling between different uncertainty sources? To what extent can one approximate the combined effect of all uncertainty sources be approximated by considering a reduced number of sources (can some sources of uncertainty be neglected)?
Section 4.4 analyzes the combined effect of the uncertainty in the sail's optical coefficients and deformation parameters, and compares it to the effect of only uncertain specularity and uncertain specularity and reflectivity. It was found that there is no significant coupling, and the emissivity, Lambertian coefficient, and

deformation uncertainties can be effectively neglected. No analysis of the coupled effect of uncertain attitude and uncertain sail optical coefficients and deformation parameters was produced, and thus could be an area of future work.

Q4. How does the uncertainty in figures of merit evolve in time?
Section 4.3 details how the distribution of the figure of merit due to uncertain specularity behaves at different points in time. It was found that, once scaled by the nominal figure of merit gain at each time, the distribution is independent of the simulation time. It was found that the standard deviation of the distribution of the figure of merit grows linearly in time, with the speed of growth being driven by the strength of the source of uncertainty. Considering the strong dominance of the specularity uncertainty, one might safely extrapolate these findings to the rest of constant random value uncertainties. Section 5.1 presents a more complex picture of the time evolution of the uncertainty distribution in time due to attitude uncertainty. While the normalized relative mean was found to be constant in time, the normalized standard deviation of the distributions was found to decrease in time until it approaches a stationary value.

Q5. Is the Gauss von Mises uncertainty propagation method an accurate estimator of uncertainty?
The Gauss von Mises method was used alongside the Monte Carlo method for the results shown in Section 4. Thus, since the results of the Monte Carlo simulations can be treated as truth values, all the results presented in Section 4 serve as a validation mechanism for the Gauss von Mises method. In general, the Gauss von Mises method was found to be accurate for the orbits and figures of merit considered, as it was able to capture the mean and standard deviations accurately. It was also found capable of accurately capturing the shape of the distribution, provided it was approximately normal. In terms of computational cost, the Gauss von Mises method proved to be orders of magnitude faster than the Monte Carlo method, which highlights its usefulness for preliminary uncertainty analysis. Future work should analyse whether the Gauss von Mises method is capable of capturing the distribution of figures of merit that do not behave as simple normal distributions.

Q6. How does the answer to previous questions change when considering different orbits, mission dates, or figures of merit?
Sections 4.2, 4.3, 4.4, and 5.2 presented detailed results for two orbit's local time of the ascending node (LTAN), 6 AM and 12 AM, and for two different steering laws and figures of merit. Section 4.5 and 5.3 presented results for different combinations of orbit LTAN and mission dates for these two steering laws and figures of merit. Through these results, conclusions on the influence of these factors were drawn. However, a Sun-synchronous 700-km-high orbit was always assumed, as well as only two locally-optical steering laws and their corresponding figures of merit. Future work should consider a more diverse family of orbits and control laws.

C.2. Future work

The results presented in this thesis open the door for several areas of further research that would serve to improve our understanding of uncertainties in solar sailing in the near-Earth environment. These are briefly covered in this section, subdivided into three thematic areas: study of different orbits, study of different uncertainties, and validation of the results.

C.2.1. Study of different orbits

The results presented in this thesis focused on solar sails in Sun-synchronous orbits because these are orbits of special interest to solar-sail missions, including the upcoming Advanced Composite Solar Sail System (ACS3) mission [1]. A nominal altitude of 700 km was assumed based on early launch opportunities for the ACS3 mission, which additionally introduced significant aerodynamic forces on the sail. Finally, simple

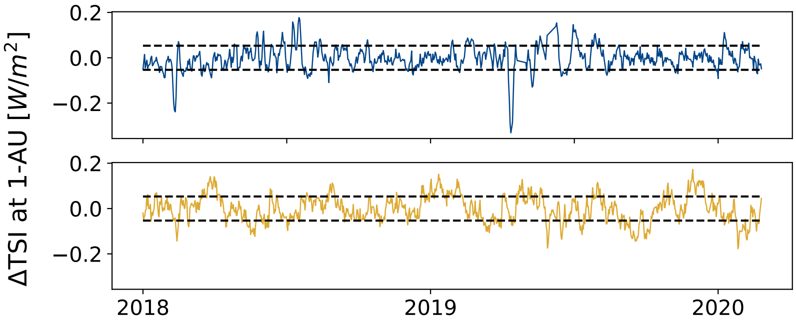

Figure C.1: Top graph represents the difference between the TSI and the TSI half-year mean. Bottom graph is a realization of an Ornstein-Uhlenbeck process with $\sigma = 0.0294$ day$^{-1/2}$ and $\theta = 0.1525$ day^{-1}. Black dashed lines represent the stationary standard deviation.

orbit-raising or inclination-changing locally-optical steering laws were considered. Further research on uncertainties for solar sails should deviate from these assumptions by considering different nominal conditions in order to expand our understanding of the behaviour of solar sails in the near-Earth environment.

Given the large area of solar sails, aerodynamic forces stand to have a significant influence on the trajectory of sailcraft. As such, studying different orbital altitudes would be of particular interest for solar sail missions in low-Earth orbit, especially if these studies include uncertain aerodynamic forces. Similarly, this thesis considered only the family of Sun-synchronous orbits, but solar-sail missions may develop in other orbits around the Earth in the near future, and thus should be investigated. For instance, there has been some interest on the de-orbit of debris in geostationary orbit through solar sails [2, 3]. The conditions in geostationary orbit are very different from low-Earth Sun-synchronous orbits, and thus a dedicated uncertainty study should be considered, especially under the strict requirements of rendez-vous operations.

This study focused on two control laws and two figures of merit for analysis. However, future missions might follow other steering laws and have other mission objectives. The TugSat concept, for instance, aims to rendez-vous with spacecraft in geostationary orbit using a control law capable of targeting a specific semi-major axis, eccentricity, inclination, and longitude [2]. The position and velocity errors with respect to the desired rendez-vous point might be interesting figures of merit to analyze in this scenario. On the other hand, mission planning for the ACS3 mission has additionally considered especial control maneuvers used to calibrate the force produced by the solar sail while in orbit [4]. The objective of these calibration orbits is to minimize all forces except one, which should be maximized in order to better characterize it. As such, it might be of interest to study how the uncertainties cause the other forces to appear, and thus quantify the level of “noise” that should be expected on the measurements of the force of interest.

C.2.2. Other sources of uncertainty

The introduction to this thesis, see Chapter A, covered many sources of uncertainty for solar sails in the near-Earth environment. Only a selection of these, those which were deemed the most influential, were studied in detail in this thesis, so future work might expand on the analysis presented here by considering other of sources of uncertainty.

The Total Solar Irradiance (TSI) of the Sun, which affects the magnitude of the solar radiation pressure, behaves in an unpredictable manner. A previous study for uncertainty in heliocentric orbits analyzed the uncertainty due to this factor, and found it to be more influential than the emissivity or Lambertian coefficient optical coefficients [5]. Their approach, however, considered the TSI to be constant during propagation, unlike the random behaviour exhibited in empirical data, see Figure A.3. Future work could use Ornstein-Uhlenbeck stochastic processes to generate a more realistic model of the erratic behaviour of the TSI, see

Figure C.1. Moreover, the times when spacecraft enter and exit the penumbra and umbra of the Earth are hard to predict exactly [6]. Thus, high-accuracy uncertainty studies might also considered these times to be uncertain.

Aerodynamic forces also represent a strong source of uncertainty for solar sails. As it was discussed in the introduction to this thesis, the drag and lift coefficients of the sail depend on a variety of factors that are hard to estimate, and thus are bound to be uncertain. The atmospheric density and winds are also difficult to predict given the inherent chaotic behaviour of the atmosphere and of the factors that influence it, such as the solar and geodetic activity coefficients. This makes studying this source of uncertainty critical for missions that operate at low altitudes, such as those intended for debris de-orbit [7, 8].

This thesis presented a simple analysis of the effects of uncertain sail shape. The model employed only considered boom bending and membrane billowing due to thermal deformations. However, engineers from the ACS3 mission have remarked on the many possible sources of uncertainty for the shape of a sail in orbit. Thus, it would be of interest to consider a more complex shape model for the sail, with more parameters to consider uncertain. Instead of a single square membrane, the sail might be broken down into individual quadrants, which is a closer representation to sails used in missions like the ACS3 mission. Each quadrant might feature differently deflected support booms, displaced connection points, irregular membrane tensioning, incomplete deployment, and so forth. Moreover, tears and holes might appear in the membrane at random points, which would impact the effective sail shape.

C.2.3. Validation of the results

The quality and completeness of the results presented might be increased through a series of validation processes. Validation with mission data should be a priority, and might be possible in the near future assuming success of the ACS3 mission. Barring the use of empirical data, these results might be validated by employing more accurate dynamical models and asserting that the results do not change meaningfully under these high-fidelity dynamics. Such higher-fidelity models can include the consideration of planetary radiation pressure force, higher-order gravity terms, the use of more complex atmospheric models, and higher-fidelity drag and lift coefficient models.

Moreover, the results presented in this study assumed a prescribed, albeit sometimes perturbed, attitude profile. Future studies might consider the coupled propagation of the attitude and position of the sail. This stands to be especially interesting for studies of uncertain sail shapes, as the shape of the sail affects mostly the torque generated by the sail, and not so much the force [9]. Finally, the coupled effect of uncertain sail optical coefficient, deformation parameters, and attitude offset might be studied, and the conclusion that there exist no significant coupling between uncertainties revisited.

Conclusion Bibliography

[1] W. K. Wilkie. “Overview of the NASA Advanced Composite Solar Sail System (ACS3) Technology Demonstration Project”. In: *AIAA Scitech 2021 Forum*. 2021. DOI: `10.2514/6.2021-1260`.

[2] P. W. Kelly et al. “TugSat: Removing space debris from geostationary orbits using solar sails”. In: *Journal of Spacecraft and Rockets* 55.2 (Jan. 2018), pp. 437–450. DOI: `10.2514/1.A33872`.

[3] P. Kelly and R. Bevilacqua. “An optimized analytical solution for geostationary debris removal using solar sails”. In: *Acta Astronautica* 162 (Sept. 2019), pp. 72–86. DOI: `10.1016/J.ACTAASTRO.2019.05.055`.

[4] L. Carzana et al. “Solar-sail Steering Laws to Calibrate the Accelerations from Solar Radiation Pressure, Planetary Radiation Pressure, and Aerodynamic Drag”. In: *6th International Symposium on Solar Sailing (ISSS)*. 2023.

[5] L. Niccolai et al. “Effects of optical parameter measurement uncertainties and solar irradiance fluctuations on solar sailing”. In: *Advances in Space Research* 67.9 (May 2021), pp. 2784–2794. DOI: `10.1016/J.ASR.2019.11.037`.

[6] V. K. Srivastava et al. “Eclipse prediction methods for LEO satellites with cylindrical and cone geometries: A comparative study of ECSM and ESCM to IRS satellites”. In: *Astronomy and Computing* 2 (2013), pp. 11–17. DOI: `10.1016/J.ASCOM.2013.06.001`.

[7] C. Colombo et al. “Drag and Solar Sail Deorbiting: Re-Entry Time Versus Cumulative Collision Probability”. In: *68th International Astronautical Congress (IAC) Proceedings* (2018), pp. 3535–3553.

[8] C. Bianchi et al. “Blended Locally-Optimal Control Laws for Space Debris Removal in LEO Using a Solar Sail”. In: *6th International Symposium on Space Sailing (ISSS)*. 2023.

[9] B. M. Gauvain and D. A. Tyler. “A Solar Sail Shape Modeling Approach for Attitude Control Design and Analysis”. In: *6th International Symposium on Space Sailing (ISSS)*. 2023.

Acknowledgements

This thesis was partly carried out at the Colorado Center for Astrodynamic Research, at the University of Boulder Colorado. Dr Hanspeter Schaub acted as the hosting professor and provided technical support during the completing of the thesis. The University of Boulder Colorado, the Center for Astrodynamic Research, and the Autonomous Vehicle Systems Laboratory provided economic support to the author.

The project that gave rise to these results received the support of a fellowship from the la Caixa Foundation (ID 100010434). The fellowship code is LCF/BQ/EU21/11890118.

This work utilized the “eudoxos” computing resource at the Delft University of Technology.

D

Simulation Setup

This appendix introduces the software used to produce the results shown in this thesis. The first section introduces the Basilisk framework, the selected tool to perform dynamics simulation and propagation, while the second section details the specific Basilisk-based implementation used in this work.

D.1. The Basilisk framework

All results presented in this thesis were obtained through simulations using the Basilisk spacecraft simulation framework [1]. Basilisk is a highly-modular tool that allows users to model and efficiently propagate the dynamics of complex spacecraft in arbitrary environments. The tool is composed of atomic "modules" that perform some operation on data and "messages" that are used to pass data around modules.

All modules, messages, and the simulation architecture, are written in C++ or C, which means that Basilisk is very performant. However, users of Basilisk configure their simulations through Python scripts, which makes Basilisk more accessible to the average engineer. Each module and message is exposed to Python through the SWIG tool (Simplified Wrapper and Interface Generator) [2]. Users can configure and connect these exposed modules however they please in order to reach their simulation objectives. Thus, assuming that Basilisk has all necessary modules available out-of-the-box, one can write simulation scripts purely through Python, without need of knowing, writing, or compiling C/C++ code. The approach of using C/C++ for the computationally expensive operations and Python for easy configuration of the simulations is also used by Tudat, the Delft University of Techonology astrodynamics toolbox [3].

Performing all simulations through Basilisk instead of writing a custom astrodynamics simulation software comes with significant advantages. Establishing a new flexible and efficient simulation architecture in C++ is a complex task that would have been out of scope for this project. Implementation time was saved by leveraging out-of-the-box modules, developing new code from the existing codebase, and making use of the Basilisk testing suite for validation. Finally, the Basilisk development team was regularly available to provide advice during the implementation of new code.

The results presented in this thesis required the implementation of several custom C++ modules. Many solar sail dynamic models were not available out-of-the-box for Basilisk, as this is the first research of this kind completed with the tool. Moreover, Basilisk was written under the assumption of deterministic dynamics. It was necessary to extend the Basilisk state machine and integrator suite to handle the integration of stochastic differential equations.

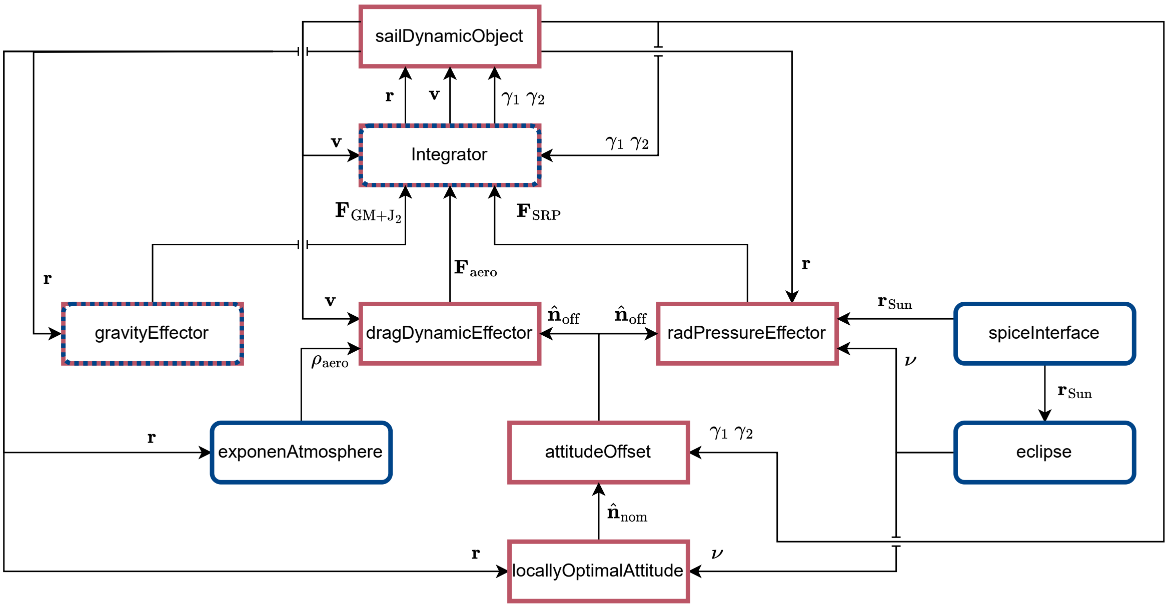

Figure D.1: Diagram of the Basilisk simulation setup.

D.2. Basilisk setup

Figure D.1 shows the Basilisk setup used to obtain the results presented in this work. The blocks shown in the figure correspond to individual “modules”, while arrows represent the flow of information through “messages”. Blocks with rounded blue contours required none or minimal modifications to existing modules. Blocks with square red contours were written from the ground up or involved heavy modification to existing code. Blocks that alternate rounded blue and square red contours involved a refactor and slight improvement of existing code.

The following enumeration briefly covers the functionality of each module. Underlined items correspond to modules that required significant implementation effort, i.e. the blocks with square red contour in Figure D.1:

- **sailDynamicObject**: this module represents the solar sail. Its main purpose is to keep track of the state of the spacecraft at any point in time. It works closely with the integrator to update the spacecraft’s state and output it to other modules in the scenario that need state information. The way the objects of this kind handle states was adapted to support having a prescribed attitude profile and stochastic states (used for the γ_1 and γ_2 offsets, see Section 3.2).

- **Integrator**: while Basilisk had pre-existing integration capabilities, part of the work of this thesis was rewriting all existing integrators to more modern and maintaible C++. Moreover, stochastic integrators were not supported. This work involved the implementation from the ground up of the stochastic integrator discussed in Appendix F.

- **gravityEffector**: this module produces the gravity force vector given the position of the spacecraft with respect to the Earth. During this work, this module was completely refactored. While this was not necessary for the completion of the thesis, the module was originally written several years ago and with poor coding practices. As a contribution to the Autonomous Vehicle Systems Laboratory, which maintains Basilisk and hosted the author during the completion of their thesis, the module was rewritten in a more maintainable and modular way.

- **dragDynamicEffector**: this module produces the aerodynamic force vector given the velocity of the spacecraft, the atmospheric density, and the attitude of the sail. Existing drag models in Basilisk used a simple cannonball model or a computationally-expensive facet-based drag model. For this work, the flat plate hyperthermal free-molecular flow model introduced in Section 2.2 was implemented.

- **exponenAtmosphere**: this module produces the atmospheric density at a given altitude according to the 1976 U.S. Standard Atmosphere.
- **radPressureEffector**: this module produces the SRP force vector given the position of the Sun with respect to the sail, the attitude of the sail, and the shadow factor, ν. Basilisk supported three SRP models: a simple cannonball model, a look-up model, and a GPU-enabled pure-reflective faceted model. Two new SRP models were implemented: a simple flat sail with specular and diffuse reflection on one side and emissivity on both sides, and the Generalized Sail Model introduced in Section 2.2.
- **spiceInterface**: this module produces the position of the Sun with respect to the Earth at any point in time by interfacing with the SPICE SPK toolkit.
- **eclipse**: this module generates the shadow factor, ν, given the position of the Sun according to the conical shadow model, as introduced in Section 2.2.
- **locallyOptimalAttitude**: this module computes the locally optimal sail normal direction given the position of the sail, as shown in Section 2.3. However, if the sail is in umbra, $\nu = 0$, the sail is oriented edgewise to the atmospheric flow to minimize drag. This module was written from the ground up.
- **attitudeOffset**: this module takes a nominal direction, $\hat{\mathbf{n}}_{\text{nom}}$, and the values of the angles γ_1 and γ_2 and applies the corresponding offset through the procedure described in Section 3.2. This module was written from the ground up.

E

Experiment Setup

Appendix D covered the Basilisk setup used to propagate the state of a solar sail for a certain period. In order to produce the results shown in this work, however, many such propagations were required. This appendix provides a glimpse into the ecosystem of utilities used to efficiently manage and post-process these propagations.

E.1. Simple propagations

A “simple propagation" experiment corresponds to a single integration of the dynamics of a solar sail. While the setup presented in Section D is the same for all propagations, it is possible to define different initial conditions, sail configurations, dynamical models, and so forth to produce different results.

```
scenario_config = ScenarioConfiguration(
    dynamics=DynamicalModel(
        gravity=GravityModel.J2,
        aero=AerodynamicModel.FLAT_PLATE_EXPONENTIAL,
        solar=SolarPressureModel.GSM_CONICAL_SHADOW,
    ),
    integration=Integration(
        integrator_type=IntegratorType.RKF78,
        time_step=10, # s
        simulation_time=(10*24*3600), # s
        abs_tol=0, # turns off adaptive time steps
        rel_tol=0, # turns off adaptive time steps
    ),
    sail=SailConfiguration(
        description="ACS3",
        mass=15, # kg
        area=80, # m^2
        reflectivity=0.91,
        specularity=0.89,
        front_lambertian_coefficient=0.79,
        back_lambertian_coefficient=0.67,
        front_emissivity=0.025,
        back_emissivity=0.27,
        billow=0.05, # m
        tip_offset=0.08, # m
    ),
    initial_conditions=InitialConditions.for_sso_circular_orbit(
```

```python
        description="Dawn-Dusk Sun Syncronous Circular Orbit",
        initial_time="2023 11 1 00:00:00",
        a=(6371 + 700) * 1000,  # altitude 700km
        ltan=6,
        f=0,
    ),
    control=Control.LOCALLY_OPTIMAL_SEMIMAJOR_AXIS,
    stochastic_uncertainties=[UncertainAttitude.from_stationary_std(
            offset_theta=1e-5,
            offset_stationary_std=3 / 180 * np.pi,
    )],
    outputs=[
        Output.TIME,
        Output.POSITION_AND_VELOCITY,
        Output.ORBITAL_ELEMENTS,
        Output.CONTROL_ANGLES,
        ModifiedOutput(
            operation=OutputModificationOperation.LINEARIZE,
            output=Output.ORBITAL_ELEMENTS,
        ),
    ],
)
```

Listing E.1: Python code required to configure a simple propagation experiment through the utility classes and methods developed for this thesis.

Listing E.1 shows an example of how a simple propagation might be configured. `ScenarioConfigure` are dataclass-like objects created for this thesis that encapsulate other custom sub dataclass-like objects. The first of such objects is the `DynamicalModel` object, which allows one to choose what dynamics to use for propagation. The `Integration` object allows control over the integrator and the total simulation time. `SailConfiguration` allows one to specify the parameters describing the solar sail. `InitialConditions` objects store the initial date, position, and velocity of the sail, but they can be defined through a variety of helper methods, such as `from_orbital_elements` or `for_sso_circular_orbit`. The `Control` object is a simple enumerator that allows one to choose whether to use locally optimal semi-major axis or inclination control. The `stochastic_uncertainties` parameter accepts an optional sequence of uncertainties defined through stochastic processes (only the attitude uncertainty, as discussed in Section 3.2, is available). Finally, the `outputs` parameter allows one to define what results to extract from the simulation.

```python
scenario = Scenario(scenario_config)
scenario.execute()
t, a = scenario.get_outputs_with_name("time", "semimajor_axis")
```

Listing E.2: Python code required to run a simple propagation and extract results through the utility classes and methods developed for this thesis.

Given this configuration, one can propagate the scenario using the code shown in Listing E.2. The object `Scenario` creates the relevant Basilisk modules, configures them with the values provided in `scenario_config`, and connects them following the diagram shown in Appendix D. Once the simulation has run, outputs can easily be extracted from the `scenario` object for post-processing.

E.2. Monte Carlo simulations

While simple propagations are useful to provide context for a specific set of conditions, the main focus of this work is the study of uncertainty through sample-based uncertainty propagation methods, see Section 3.3. As such, it is necessary to run multiple simulations, possibly changing the scenario configuration every time to account for the uncertainties in the system. In order to facilitate defining, running, storing, loading, and post-processing Monte Carlo experiments, a series of utility objects and functions have been created.

```python
experiment = MonteCarloExperiment(
    description="Sail at DD SSO, on Nov 1st, with uncertain reflectivity and 
    specularity",
    nominal_scenario=scenario_config,
    rv_uncertainties=[SailRVUnceratinty(
        reflectivity_std=0.005,
        specularity_std=0.045,
    )],
    options=MonteCarloOptions(
        n_samples=1000, jobs=14, chunk_size=5
    ),
)

experiment.run_or_load(save_folder="dd_sso_nov_ref_spc")
```

Listing E.3: Python code required to configure and run a Monte Carlo experiment through the utility classes and methods developed for this thesis.

A Monte Carlo experiment is defined through code resembling the excerpt shown in Listing E.3. The nominal scenario must be provided, as well as the random value uncertainties to consider, see Section 3.1. In the example shown in Listing E.3, a `SailRVUnceratinty` object is provided as a random value uncertainty, which will modify the scenario by randomly changing the optical coefficients of the sail according to a normal distribution with the provided standard deviations. In this case, only reflectivity and specularity are randomly modified. Finally, `MonteCarloOptions` must be passed to configure the number of samples to use as well as the parallization options.

The first time the code is run, the method `run_or_load` will run the Monte Carlo experiment and save the results in a folder. This folder will store the results for each individual sample run, as well as the overall mean and covariance matrix obtained from them. Moreover, text representations (serializations) of the nominal scenario configuration and random value uncertainty objects are saved for reference, as well as the SHA256 hash of these texts.

Once the experiment has been run and saved, re-running the code will only generate the SHA256 hash of the given nominal scenario and uncertainties, compare this hash to the saved hash, and load the cached results only if the hashes coincide. If the hashes are different, however, the experiment is re-run. This only happens when the experiment configuration, i.e., the nominal scenario or the uncertainties, have been modified and thus the cached results are outdated.

E.3. Gauss von Mises experiments

A set of utility objects and functions very similar to those defined for Monte Carlo experiments are implemented for Gauss on Mises experiments.

```python
experiment = GaussVonMisesExperiment(
    description="Sail at DD SSO, on Nov 1st, with uncertain reflectivity and 
    specularity",
    nominal_scenario=scenario_config,
    rv_uncertainties=[SailRVUnceratinty(
        reflectivity_std=0.005,
        specularity_std=0.045,
    )],
    options=GaussVonMisesOptions(
        jobs=14, chunk_size=5
    ),
```

```
)

experiment.run_or_load(save_folder="dd_sso_nov_ref_spc")
```

Listing E.4: Python code required to configure and run a Gauss von Mises experiment through the utility classes and methods developed for this thesis.

Listing E.4 displays the code used to define and run/load a Gauss von Mises experiment. The result-caching algorithm for Gauss von Mises results is very similar to that of Monte Carlo results, except that Gauss von Mises results additionally store the distribution parameters obtained through the Gauss von Mises method, $\boldsymbol{\mu}_\mathcal{G}$, $\boldsymbol{\Sigma}_\mathcal{G}$, $\alpha_\mathcal{G}$, $\boldsymbol{\beta}_\mathcal{G}$, $\boldsymbol{\Gamma}_\mathcal{G}$, and $\kappa_\mathcal{G}$, see Section 3.3. Additionally, note that the number of samples are not defined in `GaussVonMisesOptions`, as this number is prescribed by the method.

F

Stochastic Integrator

A stochastic integrator is required to integrate the trajectory of spacecraft whose dynamics are defined by stochastic differential equations, for instance, if they have a randomly evolving attitude profile as described in Section 3.2. In this paper, the weak third-order, additive-noise stochastic integrator proposed by Debrabant [4] is used. Integrators that assume additive noise require the dynamics to have a "diffusion" term that does not depend on the state of the system, where the "diffusion" term is the rapidly varying random component of the dynamics [5]. For the case of the Ornstein-Uhlenbeck processes presented in Section 3.2, this is the "$\sigma d\beta_{\mathrm{Br}}$" term, which meets the definition of additive noise as σ is constant. The integrator proposed by Debrabant was chosen because it achieves a high weak order while not being exceedingly complex to implement.

The concept of a weak third-order integrator is related to the convergence of the algorithm. For deterministic integrators, such as the commonly used Runge-Kutta integrators, the order of the method indicates the relationship between the time step used for integration and the numerical error introduced at each step. This error evolves exponentially with respect to the time step, with the exponent being the order of the method:

$$|y - \tilde{y}^{(\Delta t)}| \leqslant C\Delta t^{\Pi} \tag{F.1}$$

where y is the real solution of the integration, $\tilde{y}^{(\Delta t)}$ is the approximation produced by the integrator using time step Δt, Π is the order of the method, and C is some constant. This means, for example, that halving the time step used in a third-order deterministic integrator will lead to estimating y $2^3 = 8$ times more accurately.

Defining measures of converge for stochastic integrators is more complicated. Because the process is inherently random, the solution of the integration, $Y(t)$, as well as the approximation produced by the integrator, $\tilde{Y}^{(\Delta t)}(t)$, are random variables. Thus, one can define two orders of convergence, the weak order and the strong order. Of interest to this work is the weak order. Formally, one says that a discrete approximation $\tilde{Y}^{(\Delta t)}(t)$ with time step Δt converges weakly with order Λ at time t_f for each function $g \in \mathcal{C}_P^{2(\Lambda+1)}$[1] if one can find a constant C such that [5]:

$$|E[g(Y(t_f))] - E[g(\tilde{Y}^{(\Delta t)}(t_f))]| \leqslant C\Delta t^{\Lambda} \tag{F.2}$$

where $E[]$ represents the expected (mean) operator.

The functional space $\mathcal{C}_P^{2(\Lambda+1)}$ contains all polynomials, which means that any moment (mean, variance, standard deviation...) may be approximated with an error bound by $C\Delta t^{\Lambda}$ for a discrete approximation

---

[1] The functional space $\mathcal{C}_P^n$ represents the space of n-times continuous differentiable functions which, together with their partial derivatives of order up to n, have polynomial growth.

Table F.1: Modified Butcher table for the coefficients of a stochastic Runge-Kutta method in the form shown in Eqs. F.4 and F.5.

c_1	a_{11}	a_{12}	$\dots$	a_{1s}	d_1	d_1^*
c_2	a_{21}	a_{22}	$\dots$	a_{2s}	d_2	d_2^*
$\vdots$	$\vdots$	$\vdots$	$\ddots$	$\vdots$	$\vdots$	$\vdots$
c_s	a_{s1}	a_{s2}	$\dots$	a_{ss}	d_s	d_s^*
	b_1	b_2	$\dots$	b_s		

Table F.2: Coefficients of the weak third-order method developed by Debrabant in the modified Butcher table format shown in Table F.1 [4].

0	0	0	0	0	d	d^*
1	1	0	0	0		
1/2	3/8	1/8	0	0		
1	-0.4526683126055039	-0.4842227708685013	1.9368910834740051	0		
	1/6	-0.005430430675258792	2/3	0.1720970973419255		

$d = [-0.01844540496323970, 0.8017012756521233, 0.5092227024816198, 0.9758794209767762]^T$

$d^* = [-0.1866426386543421, -0.8575745885712401, -0.4723392695015512, 0.3060354860326548]^T$

scheme of weak order Λ. This means, for example, that halving the time step used in a weak third-order stochastic integrator will lead to estimating the mean of the distribution $2^3 = 8$ times more accurately.

Let us consider a stochastic differential equation in the form:

$$dy = f(t,y)dt + \sum_{l=0}^{m-1} \Sigma_l d\beta_{\mathrm{Br}}^{(l)}(t) \qquad y(t_0) = y_0 \qquad \text{for } t \in [t_0, t_f] \tag{F.3}$$

where an m-dimensional Wiener process $\beta_{\mathrm{Br}}(t) \in \mathbb{R}^m$ is considered. The goal is to find a discretized solution to this equation, $y = \{y_0 = y(t_0), y_1 \approx y(t_1), \dots, y_n \approx y(t_n), \dots, y_N \approx y(t_f)\}$, where $t_{n+1} - t_n = \Delta t$.

Debrabant [4] proposes a family of s-stage stochastic Runge-Kutta methods that can be expressed in a format similar to deterministic Runge-Kutta integrators:

$$y_{n+1} = y_n + \Delta t \sum_{i=0}^{s-1} b_i k_i + \sqrt{\Delta t} \sum_{l=0}^{m} \Sigma_l J_l \tag{F.4}$$

where

$$k_i = f\left(t_n + c_i \Delta t, y_n + \Delta t \sum_{j=0}^{i-1} a_{ij} k_j + \sqrt{\Delta t} \sum_{l=0}^{m-1} (d_i J_l + d_i^* J_l^*) \Sigma_l\right) \tag{F.5}$$

and where J_l and J_l^* are values that are independently drawn during every integration step from a random distribution whose moments coincide with those of the standard normal distribution. The coefficients a_{ij}, b_i, c_i, d_i, and d_i^* can be expressed in the format of a modified Butcher table, see Table F.1. They are dependent on the specific stochastic Runge-Kutta method being used. Table F.2 shows the coefficients found by Debrabant for their weak third-order method. Note that the method is explicit because $a_{ij} = 0$ for $j \geqslant i$.

G

Verification and Validation

Given the large amount of software that had to be written during this thesis, a thorough verification and validation campaign is essential to guarantee the correctness of the results. This appendix briefly covers how such a campaign was implemented. The appendix is divided into three sections, each focused on the verification and validation of a different set of implementations: those related to the dynamics, the stochastic integrator, and finally to the Gauss von Mises method.

G.1. Dynamics

As discussed in Appendix D, all necessary dynamical models were implemented through Basilisk. Several Basilisk modules were written, which were independently verified. The Basilisk software has an automated testing policy, which means that if one defines verification tests for a module, all such tests will be automatically run every time the testing suite is run. This ensures the continuous correct integration of all modules.

A key component of the verification and validation campaign for the dynamics has been access to a set of reference solutions. Carzana provided six propagations of a solar sail trajectory using different initial conditions and the locally optimal inclination or semi-major axis control laws. These solutions not only contained the state of the sail along its trajectory, but also the control angles of the sail, normal direction of the sail, shadow factor, atmospheric density, and forces acting on the sail, broken down into atmospheric forces, SRP forces, and gravity forces. This information was used to verify and validate the dynamics.

G.1.1. Verification

The verification of each module, as defined in Appendix D, consisted of:

- **gravityEffector**: Existing Basilisk tests for the module were used to verify that the refactor did not introduce bugs on the gravitational models.
- **Deterministic integrators**: Existing Basilisk tests for the deterministic integrators were used to verify that the refactor did not introduce bugs.
- **dragDynamicEffector**:
  - Check that the drag and lift forces are produced in the correct direction for certain simple sail attitudes:
    - ◇ Sails parallel to the flow ought to produce no lift or drag.

        - ◇ Sails perpendicular to the flow should produce drag in the direction of the flow and no lift.
        - ◇ Sails with a positive angle of attack should produce lift in the upward direction and drag in the direction of the flow.
    - Comparison of force results generated by the (C++) module and an equivalent Python implementation of the same formulas.
    - Comparison of the force results generated by the module and the reference results provided by Carzana at five different points in time during propagation for the six reference solutions.

- **radPressureEffector**: Only tests for the Generalized Sail Model are discussed, as the flat sail model was not used to obtain any results shown in this work:
    - Test that the produced SRP force is contained in the plane defined by the sail's normal and the direction of sunlight, which would be expected given the symmetry of the sail shape, and verifies the assumption that the “roll" angle of the sail may be ignored.
    - Test that the force obtained through the Generalized Sail Model for a (non-)ideal flat sail corresponds to the force produced by a (non-)ideal flat sail, as defined by the Equations shown in Reference [6].
    - Test that the force obtained through the Generalized Sail Model for an ideal non-flat sail corresponds to the force produced by the faceted specular-reflective SRP model implemented in Basilisk.
    - Test that the force obtained through the Generalized Sail Model for an ideal flat sail corresponds to the force provided by Carzana at five different points in time during propagation for the six reference solutions.

- **locallyOptimalAttitude**: Verify that the optimal normal direction produced by the module corresponds to the optimal normal direction provided by Carzana at five different points in time during propagation for the six reference solutions, which includes different shadow conditions and the semi-major axis and inclination optimal control laws.

- **attitudeOffset**:
    - Assert that when there is no angular offset, $\gamma_1 = \gamma_2 = 0$, the offset direction is the same as the nominal direction, $\hat{\mathbf{n}}_{\text{off}} = \hat{\mathbf{n}}_{\text{nom}}$.
    - Verify that the projection of the offset direction, ($\hat{\mathbf{n}}_{\text{nom}}$, on the $\hat{\mathbf{x}}_{\text{off}}, \hat{\mathbf{z}}_{\text{off}}$) plane is angled by γ_1 with respect to the $(\hat{\mathbf{y}}_{\text{off}}, \hat{\mathbf{z}}_{\text{off}})$ plane.
    - Verify that the projection of the offset normal, $\hat{\mathbf{n}}_{\text{off}}$, on the ($\hat{\mathbf{y}}_{\text{off}}, \hat{\mathbf{z}}_{\text{off}}$ plane is angled by γ_2 with respect to the $(\hat{\mathbf{x}}_{\text{off}}, \hat{\mathbf{z}}_{\text{off}})$ plane.

- **exponenAtmosphere, spiceInterface, eclipse**: Assumed verified given that they were existing modules in Basilisk with associated unit tests.

G.1.2. Validation

The dynamics were validated by ensuring that the complete simulation setup could replicate the results for the reference solutions provided by Carzana. The comparison is performed for a solar sail starting in a circular Sun-synchronous orbit with an LTAN at 9 AM. The following initial conditions are used:

$$\left\{a, e, i, \Omega, \omega, \bar{f}, t\right\}_0 = \{6598.1363 \text{ km},\ 0,\ 96.395 \text{ deg},\ 325.5833\text{deg},\ 0 \text{ deg},\ 0 \text{ deg},\ 2023/04/01\} \tag{G.1}$$

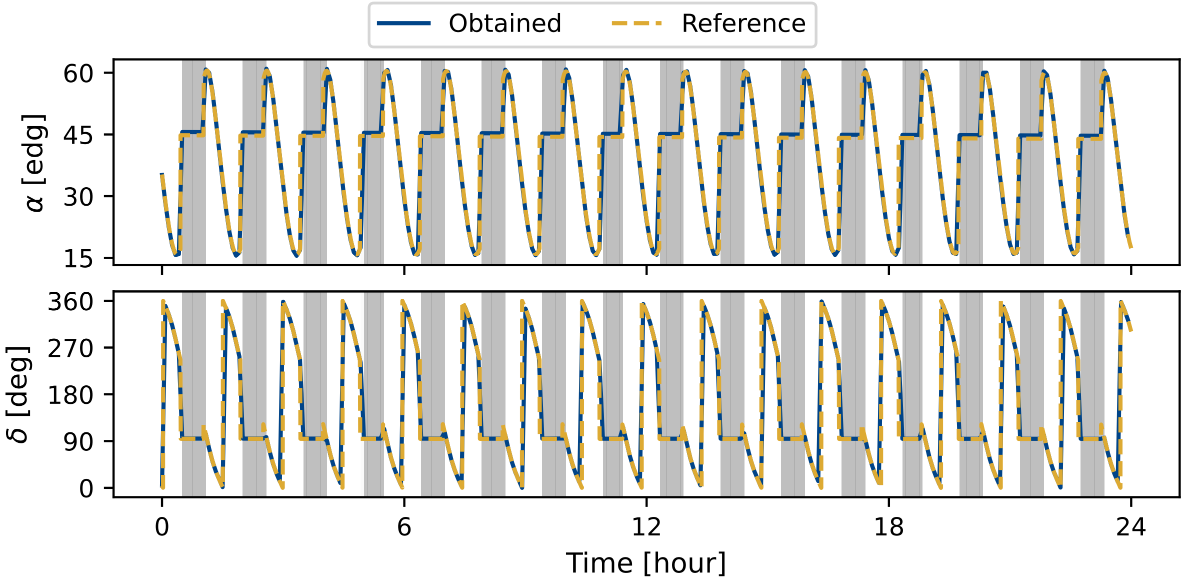

Figure G.1: Pitch, α, and clock, δ, angles for the validation scenario using the locally optimal semi-major axis control law. Shaded regions represent periods of umbra.

Two accelerations are considered: the ideal SRP acceleration and central gravity of the Earth. Two cases are studied: one using the locally optimal steering law to maximize the semi-major axis and the other employing the locally optimal steering law to maximize the inclination.

Figures G.1 and G.2 compare the results obtained from the Basilisk-based implementation with the reference solutions for the case of the locally optimal semi-major axis control law. As one can see, both propagations agree closely. The control law is followed closely, and as a result, the state of the spacecraft also behaves in a very similar manner. Small differences can be appreciated, which are likely due to slight dynamical modelling differences between the Basilisk implementation and the dynamics used to produce the reference. For instance, the Basilisk implementation considers a SRP that scales with the square of the distance between Sun and the Earth, while the reference implementation uses a constant SRP. Moreover, the Basilisk implementation uses SPICE to compute the position of the Sun, while the reference implementation uses analytical formulas from the Astronomical Almanac to compute this position. Other processes, such as integration error or numerical rounding error, may also contribute to the differences displayed. Finally, note that even though the inclination and the longitude of the ascending node are not shown in Figure G.2, they remain constant for both the reference and obtained results.

Similarly to Figures G.1 and G.2, Figures G.3 and G.4 compare the results obtained from the Basilisk-based implementation with the reference solutions for the case of the locally optimal inclination control law. One finds that the obtained and reference results are also in close agreement for this validation scenario.

G.2. Stochastic Integrator

Stochastic integrators are complex numerical algorithms used to produce sample solutions to a set of stochastic differential equations. This thesis involved the implementation of the weak third order integrator discussed in Appendix F. The equations presented in that appendix, however, are modifications of the equations presented in the original paper by Debrabant [4]. This was done so that the modified equations more closely resemble those of the deterministic Runge-Kutta method, which made implementation within Basilisk simpler and more consistent with existing algorithms. Because of this, verification and validation serve to assert that the derivation of these equations and their subsequent implementation was performed correctly.

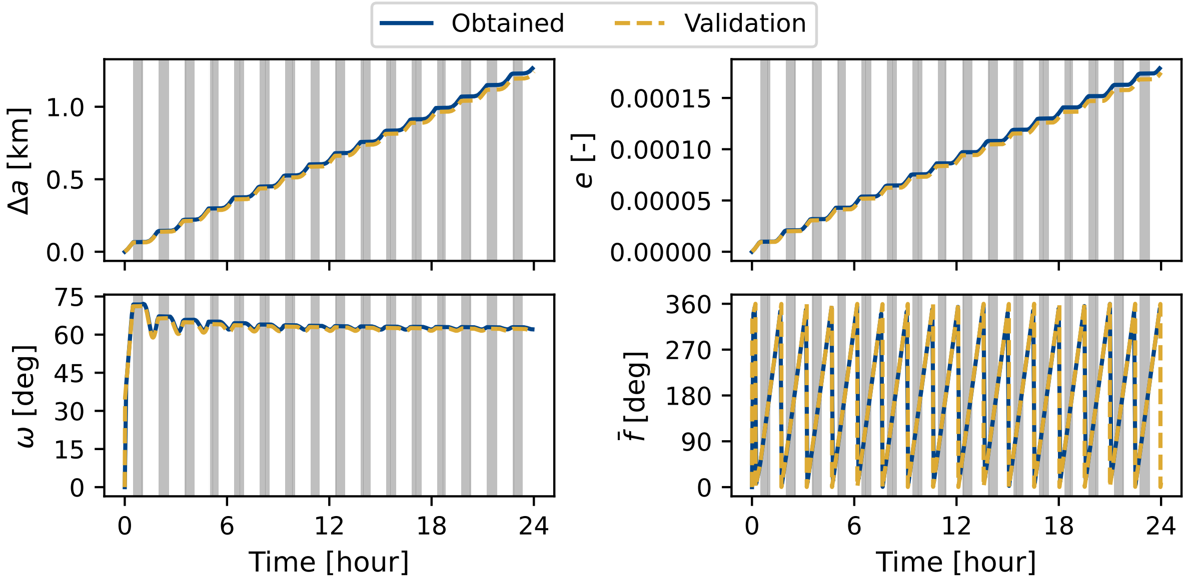

Figure G.2: Semi-major axis increase, Δa, eccentricity, e, argument of the periapsis, ω, and true anomaly, $\bar{f}$, for the validation scenario using the locally optimal semi-major axis control law. Shaded regions represent periods of umbra.

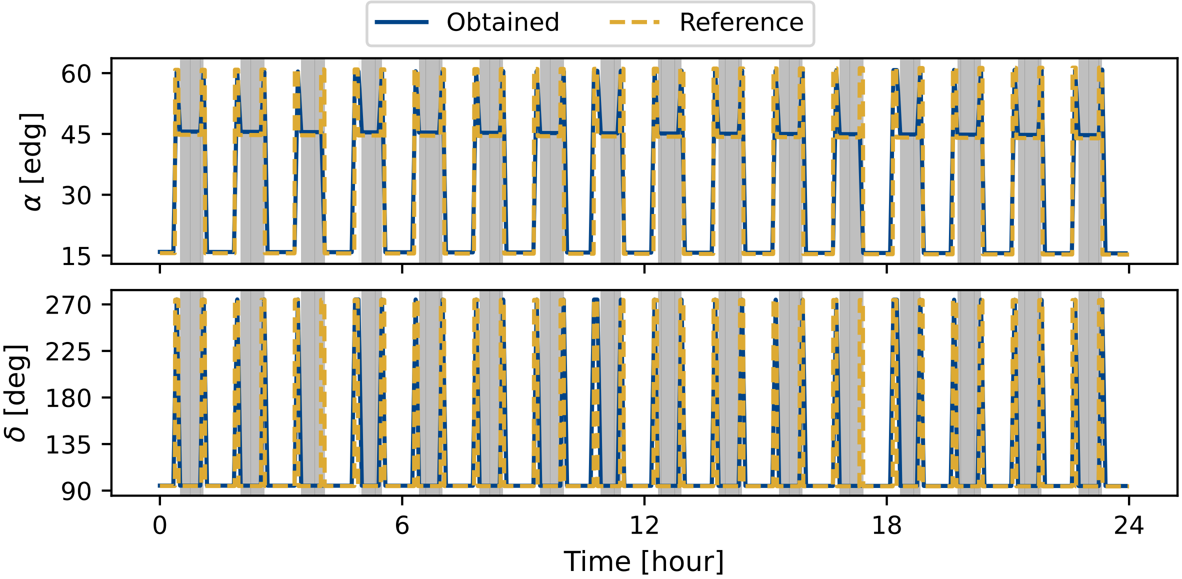

Figure G.3: Pitch, α, and clock, δ, angles for the validation scenario using the locally optimal inclination control law. Shaded regions represent periods of umbra.

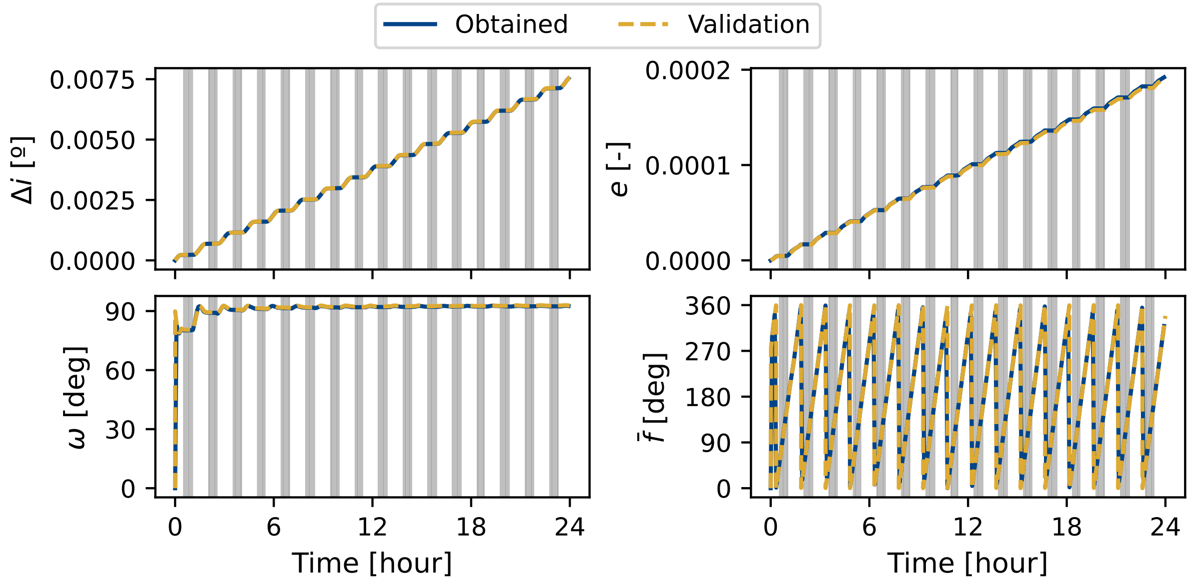

Figure G.4: Inclination increase, Δi, eccentricity, e, argument of the periapsis, ω, and true anomaly, $\bar{f}$, for the validation scenario using the locally optimal inclination control law. Shaded regions represent periods of umbra.

The following linear system of stochastic differential equations with three-dimensional noise was used during verification and validation:

$$d\begin{bmatrix} x_1 \\ x_2 \\ x_3 \end{bmatrix} = \begin{bmatrix} -0.5x_1 \\ -0.01x_1 - 0.75x_2 \\ 1.5x_3 \end{bmatrix} dt + \begin{bmatrix} -0.1 & 0 & 0 \\ 0.05 & 1/30 & 0 \\ 0 & 0 & 0.1 \end{bmatrix} \begin{bmatrix} d\beta_{\mathrm{Br},1}(t) \\ d\beta_{\mathrm{Br},2}(t) \\ d\beta_{\mathrm{Br},3}(t) \end{bmatrix} \tag{G.2}$$

with initial conditions: $[x_1, x_2, x_3]_0^T = [0, 0, 0.1]^T$. Note that x_3 is uncoupled from x_1 and x_2. For this simple case, one can prove that the analytical expression for the mean of x_3 is:

$$\mu_{x_3}(t) = 0.1e^{1.5t} \tag{G.3}$$

G.2.1. Verification

The stochastic integrator used in this work was implemented in C++ as a Basilisk module following the equations presented in Appendix F. To verify this implementation, a parallel implementation on Python using the original equations by Debrabant was created [4]. Verification thus consisted on asserting that a single step of the integrator produced the same results for the C++ and Python implementations. The stochastic differential equation shown in Eq. G.2 was used for this.

G.2.2. Validation

Ornstein-Uhlenbeck process

Of particular interest to this work is the correct integration of Ornstein-Uhlenbeck processes, which are used to model random angular offsets, see Section 3.2. It is known that an Ornstein-Uhlenbeck process defined by the following stochastic differential equation:

$$d\gamma = -\theta\gamma dt + \sigma d\beta_{\mathrm{Br}}(t) \tag{G.4}$$

has a stationary mean value of $\mu = 0$ and stationary standard deviation of $\sigma_{\mathrm{st}} = \sigma/\sqrt{2\theta}$. Thus, the stochastic integrator should be able to produce solutions with the same mean and standard deviation for $t \gg t_0$.

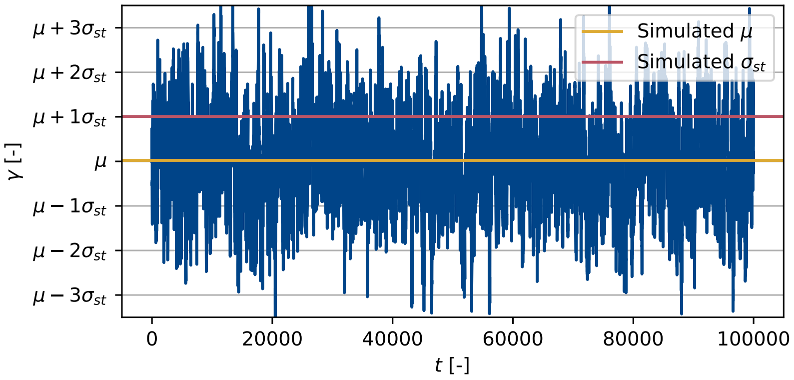

Figure G.5: Integration of an Ornstein-Uhlenbeck process, γ, with $\mu = 0$, $\theta = 10^{-2}$, and $\sigma_{\mathrm{st}} = 0.5$ using the stochastic integrator described in Section F with time step $\Delta t = 0.1$. The stationary mean and standard deviation of the simulated process are shown as yellow and red lines, respectively.

Figure G.5 shows a sample propagation of an Ornstein-Uhlenbeck process. The stationary mean and standard deviation of the simulated process are $\mu_{\mathrm{sim}} = 0.0101$ and $\sigma_{\mathrm{sim,st}} = 0.5035$, which represent reasonable deviations from the (arbitrarily chosen) nominal values: $\mu = 0$ and $\sigma_{\mathrm{st}} = 0.5$. Thus, it is validated that the stochastic integrator can produce simulations of the Ornstein-Uhlenbeck process with its expected properties.

Evolution of the error with respect to the time step

As discussed in Appendix F, an integrator of weak order Λ using time step Δt can produce discrete approximations, $\tilde{Y}^{(\Delta t)}(t)$, to the process $Y^{(\Delta t)}(t)$ with an error bound as:

$$|E[g(Y(t_f))] - E[g(\tilde{Y}^{(\Delta t)}(t_f))]| \leqslant C\Delta t^{\Lambda} \tag{G.5}$$

where C is some constant and $g(x)$ is a function in a family of functions that contains all polynomials. One such polynomial is the first-degree polynomial, such that $g(x) = x$. Then, the above equation reduces to:

$$|E[Y(t_f)] - E[\tilde{Y}^{(\Delta t)}(t_f)]| = |\mu_{Y(t_f)} - \mu_{\tilde{Y}^{(\Delta t)}(t_f)}| \leqslant C\Delta t^{\Lambda} \tag{G.6}$$

which means that the integration error of the mean of the process is bounded by $C\Delta t^{\Lambda}$. For the process $Y \equiv x_3$, as described in Eq. G.2, and a stochastic integrator of weak order $\Lambda = 3$, one expects:

$$|\mu_{x_3}(t_f) - \mu_{\tilde{x}_3^{(\Delta t)}(t_f)}| = |0.1e^{1.5t_f} - \mu_{\tilde{x}_3^{(\Delta t)}(t_f)}| \leqslant C\Delta t^3 \tag{G.7}$$

Note that an anlytical solution for the mean of x_3, $\mu_{x_3}(t_f)$, exists, while the mean of the approximation at time t_f, $\mu_{\tilde{x}_3^{(\Delta t)}(t_f)}$, must be obtained through a Monte Carlo simulation.

Given this knowledge, one can validate that the error of the implemented integrator follows the expected trend shown in Eq. G.7. Figure G.6 displays the evolution of the error as a function of the time step for $\Delta t = \{2^{-4}, 2^{-3}, 2^{-2}, 2^{-1}, 2^0, 2^1\}$. The mean of the approximation, $\mu_{\tilde{x}_3^{(\Delta t)}(t_f)}$, was obtained through a Monte Carlo simulation with 10^5 samples; the 3σ standard error for this estimated mean is shown as whiskers. Two exponential fits of the data are presented, one including and one ignoring the data point corresponding to $\Delta t = 2$. The first conclusion one may draw from this figure is that the integrator is "consistent", as this is a necessary condition for the error to converge to zero as $\Delta t \to 0$. This data can also serve to validate the (weak) order of the method. Figure G.6 shows two exponential fits, each with a different exponent, depending on the data points considered. While it is not possible to determine the order exactly, this data allows us to estimate that it is somewhere around the $\Lambda = 3$ region, as expected.

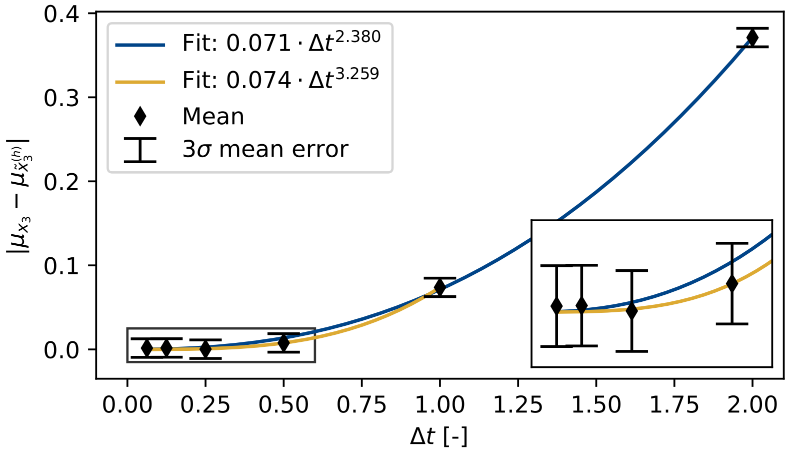

Figure G.6: Integrator error in the approximation of the mean of the process x_3 for $t_f = 2$ as a function of the time step.

G.3. The Gauss von Mises method

Section 3.3 briefly covers the Gauss von Mises method, with further details being available in Reference [7]. Given the complexity of this method, verification tests were implemented for each step in the algorithm. Moreover, the original paper by Horwood and Poore showed an example of the performance of the GVM method, which is here replicated for verification. Finally, validation of the GVM method is omitted from this appendix, as the results shown in this thesis already serve to validate that the Gauss von Mises method can replicate the results obtained from Monte Carlo simulations.

G.3.1. Verification

The implemented Gauss von Mises verification tests are:

- The computed weights of the samples must meet the theoretical constraints for the third-order quadrature method, which are shown in Table 1 in Reference [7].
- Assert that if the Gauss von Mises distribution used to generate a set of σ-points is canonical, the generated σ-point samples are also in canonical form.
- Given an initial Gauss von Mises distribution of the state of the spacecraft, the relevant σ-point set is generated. Then, this σ-point set is used to produce a Gauss von Mises distribution. Because the σ-point were not propagated or modified in any way, the resultant Gauss von Mises distribution should be the same as the initial Gauss von Mises distribution.
- In their original paper, Horwood and Poore show that the Gauss von Mises method can accurately estimate the propagation of state uncertainty for at least eight orbits under non-spherical gravity perturbations. Figure G.7 shows the same results, replicated with the implementation of the GVM method used in this work. Each of the contour lines encloses a region in which the spacecraft has a specific probability of appearing. From the innermost to the outermost contours, the probabilities are 10%, 30%, 50%, 70%, and 90%. This means that around 90% of the Monte Carlo points should rest within the outermost countour line. As one can see, similarly to the results shown by Horwood and Poore, there is a strong agreement between the GVM and MC methods.

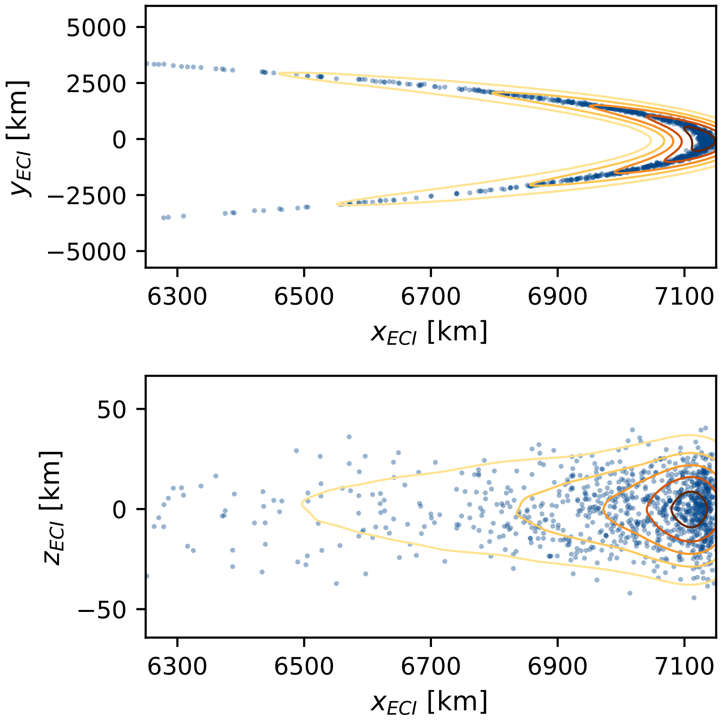

Figure G.7: Distribution of the state uncertainty of a spacecraft. Blue points represent 1000 samples obtained through a Monte Carlo simulation, while the contours represent the probability density function of the state as estimated by the Gauss von Mises method.

H

Integrator Selection

The Basilisk astrodynamics framework includes a set of adaptive and fixed-step Runge-Kutta integrators that can be freely selected and configured by users. Moreover, a stochastic integrator has been implemented, whose time step can also be configured. The selection of an integrator is critical to ensure that the numerical error of the method is small enough not to contaminate the results presented in this work. Assuming that this condition is met, the integrator should additionally be selected so that it is as computationally efficient as possible.

H.1. Deterministic integrator

In this section, a reference scenario is propagated using different integrators and time steps. The computational cost and integrator error associated with each solution are recorded, and based on these results an appropriate determinsitic integrator is selected. The reference scenario is a spacecraft using a solar sail with the characteristics described in Table 1, in a Sun Synchronous Orbit with LTAN at 12 AM, using the semi-major axis raising locally-optimal steering law, and for 10 days of propagation, which is considered representative of all scenarios studied in this work.

The dynamical model used in this work neglects several perturbations in the near-Earth environment, or otherwise performs significant simplifications. Among these are the simple exponential atmospheric model, simplified aerodynamic coefficient model, neglection of third-body gravitational effects and higher-order spherical harmonics for the Earth. Planetary radiation pressure is also ignored, which has been shown to be able to cause perturbations in the order of hundreds of meters for solar sails in Sun Synchronous orbits after 10 days of maneuvers [8]. Considering these modelling errors, an integrator error of at least an order of magnitude lower than these errors is desired. Thus, the maximum integrator error allowed in this work is 10 m. The reference solution is obtained with a Runge-Kutta integrator of order 8 and time step of 1 second.

Figure H.1 shows the position error and computational cost of several integrators as a function of the time step used. In this figure and in Table H.1 the notation "RKX" referes to a Runge-Kutta integrator of order "X" and "RKFXY" refers to an adaptive Runge-Kutta integrator of orders "X" and "Y". As one can see, neither the Runge-Kutta method of order 2 or the Euler method achieved the desired accuracy. With the exception of the RKF45 method with tolerance 10^{-10}, the adaptive Runge-Kutta methods seem to produce effectively the same position error when using the same time step. This is due to the adaptive Runge-Kutta integrator implementation in Basilisk; certain parameters, such as the position of the Sun, are only updated at the time step of the simulation. Adaptive Runge-Kutta methods cannot control the simulation time step, they may

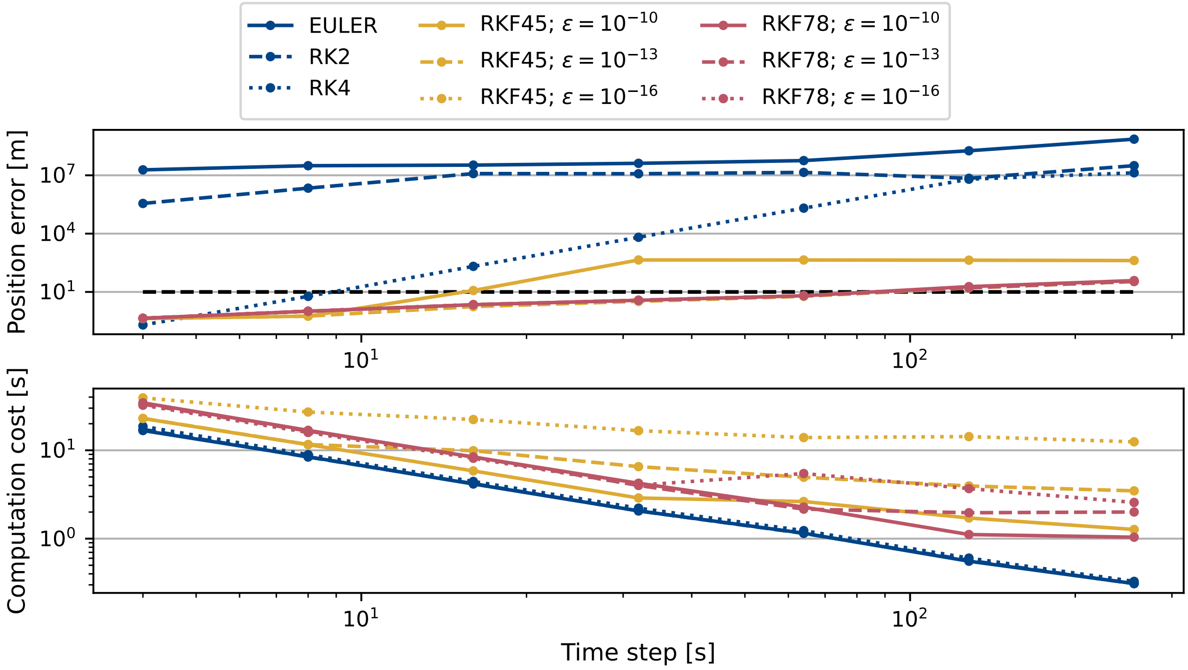

Figure H.1: Position error and computational cost associated with different integrators as a function of the time step. The maximum allowed error of 10 m is shown as a horizontal dashed line.

Table H.1: Position error and computational cost associated with each integrator when using the smallest time step that produces an error below the accuracy requirement of 10 m.

Integrator	Tolerance [-]	Time Step [s]	Position Error [m]	Computational Cost [s]
RK4	-	8	5.94	8.93
RKF45	10^{-10}	8	0.57	11.59
RKF45	10^{-13}	64	5.93	4.96
RKF45	10^{-16}	64	6.38	13.94
RKF78	10^{-10}	64	6.39	2.27
RKF78	10^{-13}	64	6.39	2.16
RKF78	10^{-16}	64	6.38	5.46

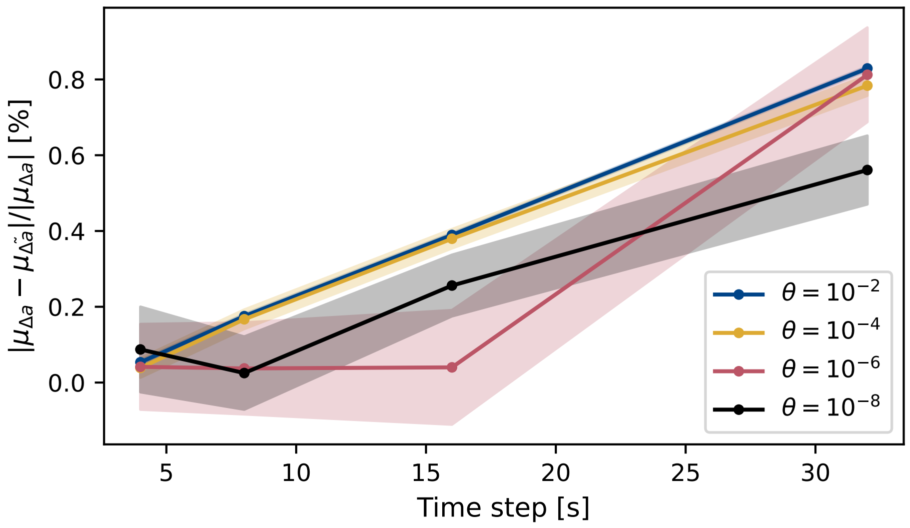

Figure H.2: Estimation error of the mean semi-major axis gain after 10 days of maneuvers for $\sigma_{\text{st}} = 5$ deg, different θ Ornstein-Uhlenbeck parameters, and integrator time steps.

only take smaller time steps between the larger, fixed simulation steps. This means that, independently of the tolerance and order of the adaptive integrator, there is some unavoidable error that depends only on the simulation time step.

Table H.1 shows the maximum time step required to achieve an integrator error below the required accuracy. Again, most adaptive integrators show the same behaviour independently of the tolerance used. Because of this, it is often best to employ fixed-step integrators in Basilisk, as they have lower computational overhead. As shown in the table, the "RKF78" method, which here acts effectively as a fixed-step Runge-Kutta method of order 8 with time step 64 s has the lowest computational cost, and thus is the integrator used to obtain the results shown in this project.

H.2. Stochastic Integrator

Determining the accuracy of a stochastic integrator is more complex than doing the same for a deterministic integrator. Given the intrinsic randomness of the system, each propagation performed with a stochastic integrator produces a random trajectory. Thus, the error associated with a stochastic integrator is evaluated by finding the error in the expected (mean) value of some function of the propagation. As discussed in Section G.2.2, this error is a function of the time step used.

This section evaluates the error in the estimation of the mean of the distribution of the semi-major axis after 10 days of maneuvers with a randomly evolving attitude offset, as described in Section 3.2. The test scenario is a solar sail with the characteristics described in Table 1, in a Sun Synchronous Orbit with LTAN at 12 AM, using semi-major axis raising locally-optimal steering law. The Ornstein-Uhlenbeck parameter σ_{st} is set to its maximum considered, 5 deg, while several θ parameters are considered.

Figure H.2 shows the error in the estimation of the mean as a function of the time step. As one can see, a time step of 16 s creates mean errors below 0.5% for the four θ parameters considered, making this time step an acceptable time step to generate the results shown in this work.

I

Shape Model Discretization

Section 2.2 introduced the shape model of the sail used in this thesis. Because the Generalized Sail Model formulas cannot be solved analytically when using this shape model, a discretization of the shape is necessary. The number of faces used in this discretization drives the discretization error introduced, as well as the computational cost associated with generating the $\mathbf{J}^k$ tensors.

Figures I.1 and I.2 quantify the error that the discretization introduces for a sail with the following parameters: $l = 30$ m, $\rho s = 0.75$, $a_2 = 0.4$, $a_3 = 0.25$, $\Delta z_{\text{tip}} = 0.08$ m and $\Delta z_{\text{billow}} = 0.05$ m, see Section 2.2 for the definition of these variables. Figure I.1 shows the absolute error in the $\mathbf{J}^k$ tensors, which as one can see, is greatest for the $\mathbf{J}^3$ tensor and practically negligible for the $\mathbf{J}^1$ tensor. Figure I.2, on the other hand, shows the relative error introduced in the SRP force for different pitch angles. Given the weak effect of the deformation in the total force, even low numbers of faces produce accurate results. In this thesis, shape models with 10,000 faces are used, which are shown to produce relative force errors with magnitude less than 10^{-5}% and take only 0.05 s to compute in a mainstream laptop.

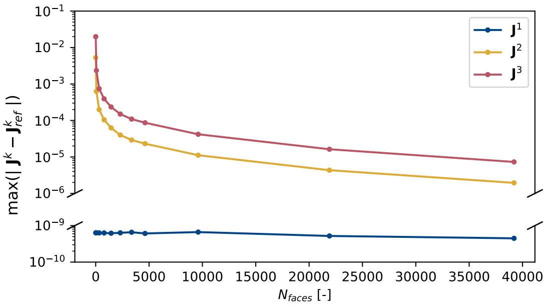

Figure I.1: Maximum absolute error for each $\mathbf{J}^k$ tensor as a function of the number of triangles used to discretize the surface.

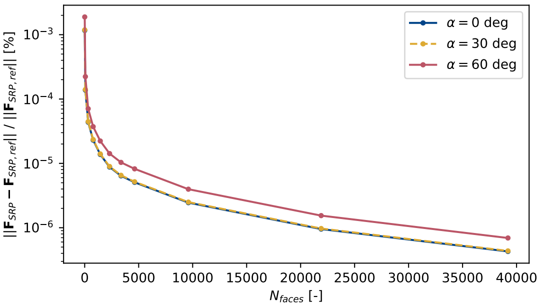

Figure I.2: Relative error of the SRP force for different pitch angles, α, as a function of the number of triangles used to discretize the surface.

J

Solar Radiation Pressure acceleration model

Section 2.2 briefly introduced the SRP acceleration model used in this thesis. This appendix expands this section by providing additional explanations that was not deemed of interest for the paper. Moreover, Section 2 introduces the "Conical" shadow model, which is also briefly explained in this appendix.

Recall that the model used in this thesis is the Generalized Sail Model developed by Rios-Reyes and Scheeres [9], which can account for deformed and non-ideal solar sails. Let us consider an infinitesimal piece of sail, dA, whose orientation is fully defined by a normal vector $\hat{\mathbf{n}}$, as defined in Section 2.1. Then, the SRP force on this infinitesimal piece of sail is given by:

$$d\mathbf{F}_{\text{SRP}} = d\mathbf{F}_{\mathbf{r}} - d\mathbf{F}_{\mathbf{a}} - d\mathbf{F}_{\mathbf{e}} \tag{J.1}$$

where $d\mathbf{F}_{\mathbf{r}}$ is the force caused by reflection, $d\mathbf{F}_{\mathbf{a}}$ is the force due to absorption, and $d\mathbf{F}_{\mathbf{e}}$ is the force due to emissivity (re-radiation). The total force due to reflection is given by [6]:

$$d\mathbf{F}_{\mathbf{r}} = PdA\left[-\left(\rho s \cos^2\alpha + B_{\text{f}}(1-s)\rho\cos\alpha\right)\hat{\mathbf{n}} - \rho s \cos\alpha\sin\alpha\hat{\mathbf{t}}\right] \tag{J.2}$$

where P is the SRP at the sailcraft location, ρ is the fraction of photons that are reflected (reflectivity), s is the fraction of reflected photons that are reflected specularily (specularity), and B_f is the Lambertian coefficient describing the sail's deviation of the front (illuminated) surface from a Lambertian surface. A Lambertian surface has the same radiance in all directions [10].

The total force due to absorption is given by [6]:

$$d\mathbf{F}_{\mathbf{a}} = PdA\left[-\cos^2\alpha\hat{\mathbf{n}} + \cos\alpha\sin\alpha\hat{\mathbf{t}}\right] \tag{J.3}$$

while the force due to emission is [6]:

$$d\mathbf{F}_{\mathbf{e}} = -PdA(1-\rho)(1-\rho)\frac{\varepsilon_f B_f - \varepsilon_b B_b}{\varepsilon_f + \varepsilon_b}\cos\alpha\hat{\mathbf{n}} \tag{J.4}$$

where B_b is the is the Lambertian coefficient of the back (dark) side of the sail; and ε_f and ε_b are the emissivity coefficients for the sail's front and back sides, respectively.

Combining Eqs. J.1, J.2, J.3, and J.4 one reaches the previously introduced Eq. 4 for the differential SRP force $d\mathbf{F}_{\text{SRP}}$ produced by a differential area of sail dA:

$$d\mathbf{F}_{\text{SRP}} = PdA\left[-\left(a_1\cos^2\alpha + a_2\cos\alpha\right)\hat{\mathbf{n}} + a_3\cos\alpha\sin\alpha\hat{\mathbf{t}}\right] \tag{J.5}$$

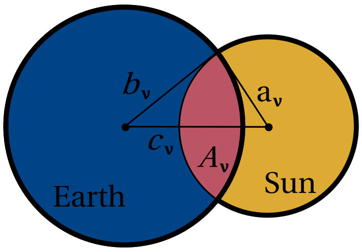

Figure J.1: Schematic to determine the shadow factor as per the conical shadow model [11].

On the other hand, Figure J.1 can be used to further understand the "Conical" shadow model. This figure shows the Earth and Sun's disks from the perspective of the spacecraft. The triangle joining the disks' centers and the disks' intersection has sides a_ν, b_ν, and c_ν. The area of intersection of the disks, A_ν, is given by [11]:

$$A_\nu = a_\nu^2 \cos^{-1}\left(\frac{x_\nu}{a_\nu}\right) + b_\nu^2 \cos^{-1}\left(\frac{c_\nu - x_\nu}{b_\nu}\right) - c_\nu y_\nu \tag{J.6}$$

where

$$x_\nu = \frac{c_\nu^2 + a_\nu^2 - b_\nu^2}{2c_\nu} \quad \text{and} \quad y_\nu = \sqrt{a_\nu^2 - x_\nu^2} \tag{J.7}$$

If the Sun's disk is completely covered by the Earth's disk, then the shadow factor is $\nu = 0$. When the disks do not intersect, then the shadow factor is $\nu = 1$. Finally, for the case of penumbra, as is shown in Figure J.1, the shadow factor is given by [11]:

$$\nu = 1 - \frac{A_\nu}{\pi a_\nu^2} \tag{J.8}$$

Appendixes Bibliography

[1] P. W. Kenneally, S. Piggott, and H. Schaub. “Basilisk: A flexible, scalable and modular astrodynamics simulation framework”. In: *Journal of aerospace information systems* 17.9 (2020), pp. 496–507.

[2] David M. Beazley. “Using SWIG to control, prototype, and debug C programs with Python”. In: *4th International Python Conference* (1996).

[3] K. Kumar et al. “Tudat: a modular and robust astrodynamics toolbox”. In: *5th ICATT Conference*. ESA. 2012, pp. 1–8.

[4] K. Debrabant. “Runge-Kutta methods for third order weak approximation of SDEs with multidimensional additive noise”. In: *BIT Numerical Mathematics* 50 (2010), pp. 541–558.

[5] P. E. Kloeden and E. Platen. *Numerical Solution of Stochastic Differential Equations*. 3rd ed. 1999.

[6] C. R. Mcinnes. *Solar sailing: technology, dynamics and mission applications*. Springer Science & Business Media, 2004.

[7] J. T. Horwood, N. D. Aragon, and A. B. Poore. “Gaussian sum filters for space surveillance: theory and simulations”. In: *Journal of Guidance, Control, and Dynamics* 34.6 (2011), pp. 1839–1851.

[8] L. Carzana, P. Visser, and J. Heiligers. “A New Model for the Planetary Radiation Pressure Acceleration for Solar Sails”. In: *2022 AAS/AIAA Astrodynamics Specialist Conference*. 2022.

[9] L. Rios-Reyes and D. Scheeres. “Trajectory Control for General Solar Sails”. In: *AIAA Guidance, Navigation and Control Conference and Exhibit*. 2008. DOI: `10.2514/6.2008-6830`.

[10] J. Meyer-Arendt. *Introduction to Classical and Modern Optics*. Prentice-Hall, 1984.

[11] O. Montenbruck, E. Gill, and F. H. Lutze. “Satellite Orbits: Models, Methods, and Applications”. In: *Applied Mechanics Reviews* 55.2 (Apr. 2002), B27–B28. DOI: `10.1115/1.1451162`.